Pathways of Nitrous Oxide Production in the Eastern Tropical South Pacific Oxygen Minimum Zone

Daniel McCoy[1], Pierre Damien[1], Daniel J Clements[1], Simon Yang[1], Daniele Bianchi[2], Annie Bourbonnais[3], Laura Bristow[4], Pearse Buchanan[5], Phyllis Lam[6], Andrew Babbin[7], Emily Zakem[8], and Colette Kelly[9]

[1]UCLA
[2]University of California Los Angeles
[3]University of South Carolina
[4]University of Southern Denmark
[5]University of Liverpool
[6]University of Southampton
[7]Massachusetts Institute of Technology
[8]Carnegie Institution for Science
[9]Stanford University, Department of Earth System Science

December 9, 2022

Abstract

Oceanic emissions of nitrous oxide (N2O) account for roughly one-third of all natural sources to the atmosphere. Hot-spots of N2O outgassing occur over oxygen minimum zones (OMZs), where the presence of steep oxygen gradients surrounding anoxic waters leads to enhanced N2O production from both nitrification and denitrification. However, the relative contributions from these pathways to N2O production and outgassing in these regions remains poorly constrained, in part due to shared intermediary nitrogen tracers, and the tight coupling of denitrification sources and sinks. To shed light on this problem, we embed a new, mechanistic model of the OMZ nitrogen cycle within a three-dimensional eddy-resolving physical-biogeochemical model of the ETSP, tracking contributions from remote advection, atmospheric exchange, and local nitrification and denitrification. Our results indicate that net N2O production from denitrification is approximately one order of magnitude greater than nitrification within the ETSP OMZ. However, only ˜30% of denitrification-derived N2O production ultimately outgasses to the atmosphere in this region (contributing ˜34% of the air-sea N2O flux on an annual basis), while the remaining is exported out of the domain. Instead, remotely-produced N2O advected into the OMZ region accounts for roughly half (˜56%) of the total N2O outgassing, with smaller contributions from nitrification (˜7%). Our results suggests that, together with enhanced production by denitrification, upwelling of remotely-derived N2O (likely produced via nitrification in the oxygenated ocean) contributes the most to N2O outgassing over the ETSP OMZ.

Pathways of Nitrous Oxide Production in the Eastern Tropical South Pacific Oxygen Minimum Zone

Daniel McCoy[1], Pierre Damien[1], Daniel Clements[1], Simon Yang[1], Daniele Bianchi[1]

[1]Department of Atmospheric and Oceanic Sciences
[1]University of California – Los Angeles
[1]520 Portola Plaza, Los Angeles, CA 90095, USA

Key Points:

- In the eastern tropical South Pacific Oxygen Minimum Zone, denitrification is the dominant source of N_2O production.
- Tropical subsurface currents supply N_2O to the region, fueling N_2O emissions to the atmosphere.
- Significant amounts of locally-produced N_2O escape outgassing and are exported to the subtropical gyre.

Corresponding author: Daniel McCoy, `demccoy@atmos.ucla.edu`

Abstract

Oceanic emissions of nitrous oxide (N_2O) account for roughly one-third of all natural sources to the atmosphere. Hot-spots of N_2O outgassing occur over oxygen minimum zones (OMZs), where the presence of steep oxygen gradients surrounding anoxic waters leads to enhanced N_2O production from both nitrification and denitrification. However, the relative contributions from these pathways to N_2O production and outgassing in these regions remains poorly constrained, in part due to shared intermediary nitrogen tracers, and the tight coupling of denitrification sources and sinks. To shed light on this problem, we embed a new, mechanistic model of the OMZ nitrogen cycle within a three-dimensional eddy-resolving physical-biogeochemical model of the ETSP, tracking contributions from remote advection, atmospheric exchange, and local nitrification and denitrification. Our results indicate that net N_2O production from denitrification is approximately one order of magnitude greater than nitrification within the ETSP OMZ. However, only ∼30% of denitrification-derived N_2O production ultimately outgasses to the atmosphere in this region (contributing ∼34% of the air-sea N_2O flux on an annual basis), while the remaining is exported out of the domain. Instead, remotely-produced N_2O advected into the OMZ region accounts for roughly half (∼56%) of the total N_2O outgassing, with smaller contributions from nitrification (∼7%). Our results suggests that, together with enhanced production by denitrification, upwelling of remotely-derived N_2O (likely produced via nitrification in the oxygenated ocean) contributes the most to N_2O outgassing over the ETSP OMZ.

1 Introduction

Nitrous oxide (N_2O) is a powerful greenhouse gas that is roughly 300 times more potent than carbon dioxide (CO_2) and is projected to become the most important ozone-depleting anthropogenic emission by the end of the 21st century (Ravishankara et al., 2009; IPCC, 2013). Recent analyses of the global N_2O budget over the decade of 2007 - 2016 suggest that anthropogenic emissions are responsible for up to 40% of total N_2O sources to the atmosphere, mostly from agriculture, whereas outgassing from the ocean accounts for roughly 20% (Canadell et al., 2021). The production of N_2O in the ocean is linked to the remineralization of organic matter (OM) via both aerobic and anaerobic pathways, and, as a consequence, is tightly coupled to the oceanic oxygen (O_2) distribution (Freing et al., 2012; Arévalo-Martínez et al., 2015; Babbin et al., 2015; Ji et al., 2015; Yang et al., 2020). While in large parts of the surface ocean N_2O concentrations are close to saturation, the most intense hot-spots of N_2O air-sea flux are found in the Eastern Tropical North Pacific (ETNP), the Eastern Tropical South Pacific (ETSP), and the Arabian Sea, where high organic matter export rates and sluggish lateral circulation results in steep O_2 gradients that surround anoxic (here defined as $O_2 < 5\ mmol\ m^{-3}$) waters also known as oxygen minimum zones (OMZ)(Codispoti, 2010; Arévalo-Martínez et al., 2015; Ji et al., 2018; Yang et al., 2020). Although OMZ regions only account for roughly 1% of the total ocean volume, the dynamic marine nitrogen cycling that occurs there results in up to 50% of total oceanic N_2O emissions (Codispoti, 2010; Arévalo-Martínez et al., 2015; Babbin et al., 2015; Yang et al., 2020).

The ETSP hosts the second largest OMZ by area and comprises the Humboldt Current System, one of the four major Eastern Boundary Upwelling Systems, which extends from the southern extent of Chile ($\sim 45^oS$) to northern Peru ($\sim 4^oS$)(Chavez & Messié, 2009; Santoro et al., 2021). While southern Chile experiences more intense upwelling during boreal summer (Pennington et al., 2006), upwelling-favorable conditions exist year-round along the Peruvian and northern Chile coastlines, fueling high rates of surface primary productivity, organic matter export (Chavez & Messié, 2009), and subsurface O_2 depletion. The ETSP OMZ is located in the South Pacific tropical shadow zone of the thermocline (Luyten et al., 1983), which extends westward from the eastern boundary between the equatorward edges of the subtropical gyres. This limits the supply of oxy-

gen from the ventilated subtropical gyres to the OMZs, and leaves the relatively O_2-rich eastward tropical currents such as the Equatorial Undercurrent (EUC) and the Southern Subsurface Countercurrents (SSCC) as the major advective sources of O_2 to the equatorward side of the ETSP OMZ (Karstensen et al., 2008; Stramma et al., 2010). While these advective pathways are reinforced by lateral O_2 supply from mesoscale eddies (Gnanadesikan et al., 2013; Bettencourt et al., 2015), O_2 remains depleted within the OMZ core (Kwiecinski & Babbin, 2021), leading to functional anoxia (Thamdrup et al., 2012), fixed nitrogen loss, a pronounced subsurface nitrite (NO_2^-) maximum, and a strong nitrogen deficit (Kalvelage et al., 2013). An additional characteristic of the ETSP is the relatively sharp transition from anoxic to suboxic ($5\ mmol\ m^{-3} < O_2 < 10\ mmol\ m^{-3}$) waters along the OMZ boundary. These O_2 gradients host both aerobic (i.e., nitrification) and anaerobic (i.e., denitrification) nitrogen cycle transformations, ultimately leading to N_2O supersaturation in the layers surrounding the anoxic core (Babbin et al., 2015; Kock et al., 2016). Upwelling of these waters to the surface likely contributes to the local hot-spot of N_2O outgassing in the ETSP, as shown by observational and modeling studies (Arévalo-Martínez et al., 2015; Ji et al., 2018; Yang et al., 2020).

Nitrification is a two-step process that occurs within the oxygenated water column wherein ammonium (NH_4^+) produced from remineralization of organic matter (pathway 1 in Figure 1) is oxidized by O_2 to NO_2^- and subsequently to nitrate (NO_3^-) by NH_4^+-oxidizing bacteria and archaea and NO_2^--oxidizing bacteria, respectively (pathways 2 and 4, respectively) (Lam & Kuypers, 2011). Nitrification-derived N_2O occurs as a byproduct of NH_4^+ oxidation (pathway 3), resulting in a positive correlation between apparent oxygen utilization (AOU) and supersaturated N_2O concentrations in many areas of the ocean (Cohen & Gordon, 1978; Walter et al., 2006), a process that has been further quantified by active production of $^{15}N_2O$ in ^{15}N tracer incubation experiments (Yoshida et al., 1989). The ratio of N_2O yield to NO_2^- yield from NH_4^+ oxidation has been observed to increase at decreasing O_2 concentrations in cultures with NH_4^+-oxidizing bacteria and archaea (Goreau et al., 1980; Löscher et al., 2012), likely leading to enhanced nitrification-derived N_2O production within the steep suboxic gradients above and below the anoxic core of OMZs (Nevison et al., 2003; Ji et al., 2015, 2018; Santoro et al., 2021).

Besides N_2O production via the nitrification pathway, N_2O also forms as an intermediary product of step-wise denitrification (NO_3^- to NO_2^- to N_2O to N_2) under suboxic and anoxic conditions (pathways 5 - 7 in Figure 1). Within the anoxic core of OMZs, widespread consumption of N_2O occurs via N_2O reduction — the only known process able to remove N_2O from the water column. However, recent studies have highlighted how the different steps, each mediated by distinct enzymes and likely different microorganisms (Ganesh et al., 2014; Kuypers et al., 2018), are subject to variable O_2 sensitivities wherein NO_3^-, NO_2^-, and N_2O reduction become progressively less O_2 tolerant (Körner & Zumft, 1989; Kalvelage et al., 2011; Dalsgaard et al., 2014; Babbin et al., 2015; Ji et al., 2015). Therefore, the same suboxic gradients that lead to enhanced N_2O production from nitrification can also lead to N_2O accumulation from denitrification, as NO_2^- reduction proceeds while N_2O reduction is inhibited, in a process referred to as "incomplete" denitrification (Babbin et al., 2015).

The coupled production of N_2O at low O_2 from nitrification and denitrification, and their shared NO_2^- intermediary, complicate the interpretation of in situ observations from OMZs (Ji et al., 2015, 2018; Santoro et al., 2021). Observations of N_2O and NO_2^- in these regions typically reveal an OMZ anoxic core layer characterized by a secondary NO_2^- maximum and undersaturated N_2O concentrations, suggesting coupled step-wise denitrification. Supersaturated concentrations of N_2O in the bounding suboxic gradients (the upper and lower oxyclines) have been linked to the enhanced production by nitrification (Cohen & Gordon, 1978). Yet, studies have noted the lack of a linear relationship with AOU and high abundances of gene markers for NO_2^- reduction as evidence

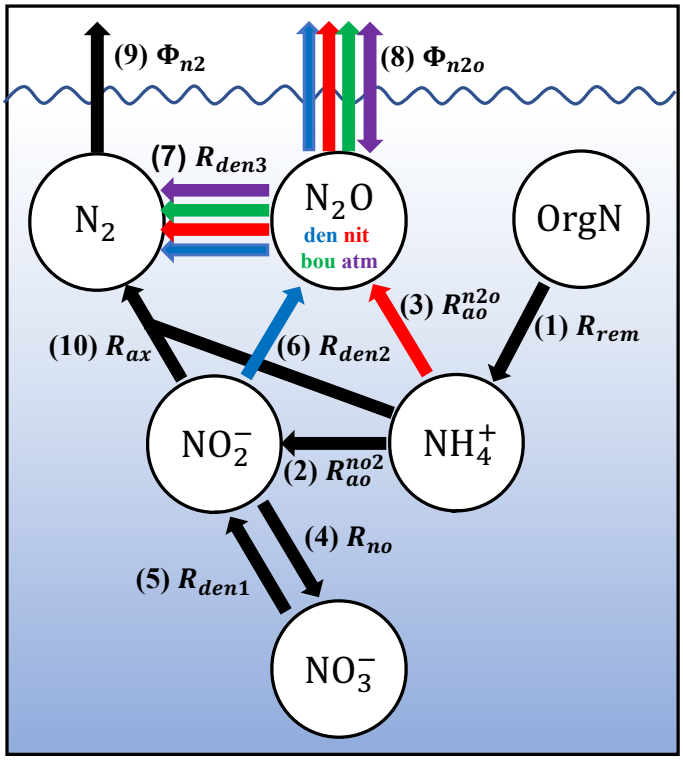

Figure 1. Schematic of the oceanic nitrogen cycle (ignoring biological uptake) as represented in ROMS. Transformation pathways include: (1, R_{rem}) oxic remineralization of nitrogen in organic matter (OrgN) to ammonium; (2, R_{ao}^{no}) ammonium oxidation to nitrite; (3, R_{ao}^{n2o}) ammonium oxidation to nitrous oxide; (4, R_{no}) nitrite oxidation; (5, R_{den1}) nitrate reduction; (6, R_{den2}) nitrite reduction; (7, R_{den3}) decomposed nitrous oxide reduction; (8, Φ_{n2o}) decomposed nitrous oxide air-sea flux; (9, Φ_{n2}) dinitrogen air-sea flux; and (10, R_{ax}) anaerobic ammonium oxidation (anammox). Colored arrows correspond to the sources and sinks of the decomposed N_2O tracers (N_2O_{den}, N_2O_{nit}, N_2O_{bou}, and N_2O_{atm}) discussed in Section 2.4.

of simultaneous production from both nitrification and incomplete denitrification (Arévalo-Martínez et al., 2015), as further supported by isotopic evidence (Bourbonnais et al., 2017).

However, while progressive O_2 tolerances for denitrification have been documented (Dalsgaard et al., 2014), biogeochemical models predominantly employ simple parameterizations representing N_2O production as a function of nitrification, whereas denitrification is typically modelled with a lack of N_2O production or as a net sink of N_2O at low O_2 (Suntharalingam et al., 2000; Jin & Gruber, 2003; Ji et al., 2018; Battaglia & Joos, 2018). Other studies have highlighted the importance of resolving O_2-dependent decoupling of N_2O production and consumption (Babbin et al., 2015), suggesting that N_2O production rates from denitrification may be up to two orders of magnitude larger than those from nitrification near the core of OMZs, albeit closely balanced by N_2O reduction to dinitrogen gas (N_2). Thus, incomplete denitrification may account for a production source that is poorly represented in most biogeochemical ocean and climate models.

While the uncertainty surrounding N_2O production in the ocean has been reduced in recent years following improved estimates of ocean (Yang et al., 2020), terrestrial, and anthropogenic N_2O sources (Canadell et al., 2021; Tian et al., 2020), barriers remain in

accurately projecting future air-sea flux because of poorly constrained contributions from the nitrification and denitrification pathways. The observed expansion of OMZs (Stramma et al., 2008; Schmidtko et al., 2017; Oschlies et al., 2018) is expected to continue over the 21st century, although the extent of future changes in low O_2 and anoxic water volumes remain uncertain (Cabré et al., 2015; Bianchi et al., 2018; Busecke et al., 2021). Therefore, accurate parameterization of N_2O cycling in global ocean models is crucial in simulating realistic future scenarios, and a better understanding of the physical and biogeochemical mechanisms and relative contributions from both production pathways is warranted. This is particularly critical given that OMZ regions continue to be poorly resolved in current global Earth system models (Cabré et al., 2015; Busecke et al., 2021; Séférian et al., 2020), which generally struggle to capture the role of fine-scale circulation such as the zonal jet systems that ventilate the tropical Ocean (Kessler, 2006; Duteil et al., 2014; Busecke et al., 2019; Duteil et al., 2021).

To address these sources of uncertainty, we implement a new model of the OMZ nitrogen cycle (NitrOMZ) (Bianchi et al., 2022) into an eddy-resolving three-dimensional (3-D) regional ocean model of the ETSP that simulates local N_2O production from nitrification and denitrification. The new model, constrained by in situ ETSP observations of nitrogen cycle tracers and rates, allows for an examination of the N_2O balance within a characteristic OMZ upwelling region. To attribute the sources of N_2O outgassing flux to different processes, we use the 3-D model to track contributions from local air-sea gas exchange, advection into the domain from the boundaries, and production by nitrification and denitrification. This analysis reveals the importance of incomplete denitrification and transport of remotely-generated N_2O for air-sea fluxes, with implications for future N_2O emissions in a changing ocean.

The rest of the paper is organized as follows: Section 2 describes the 3-D model configuration and setup, a brief summary of N_2O production pathways in NitrOMZ, and the N_2O tracer decomposition strategy; Section 3 provides a short validation of model solutions, summarizes the results of the simulations, and describes the ETSP N_2O balance; Section 4 discusses the results and implications, and concludes the paper.

2 Modelling Methods and Validation

2.1 Physical Model Configuration and Forcing

The physical component of the model consists of the Regional Ocean Modeling System (ROMS) (Shchepetkin & McWilliams, 2005; Shchepetkin, 2015), a primitive-equation, hydrostatic, topography-following general ocean circulation model. The model domain extends from -111.38^oW to -66.62^oW and from 42.52^oS to 3.41^oN and is chosen to resolve key oceanographic features of the ETSP such as the EUC (Figure 2c), the wind-driven South Pacific gyre (contour lines in Figure 2a and 2b), and the horizontal extent of the OMZ (Figure 3a). Its grid consists of 402 x 502 points with a nominal resolution of 10 kilometers and 42 topography-following vertical levels with higher resolution at the surface and bottom. The model time-step is 800 seconds, and output is saved as monthly means.

For this study, low-frequency interannual variability is ignored to instead focus on a climatological steady-state. Initial conditions and monthly climatological boundary forcing (applied at the northern, western, and southern boundaries) for temperature, salinity, surface elevation, and horizontal velocity are taken from an existing Pacific-wide ROMS simulation (Lemarié et al., 2012). Normal-year-forcing of daily freshwater and turbulent heat fluxes are estimated using bulk formulae (Large, 2006) applied to ERA-interim (ERAi) reanalysis data for the year 1979 (Simmons et al., 2006; Dee et al., 2011). Because of known biases in ERAi shortwave (overestimate) and longwave (underestimate) fluxes (Brodeau et al., 2010), we applied the DRAKKAR Forcing Set version 5.2 corrections to heat flux

terms (Dussin et al., 2014). Daily climatological wind stress is taken from the QuickSCAT-based Scatterometer Climatology of Ocean Winds (Risien & Chelton, 2008). The resulting simulation produces an overall similar climatological picture of the hydrographic properties, gyre circulation, and equatorial current structure of the ETSP (Figure 2a - c) when compared to validation products (Figure 2d - f).

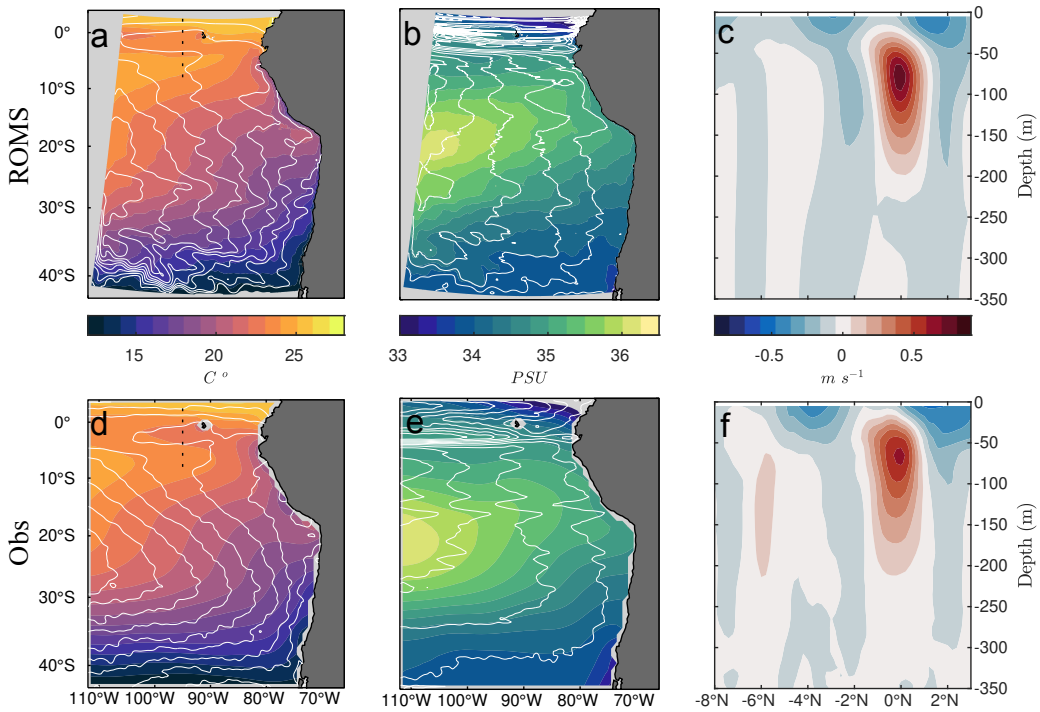

Figure 2. (a,d) Annually averaged sea-surface temperature from ROMS model years 46 - 50 (top) and World Ocean Atlas 2018 (bottom). Contours highlight sea-surface height at 5 *cm* intervals, with validation data obtained by averaging AVISO data between 2000 to 2018. Dashed lines mark the transect location in panels (c) and (f). (b,e) Same as in panels (a) and (d), but for sea-surface salinity; contours highlight calculated geostrophic velocity streamlines, with validation data derived from AVISO. (c,f) Zonal velocity sections along the equator at 95^oW from ROMS (top) and Johnson et al. (2002) (bottom).

2.2 Biogeochemical Model Configuration and Forcing

The physical model is coupled online to the Biogeochemical Elemental Cycling (BEC) model from Moore et al. (2004) using the same equations and parameter settings as in Frischknecht et al. (2017) with the exception of the nitrogen cycling component, which was expanded for the NitrOMZ model (Bianchi et al., 2022). NitrOMZ explicitly resolves the main set of nitrogen cycle transformations associated with the remineralization of sinking OM in low O_2 environments (summarized in Figure 1). These include the chemolithotrophic reactions associated with nitrification: aerobic NH_4^+ oxidation to both N_2O ($R_{ao}^{n_2o}$) and NO_2^- ($R_{ao}^{no_2}$), and aerobic NO_2^- oxidation to NO_3^- (R_{no}). Anaerobic NH_4^+ oxidation with NO_2^- to N_2 (anammox, R_{ax}) is also represented. Additionally, NitrOMZ partitions the OM remineralization cycle in ROMS-BEC to include three additional heterotrophic denitrification steps: NO_3^- reduction to NO_2^- (R_{den1}), NO_2^- reduction to N_2O (R_{den2}), and N_2O reduction to N_2 (R_{den3}). The treatment of OM in the model is outlined in support-

ing information S1, with chemolithotrophic and heterotrophic reactions summarized in S2. Notably, the model expands BEC by allowing for the production of N_2O via both nitrification and incomplete denitrification pathways (Section 2.2.1).

Initial conditions and boundary forcing of biogeochemical nutrient concentrations (NO_3^-, PO_4^{3-}, $Si(OH)_4$ and O_2) are taken from monthly climatological observations from the 2013 World Ocean Atlas (H. E. Garcia, Boyer, et al., 2013; H. E. Garcia, Locarnini, et al., 2013); NH_4^+, NO_2^-, and N_2 boundary conditions are set to 0 but adjust rapidly within the domain. Iron data were taken from the Community Earth System Model (CESM) as in Deutsch et al. (2021), and DIC/Alkalinity were extracted from GLODAP (Lauvset et al., 2016) with a reference year of 2002. Initial and monthly boundary conditions for N_2O were provided from a 3-D reconstruction based on in situ data from recent cruises to the ETSP (Kalvelage et al., 2013; Ji et al., 2015; Peng et al., 2016; Babbin et al., 2017, 2020), and the MEMENTO databases (Kock & Bange, 2015) and GLODAP (Olsen et al., 2016; Lauvset et al., 2016), which we extrapolate to the model domain using the same machine learning approach as described in Yang et al. (2020).

2.2.1 NitrOMZ N_2O Production

Production of N_2O via nitrification in NitrOMZ is modelled as a by-product of NH_4^+ oxidation ($R_{ao}^{n_2o}$, pathway 3 in Figure 1), with enhanced yields at lower O_2 concentrations. Both nitrification steps (i.e. NO_2^- oxidation) are suppressed near the surface by light inhibition (see supporting information S4) and competition for NH_4^+ and NO_2^- from phytoplankton as in Frischknecht et al. (2017). Therefore, nitrification is largely restricted to below the euphotic zone while also being suppressed at low O_2. The partitioning between N_2O and NO_2^- production from R_{ao} is calculated using the function proposed by Nevison et al. (2003), derived by fitting measured N_2O and NO_2^- yields ($f_{ao}^{n_2o}$ and $f_{ao}^{no_2}$, respectively) to oxygen concentrations (Goreau et al., 1980):

$$\frac{f_{ao}^{n_2o}}{f_{ao}^{no_2}} = 0.01 \cdot \frac{a}{[O_2]} + b. \tag{1}$$

Relative to the original parameterization by Nevison et al. (2003), we apply distinct values of the parameters a and b to reflect results from a series of in situ measurements of N_2O production from the ETSP and ETNP OMZs (Ji et al., 2015, 2018; Santoro et al., 2021) (see Section 2.3.1). N_2O production by nitrification, in units of *mmol* N m^{-3} s^{-1}, is therefore represented as:

$$R_{ao}^{n_2o} = R_{ao} \cdot f_{ao}^{n_2o}, \tag{2}$$

with a similar function for NO_2^- production.

In the denitrification pathway, N_2O is produced via NO_2^- reduction at low O_2:

$$R_{den2}^{n_2o} = f_{den2} \cdot R_{rem}^{tot} \cdot Q_{den}^{C:N}, \tag{3}$$

where f_{den2} is the local fraction of total OM remineralization (R_{rem}^{tot}) routed to NO_2^- reduction (see supporting information S2), and $Q_{den}^{C:N}$ the carbon to nitrogen ratio from denitrification (472/2/106) following Anderson and Sarmiento (1994). Similarly, N_2O is consumed via N_2O reduction to N_2 at low O_2:

$$R_{den3}^{n_2} = f_{den3} \cdot R_{rem}^{tot} \cdot Q_{den}^{C:N}. \tag{4}$$

Net production of N_2O ($R_{net}^{n_2o}$, in units of *mmol* N_2O m^{-3} s^{-1}) results by the combination of nitrification (equation (2)) and the residual between NO_2^- and N_2O reduction (equation (3) minus equation (4)):

$$R_{net}^{n_2o} = 0.5 \cdot (R_{ao}^{n_2o} + R_{den2}^{n_2o}) - R_{den3}^{n_2}. \tag{5}$$

2.3 Biogeochemical Validation

To validate the biogeochemical tracer distributions simulated by ROMS-BEC, we gathered O_2, NO_3^-, PO_4^{-3}, and N^* (defined as 16·[NO_3^-] - [PO_4^{3-}]) reconstructions from World Ocean Atlas 2018 (H. Garcia et al., 2019a) (Figures S1 - S4); additional O_2 estimates were provided by Dunn (2012) and Bianchi et al. (2012). Estimates of 3-D NO_2^- and N_2O were obtained from in situ observations (Kock & Bange, 2015; Lauvset et al., 2016), and extrapolated using a machine learning approach as outlined in Yang et al. (2020) (Figures S5 - S6). Annually averaged maps of net primary production (NPP) were obtained using three different productivity algorithms, which included the Eppley Vertically Generalized Production Model (Eppley-VGPM) (Behrenfeld & Falkowski, 1997), the updated Carbon-Based Productivity Model (CbPM2) (Behrenfeld et al., 2005) and the Carbon, Absorption, and Fluorescence Euphotic-resolving model (CAFE) (Silsbe et al., 2016) (Figure S7). Level 3 satellite chlorophyll-a concentration data were obtained from the NASA Ocean Color data center (Figure S8), with all of the satellite-based data (including NPP) obtained from the Ocean Productivity Group at Oregon State University. Additional model validation is discussed in Section 3.1.

2.3.1 Model Parameterization and Spinup

Further details on the formulation and parameterization of NitrOMZ are discussed in Bianchi et al. (2022). Briefly, we estimated uncertain model parameters by optimizing a one-dimensional version of the model against a cost functioned designed to evaluate squared errors between model estimates and local observations of tracers and N transformation rates from the ETSP (Kalvelage et al., 2013; Ji et al., 2015; Peng et al., 2016; Babbin et al., 2017, 2020). Based on the optimization, we implement a low-cost parameter set with good comparisons to observed N_2O and NO_2^- profiles (Opt_{sel} from Bianchi et al. (2022), with parameter values in Table S4) into ROMS-BEC. The model is initially run for 20 years before evaluating against the validation products discussed in Section 2.3 and in situ ETSP observations from Kalvelage et al. (2013), Cornejo and Farías (2012), and Krahmann et al. (2021).

Based on this first comparison, we applied additional tuning to (1) bring surface concentrations of NO_2^- and NH_4^+ closer to zero and (2) increase the concentration of N_2O in suboxic waters to better match the magnitude of observed subsurface N_2O maxima in the ETSP OMZ. This was accomplished by (1) slightly increasing the maximum NH_4^+ and NO_2^- oxidation rates (k_{ao} and k_{no}, respectively, see supporting information S2) and (2) slightly widening the difference between exponential O_2 inhibition thresholds for NO_2^- and N_2O reduction ($K_{den2}^{o_2}$ and $K_{den3}^{o_2}$, respectively). We implement the final parameter set into ROMS-BEC and run a 50 year-long simulation to obtain a steady-state solution (Figure S9).

The choice of parameters results in a high NH_4^+ oxidation rate (R_{ao}) just below the euphotic zone that mostly produces NO_2^- ($R_{ao}^{no_2}$) due to high O_2 concentrations. As O_2 becomes scarce, R_{ao} decreases, yet production of N_2O ($R_{ao}^{n_2o}$) relative to NO_2^- increases following equations (1) and (2). Consumption of N_2O within anoxic waters occurs as all denitrification steps proceed without O_2 inhibition (consumption >> production). Similar to Babbin et al. (2015) and Bianchi et al. (2022), we model a progressive O_2 inhibition of the three denitrification steps ($K_{den1}^{O_2} > K_{den2}^{O_2} > K_{den3}^{O_2}$). Therefore, incomplete denitrification is allowed to occur at low but non-zero O_2 as NO_3^- reduction and NO_2^- reduction (R_{den1} and R_{den2}, respectively) proceed while N_2O reduction (R_{den3}) is inhibited (consumption < production).

2.4 N_2O Balance and Tracer Decomposition

To track the evolution of N_2O from different pathways, we decompose N_2O into four tracers that keep track of N_2O sources in the model domain:

$$N_2O = N_2O_{den} + N_2O_{nit} + N_2O_{atm} + N_2O_{bou}. \tag{6}$$

Each of the tracers in equation (6) follows a separate conservation equation (see supporting information S3), and is affected by a specific production process, by air-sea gas fluxes, transport from the boundaries, and destruction by the last step of denitrification (N_2O reduction, R_{den3}). By construction, the conservation equations for the individual tracers sum up to the conservation equation for N_2O (equation (5)), so that equation (6) can be considered a linear tracer decomposition.

Specifically, N_2O_{nit} tracks local production by nitrification (R_{ao}^{n2o}, equation (2)) whereas N_2O_{den} tracks production by denitrification ($R_{den2}^{n_2o}$, equation (3)) as outlined in Section 2.2.1 (pathways 3 and 6, respectively, in Figure 1). The remaining tracers, N_2O_{atm} and N_2O_{bou}, are designed to track N_2O originating from the atmosphere and from production sources outside the regional ROMS domain, respectively. Saturated N_2O forced from the model boundaries (assuming an atmospheric N_2O concentration of 300 ppb) can be interpreted as originating from air-sea equilibrium with the atmosphere, whereas supersaturated N_2O is linked to production outside the regional model domain. We therefore split the N_2O forced into the domain into a saturation component (N_2O_{atm}) and a supersaturation component (N_2O_{bou}) transported into the domain.

To close separate biogeochemical budgets for each N_2O tracer, we similarly decomposed the N_2O reduction rate (R_{den3}, equation (4) and pathway 7 in Figure 1) and N_2O air-sea flux (Φ^{n2o}, pathway 8 in Figure 1) to track losses with respect to the decomposed N_2O concentrations from within the domain:

$$R_{den3} = R_{den3}^{den} + R_{den3}^{nit} + R_{den3}^{bou} + R_{den3}^{atm} \tag{7}$$

$$\Phi_{n2o} = \Phi_{n2o}^{den} + \Phi_{n2o}^{nit} + \Phi_{n2o}^{bou} + \Phi_{n2o}^{atm}. \tag{8}$$

Here, each consumption term by denitrification is proportional to the individual tracer concentration in a linear fashion. Air-sea fluxes follow the same formulation as N_2O (modeled according to Wanninkhof (1992) using a constant atmospheric mixing ratio of 300 ppb), but with mixing ratios set to zero for all tracers except N_2O_{atm}, for which it is set to the total value. Therefore, while initially saturated at the boundaries, the concentration of N_2O_{atm} can drop below saturation following consumption via R_{den3}^{atm}. When N_2O-undersaturated water is exposed to the surface, atmospheric in-gassing will increase N_2O_{atm} until N_2O reaches saturation. As such, N_2O_{atm} tracks both domain ingassing of N_2O and import of saturated N_2O from the model boundaries, whereas N_2O_{bou} exclusively tracks import of the supersaturation component. To initialize the decomposition, the initial 3-D N_2O was separated into N_2O_{atm} and N_2O_{bou} while N_2O_{nit} and N_2O_{den} were set to zero everywhere; thus these tracers exclusively track production within the domain after initialization (Figure S10).

Finally, to elucidate the sources of N_2O air-sea flux over the OMZ, we defined a budget domain that captures the extent of the ETSP OMZ horizontally (dashed blue box in Figure 3a) and vertically from the surface to 750 m depth. We configured ROMS output to close biogeochemical budgets within each grid cell, allowing us to scale them up to arbitrary 3-D domains within the model:

$$\frac{d[\mathrm{C}]}{dt} = J + T - \Phi. \tag{9}$$

Here, $d[\mathrm{C}]/dt$ is the climatological N_2O rate of change calculated as the difference between snapshots at the beginning and end of each month; T the transport component calculated as the divergence of advection/diffusion fluxes, J the sum of biological sources and sinks, and Φ the air-sea flux controlled by gas exchange.

3 Results

3.1 Model Validation

Figure 3 shows the extent and thickness of the modelled OMZ from model years 46 - 50 (Figure 3a) and various validation products (Figure 3b - e). The simulated OMZ is centered offshore of the Peruvian and Ecuadorian coastline at roughly 8^oS and extends from the Galapagos islands at the equator to nearly 15^oS. This represents a displacement both equatorward and offshore compared to observations, which suggest a more coastal OMZ between southern Peru and Chile. The thickness of waters with less than 10 $mmol$ O_2 m^{-3} ranges mostly between 300 - 500 m and extends to roughly 105^oW. Considering that O_2 reconstructions based on spatial interpolation of in situ profiles underestimate the volume of anoxic waters (Bianchi et al., 2012), the inset bar plot in Figure 3a suggests that the ROMS simulation is overall within range of OMZ volume predictions across several thresholds ranging from 5 $mmol$ O_2 m^{-3} (Kwiecinski & Babbin, 2021) to 20 $mmol$ O_2 m^{-3} (H. Garcia et al., 2019a; Bianchi et al., 2012; Dunn, 2012).

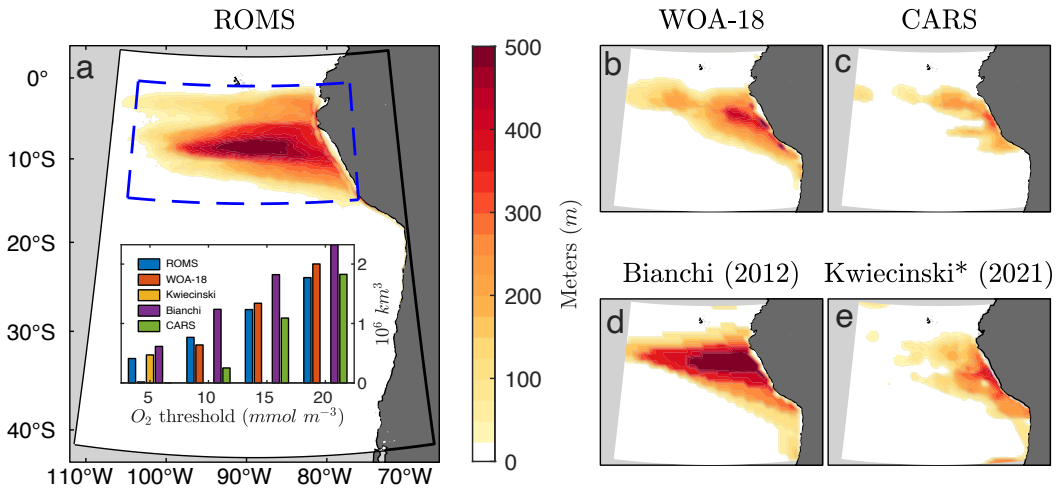

Figure 3. (a) ROMS Peru-Chile 10 km domain, with annually averaged OMZ thickness (O_2 < 10 $mmol$ m^{-3}) from model years 46 - 50. The inset bar plot shows OMZ volume from ROMS and validation products based on 5, 10, 15, and 20 $mmol$ m^{-3} thresholds. The N_2O budget region is also shown as the area encompassed by dashed blue lines, extending vertically from the surface to 750 m. (b-d) OMZ thickness (O_2 < 10 $mmol$ m^{-3}) from World Ocean Atlas 2018, CSIRO Atlas of Regional Seas (CARS), and the Objective mapping 2 product from Bianchi et al. (2012). (e) OMZ thickness (O_2 < 5 $mmol$ m^{-3}) from Kwiecinski and Babbin (2021).

Taking into account the slight equatorward geographic shift in the model OMZ, nitrogen tracer (NO_3^-, NO_2^-, and N_2O) sections at 250 m in Figure 4a - c compare well with validation products (Figure 4d - f). The simulation is able to replicate the expected draw-down of NO_3^- and N_2O and increase in NO_2^- within the core of the OMZ, characteristics of step-wise denitrification. The magnitude and spatial patterns of open ocean concentrations are similarly reproduced, such as the low NO_3^- and N_2O concentrations observed in the subtropical gyre at 25^oS. The oxic to suboxic transition zone (inshore of the 20 $mmol$ O_2 m^{-3} contour in Figure 4) also reveals an increase in N_2O concentrations that skillfully reproduces observational reconstructions discussed in Section 2.2.

The vertical subsurface structure and concentration magnitudes of nitrogen tracers in the ETSP OMZ are shown in Figure 4g - i. Model profiles centered over the OMZ

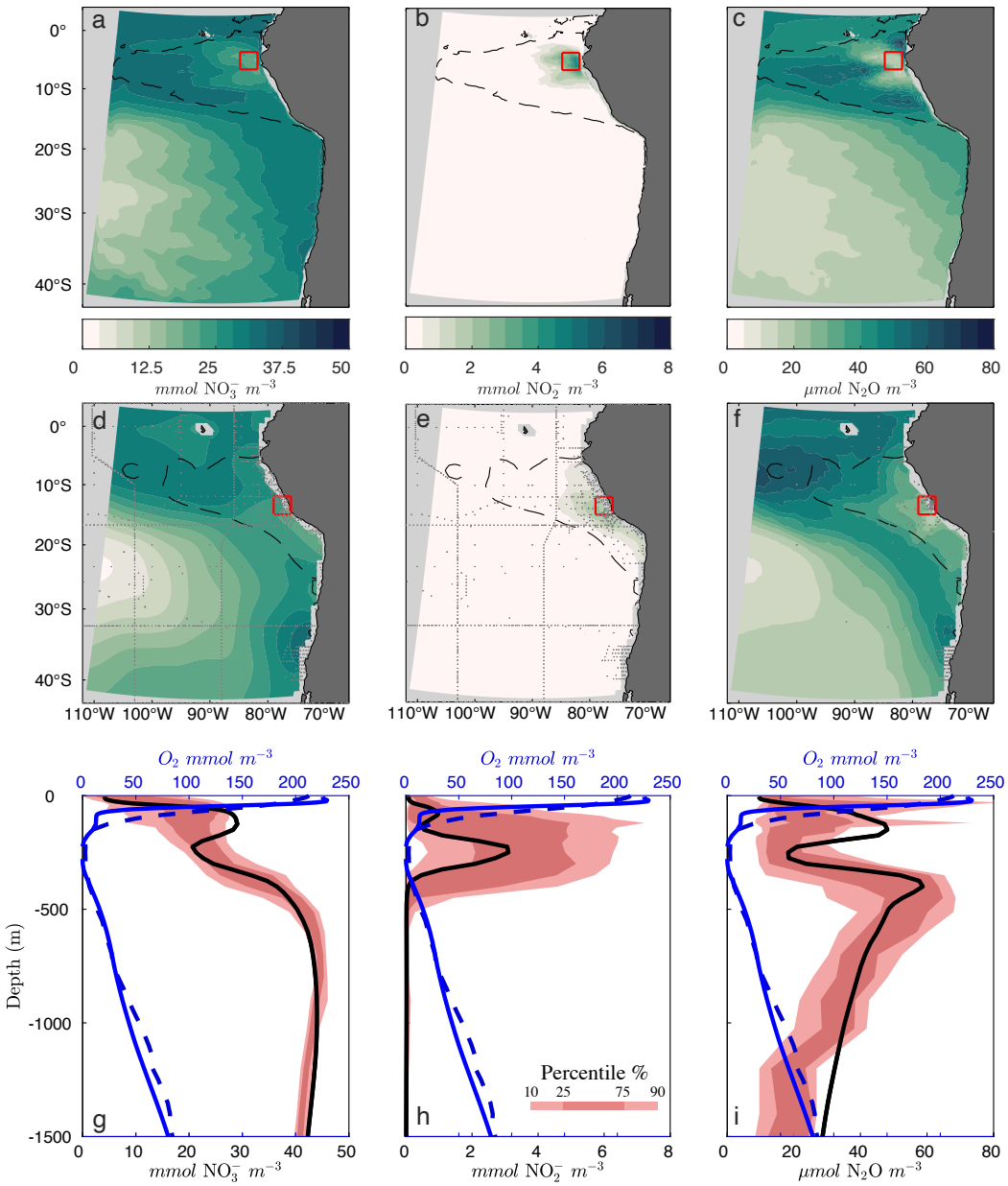

Figure 4. (a-c) ROMS annually averaged NO_3^-, NO_2^-, and N_2O at 250 m from model years 46 - 50. Dashed black lines highlight the 20 $mmol$ O_2 m^{-3} contour. (d-f) NO_3^-, NO_2^-, and N_2O at 250 m from World Ocean Atlas 2018 and machine learning estimates, respectively. Grey markers show the location of shipboard samples. (g-i) Averaged profiles of NO_3^-, NO_2^-, and N_2O from ROMS (black curves) extracted from within the OMZ (red boxes in panels a - c). Shaded regions show the 10th/90th and 25th/75th percentiles of shipboard observations from Kalvelage et al. (2013), Cornejo and Farías (2012), and Krahmann et al. (2021) conducted within the red boxes in panels d - f. Solid blue curves show ROMS O_2 whereas the dashed blue curves show averaged World Ocean Atlas 2018 O_2 over the shipboard sampling region.

show low concentrations at the surface for NO_3^-, NO_2^-, and N_2O. As depth increases, local maxima in NO_2^- and N_2O can be seen at ∼100 m that correspond to low but non-

zero O_2. Just below this depth, where O_2 drops further to anoxic levels, local minima in NO_3^- and N_2O appear along with a large peak in NO_2^- of roughly 3 $mmol\ m^{-3}$. Beneath the anoxic OMZ, a second N_2O peak appears of slightly greater magnitude ($\sim$60 μmol N_2O m^{-3}) to the shallower maxima ($\sim$50 μmol N_2O m^{-3}). Depth-dependent distributions from shipboard measurements (Kalvelage et al., 2013; Cornejo & Farías, 2012; Krahmann et al., 2021) through the OMZ (pink shading) generally show good agreement between model and observations as O_2 increases and decreases vertically. Note that the geographical location of shipboard measurements differs from the ROMS averaging box due to the equatorward and offshore OMZ shift discussed above. Despite this geographical bias, Figures 4g - i demonstrate similarity in the expression of anaerobic nitrogen cycle processes at locations with comparable O_2 profiles. Remaining inconsistencies, such as the shallower depth of the observed upper N_2O maxima, can be explained by the proximity of observations to the coast, as compared to the more offshore location used to average model profiles.

Finally, given the importance of accurately representing water column denitrification, we compared total fixed nitrogen loss in ROMS via denitrification and anammox to other ETSP estimates (Figure 5). Both processes contribute roughly 50% to OMZ N-loss throughout the year, with seasonal variability mostly driven by changes in denitrification rates (red shading). The total water-column fixed nitrogen loss in the model is 25.2 TgN yr^{-1}, within the range of observational estimates for the region (Deutsch et al., 2007; Bianchi et al., 2012; DeVries et al., 2013; Yang et al., 2017). Thus, despite a geographic shift, the model produces a realistic OMZ and associated nitrogen cycle tracers and rates.

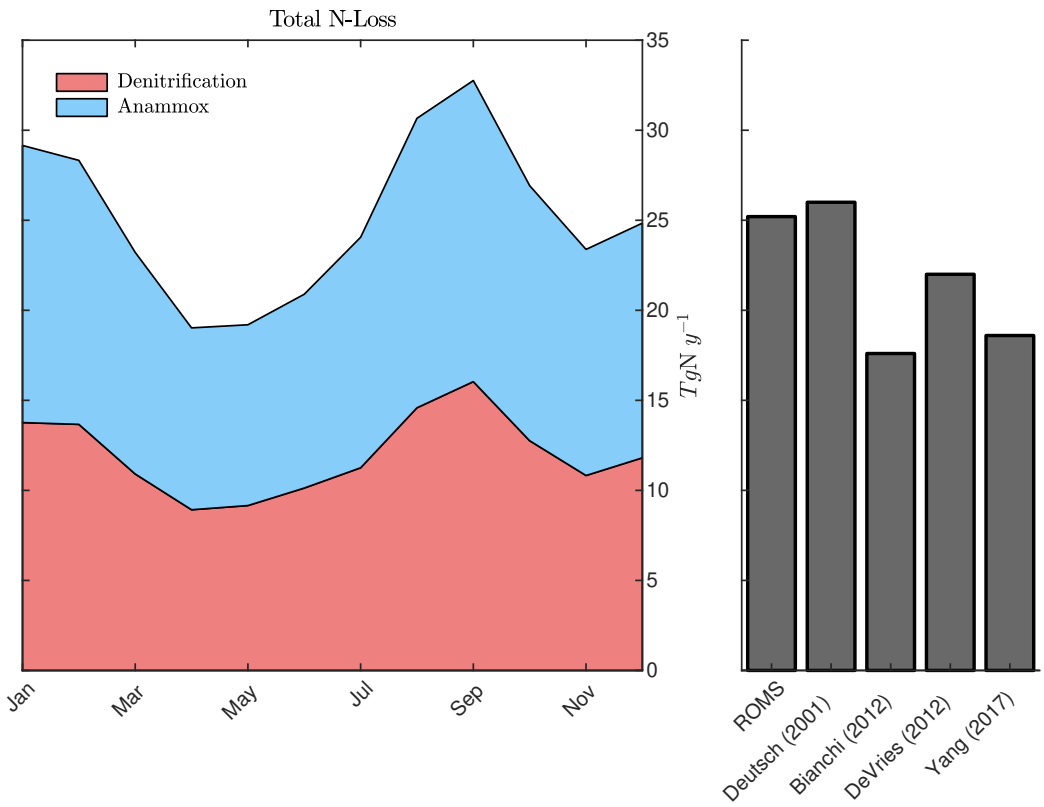

Figure 5. (left) Monthly averaged fixed nitrogen loss from ROMS via canonical denitrification and anammox from models year 46 - 50. (right) ETSP estimates of total annual averaged nitrogen loss from ROMS, Deutsch et al. (2007), Bianchi et al. (2012), DeVries et al. (2013), and Yang et al. (2017).

3.2 ETSP N_2O Production

A transect crossing the core of the model OMZ shows that N_2O production and consumption rates from denitrification are strongly influenced by O_2 concentrations (Figure 6a). Within the anoxic core, N_2O reduction to N_2 ($R^{n_2}_{den3}$) exceeds NO_2^- reduction to N_2O ($R^{n_2o}_{den2}$), causing widespread net N_2O consumption (red shading) of nearly 0.1 μmol N m^{-3} d^{-1}. The resulting N_2O and NO_2^- transects (Figure 6c and 6d) show consistent offshore subsurface N_2O minima coinciding with peak concentrations of NO_2^- at the same depth range. These patterns suggests that all three denitrification steps proceed with minimal O_2 inhibition within the OMZ core, supporting a zone of active fixed N-loss.

Along the exterior of the OMZ core, O_2 gradients preferentially inhibit N_2O reduction to N_2 ($R^{n_2}_{den3}$) and allow incomplete denitrification to proceed. Accordingly, net N_2O consumption transitions to net production (blue shading) of a similar $\sim$0.1 μmol N m^{-3} d^{-1} magnitude (Figure 6a). Beyond suboxic waters, net production from denitrification ceases. In contrast, maximum N_2O production from NH_4^+ oxidation ($R^{n_2o}_{ao}$, Figure 6b) peaks at roughly 0.01 μmol N m^{-3} d^{-1} and is largely restricted to a thin, mostly oxygenated layer at roughly 100 - 150 m that mirrors vertical maxima in POC flux (not shown), with little amplification at low O_2.

The relative contributions from the N_2O tracer decomposition (Figure 6e - h) highlight the disparity between N_2O sources. At the surface, atmospheric ingassing allows

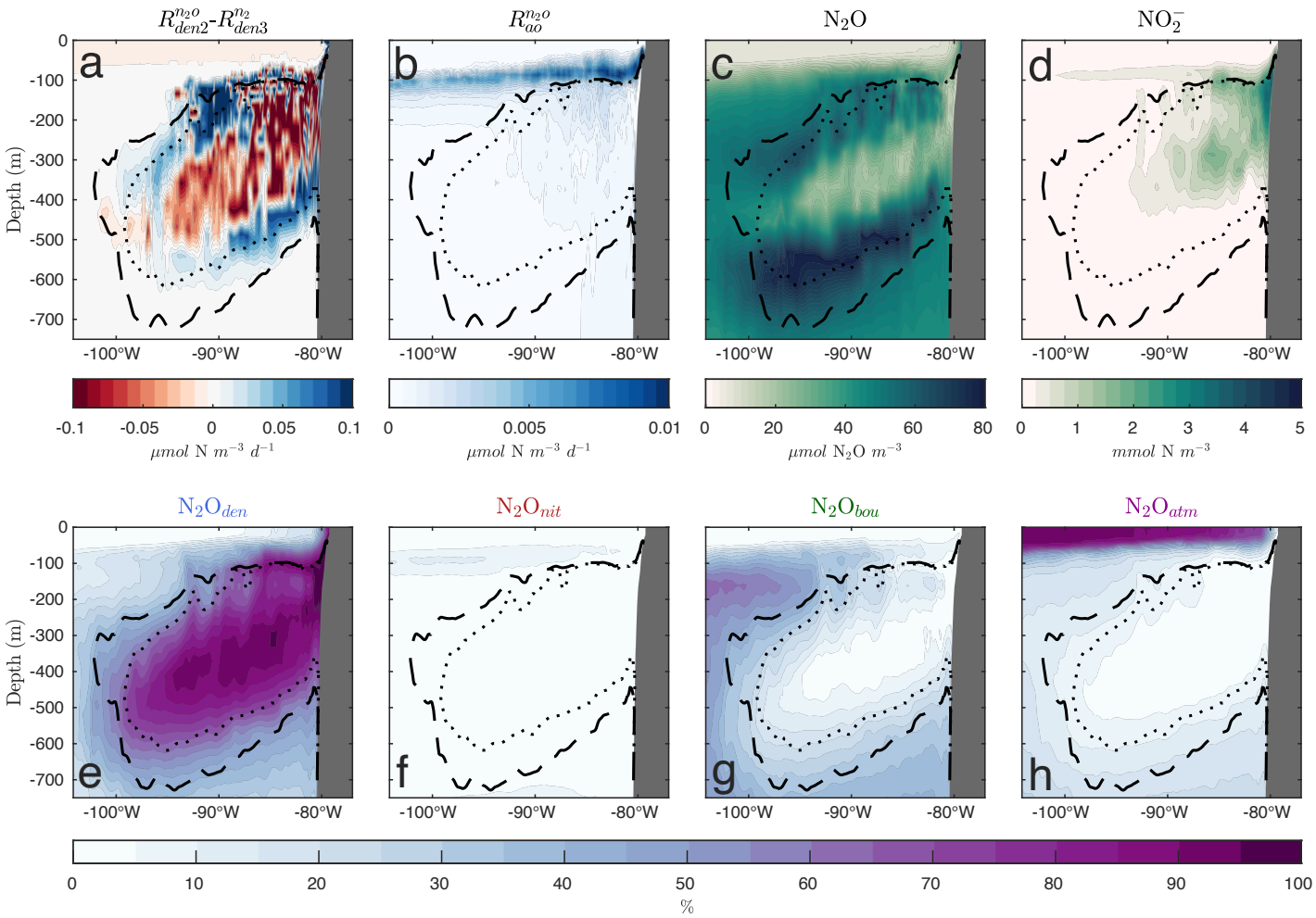

Figure 6. (a) Annually averaged net N_2O production from denitrification for model years 46 - 50 along a transect from the coast at 8^oS. The dotted and dashed black curves in highlight the 5 and 10 $mmol$ O_2 m^{-3} contours, respectively. (b-d) Same as in panel (a), but for N_2O production from nitrification (b), N_2O (c), and NO_2^- (d). Panels (e) - (h) show the relative contributions to N_2O for each decomposed N_2O tracer (N_2O_{den}, N_2O_{nit}, N_2O_{bou}, and N_2O_{atm}).

saturated N_2O (N_2O_{atm}) to dominate (Figure 6h), especially offshore. Within the anoxic OMZ core, despite vigorous net N_2O consumption (Figure 6a), residual N_2O concentrations of $\sim$20 μmol m^{-3} persist (Figure 6c), and are nearly completely attributed to N_2O denitrification (N_2O_{den}, Figure 6e). As O_2 increases beyond suboxic levels, the contribution of N_2O_{den} diminishes, while contributions from supersaturated and saturated N_2O from the boundaries (N_2O_{bou} and N_2O_{atm}, respectively) account for the remainder. In contrast, N_2O from nitrification (N_2O_{nit}, Figure 6f) does not contribute more than 10%, with a maximum at roughly 100 m depth, suggesting that incomplete denitrification is the main contributor ($\mathcal{O}(10)$ times greater production) to local N_2O production throughout the OMZ.

Notably, the contributions from supersaturated and saturated N_2O transported into the OMZ from the model domain boundaries (N_2O_{bou} and N_2O_{atm}, respectively) are rapidly reduced at low O_2, showing consumption of externally derived N_2O within the OMZ core. Additionally, while production from incomplete denitrification is generally confined to

suboxic waters (Figure 6a), significant concentrations of N_2O_{den} in oxygenated waters suggest export of N_2O_{den} out of the OMZ. Together, these results highlight an important role for circulation in redistributing N_2O within the ETSP.

3.3 Contributions of Different Processes to the N_2O Balance

Figure 7 shows vertically-integrated N_2O sources minus sinks (J terms) over the OMZ budget region, and the annual time-series of total integrated net production for N_2O and each decomposed tracer. In general, net N_2O production ($J^{n_2o}_{tot}$, black line in the time-series) is positive for each month with the exception of June, and reveals higher rates beginning in August that persist through December. Production is predominantly driven by denitrification ($J^{n_2o}_{den}$, blue line), which also drives the bulk of monthly variability seen in $J^{n_2o}_{tot}$. In contrast, production from nitrification ($J^{n_2o}_{nit}$, red line) is net positive throughout the year, but only accounts for a small proportion of the N_2O production. Tracers that lack domain production sources (N_2O_{bou} and N_2O_{atm}) show consistent consumption rates throughout the year.

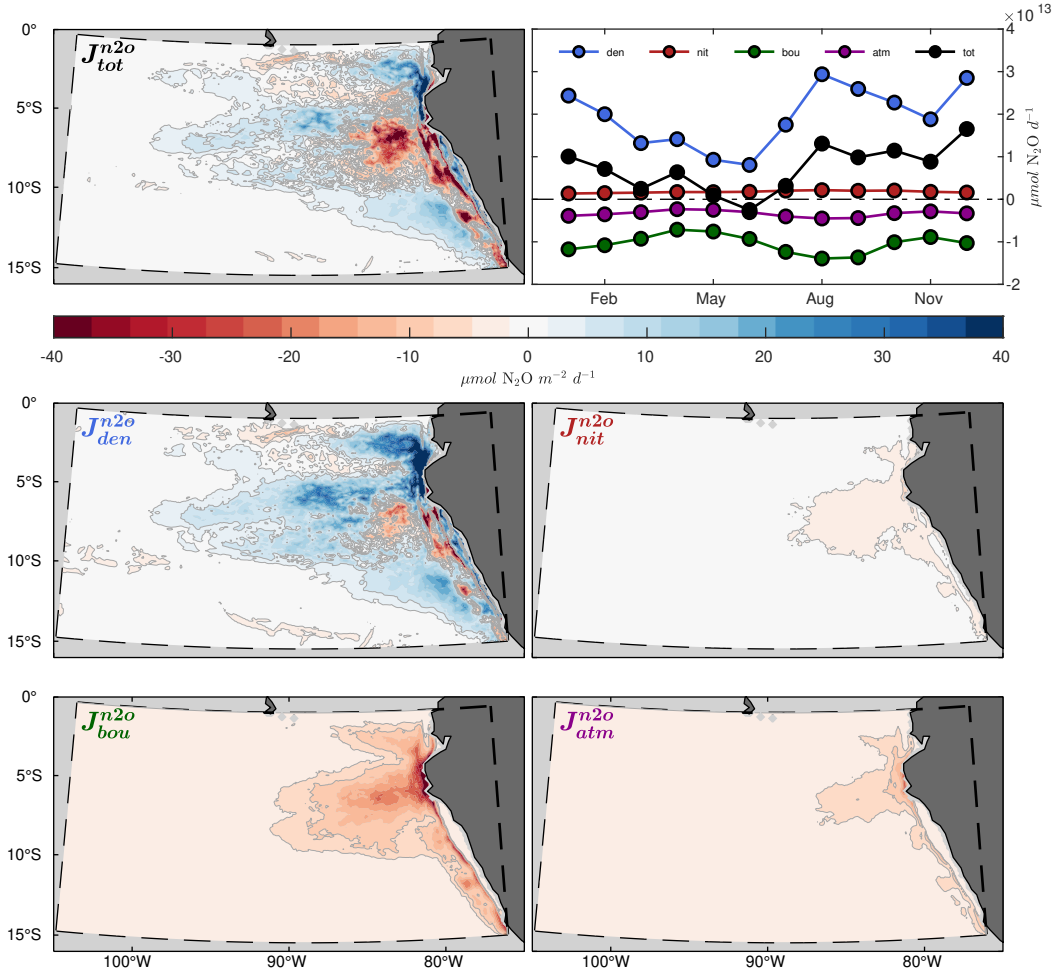

Figure 7. (top left) Vertically integrated sources-minus-sinks (J) for N_2O from the OMZ budget domain, annually averaged from model years 46 - 50. (top right) Time-series of integrated sources-minus-sinks for N_2O (black) and the decomposed N_2O tracers. (bottom panels) Same as in the top left panel, but for each of the decomposed N_2O tracers. Positive values (production) are shown in blue, and negative values (consumption or removal) in red.

Vertically-integrated total N_2O production ($J_{tot}^{n_2o}$) and denitrification-derived production ($J_{den}^{n_2o}$) shown in Figure 7 are similar and reveal a hot-spot of vigorous net consumption (red shading) centered at roughly 8^oS and 80^oW that abruptly transitions to net production (blue shading) in the surrounding ocean. The remaining tracers reveal similar hot-spots of consumption near the coast, especially supersaturated N_2O from the model boundaries ($J_{bou}^{n_2o}$). Integrated N_2O consumption from nitrification ($J_{nit}^{n_2o}$) is balanced by production immediately adjacent to the coastline and in the offshore region that ultimately leads to net production within the budget domain. The region is therefore characterized by a coastal hot-spot of net N_2O consumption that depletes both locally produced N_2O (N_2O_{den} and N_2O_{nit}, blue and red lines respectively) and remote N_2O originating from outside the model domain (N_2O_{bou} and N_2O_{atm}, green and purple lines respectively). Outside the coastal hot-spot, N_2O production from denitrification overcompensates for the consumption at the coast and makes the OMZ a net source of N_2O in all months, with the exception of June. As expected at steady-state, the divergence of advective and diffusive fluxes (T terms) for each N_2O tracer, shown in Figure S11, largely balances the sources minus sinks in Figure 7.

The total N_2O air-sea flux ($\Phi_{tot}^{n_2o}$, black lines in Figure 8) peaks in July and is positive throughout the year, indicating the surface ocean of the ETSP OMZ as a constant source of N_2O to the atmosphere with higher outgassing rates throughout upwelling season (boreal summer). The major contributing components to the flux are supersaturated N_2O from the model boundaries ($\Phi_{bou}^{n_2o}$) and locally produced N_2O from denitrification ($\Phi_{den}^{n_2o}$), which exhibit similar seasonal cycles as in the total flux ($\Phi_{tot}^{n_2o}$), albeit with different geographical distributions. The spatial pattern of $\Phi_{tot}^{n_2o}$ can be described as a combination of $\Phi_{bou}^{n_2o}$ and $\Phi_{den}^{n_2o}$ patterns; $\Phi_{den}^{n_2o}$ is concentrated near the coast with a structure closely mirroring the coastal hot-spot of consumption shown by Figure 7, whereas $\Phi_{bou}^{n_2o}$ takes place mostly along the northern boundary of the budget region (albeit with maximum outgassing near the coast). Since the N_2O_{atm} tracer can be consumed via N_2O reduction within the domain (section 2.4), $\Phi_{atm}^{n_2o}$ similarly tracks the coastal hot-spot, but reveals oceanic ingassing at the surface, peaking in July, which brings N_2O_{atm} back towards saturation. Finally, the magnitude of air-sea flux from local nitrification ($\Phi_{nit}^{n_2o}$) is small but net positive, and shows a similar July maximum peaking near the coast.

3.4 N_2O Balance

A schematic of the annual N_2O balance (Figure 9) shows that total OMZ N_2O production is dominated by incomplete denitrification (174 $Gg\,N\,y^{-1}$), whereas nitrification contributes a smaller fraction (18 $Gg\,N\,y^{-1}$). Conversely, consumption of both saturated and supersaturated N_2O from the model boundaries (N_2O_{atm} and N_2O_{bou}) drives a net N_2O loss (106 and 34 $Gg\,N\,y^{-1}$ respectively). The excess production makes the OMZ a net N_2O source to the atmosphere (51 $Gg\,N\,y^{-1}$). This production takes place predominantly on the fringe of the OMZ both vertically and horizontally, where thick suboxic layers support net N_2O accumulation from the denitrification pathway (Figures 6 and 7).

The budget also suggests that the corresponding outgassing pathways from local production sources are somewhat inefficient; the annual export of 125 and 7 $Gg\,N\,y^{-1}$ of N_2O_{den} and N_2O_{nit} (respectively) suggests that ∼72% and ∼39% of their net production ($J_{den}^{n_2o}$ and $J_{nit}^{n_2o}$, respectively) ultimately avoids outgassing within the budget domain. Yet despite the surprising magnitude of these production export rates, high net import rates of N_2O_{bou} and N_2O_{atm} from the model boundaries (188 and 38 $Gg\,N\,y^{-1}$, respectively) drive an annual net source of 94 $Gg\,N\,y^{-1}$ into the OMZ region. Separating the advective fluxes into zonal, meridional, and vertical components reveals zonal fluxes along the western boundary of the domain as the primary interface of N_2O exchange with the surrounding ocean, organized as alternating narrow bands of N_2O import (Figure S12e, red shading) and export (blue shading). The net transport is driven by supersat-

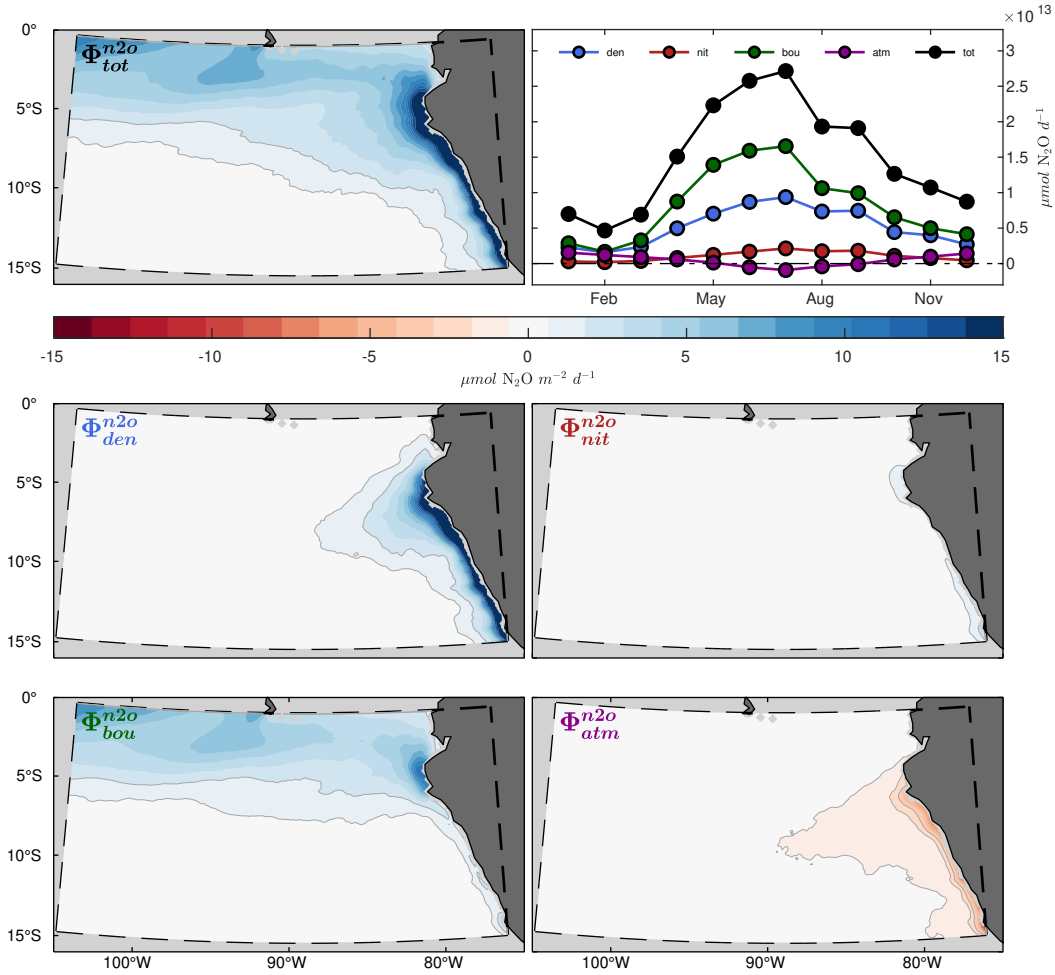

Figure 8. Same as in Figure 7, but for air-sea flux (Φ) of N_2O

urated N_2O (N_2O_{bou}) supplied through the boundaries (Figure S12c), with the most intense import along the equator at roughly 150 m depth (see also Figure 6g). In contrast, denitrification-driven export (Figure S12a) is focused further to the south (roughly 8^oS) and at deeper depths (200 - 500 m, also evident in Figure 6e).

After accounting for boundary exchanges, local subsurface production and consumption, and periodic ingassing of N_2O_{atm} (Figure 8), all tracers reveal net outgassing with $\Phi^{n_2o}_{bou}$ and $\Phi^{n_2o}_{den}$ contributing ~56% and ~34% (respectively) to the annual 152 $Gg\,N\,y^{-1}$ outgassed to the atmosphere. Thus, what emerges from the above descriptions is an ETSP OMZ that is characterized by: (1) A consistent supply of N_2O_{bou} and N_2O_{atm} from predominantly zonal subsurface currents in the tropical band (Figures S11, S12c, and S12e); (2) Advection of all N_2O tracers into a coastal hot-spot where vigorous consumption leads to significant N-loss; (3) Net N_2O production predominantly by denitrification within suboxic gradients surrounding the OMZ (Figure 7); (4) Significant export of N_2O_{den} into the exterior ocean (Figures S11 and S12); (5) Consumption of locally produced and externally derived N_2O; and (6) Year-round air-sea flux of N_2O driven predominantly by imported N_2O_{bou} and locally produced N_2O_{den} that upwell and outgas along the northern extent of the OMZ domain and along the coast, respectively (Figure 8).

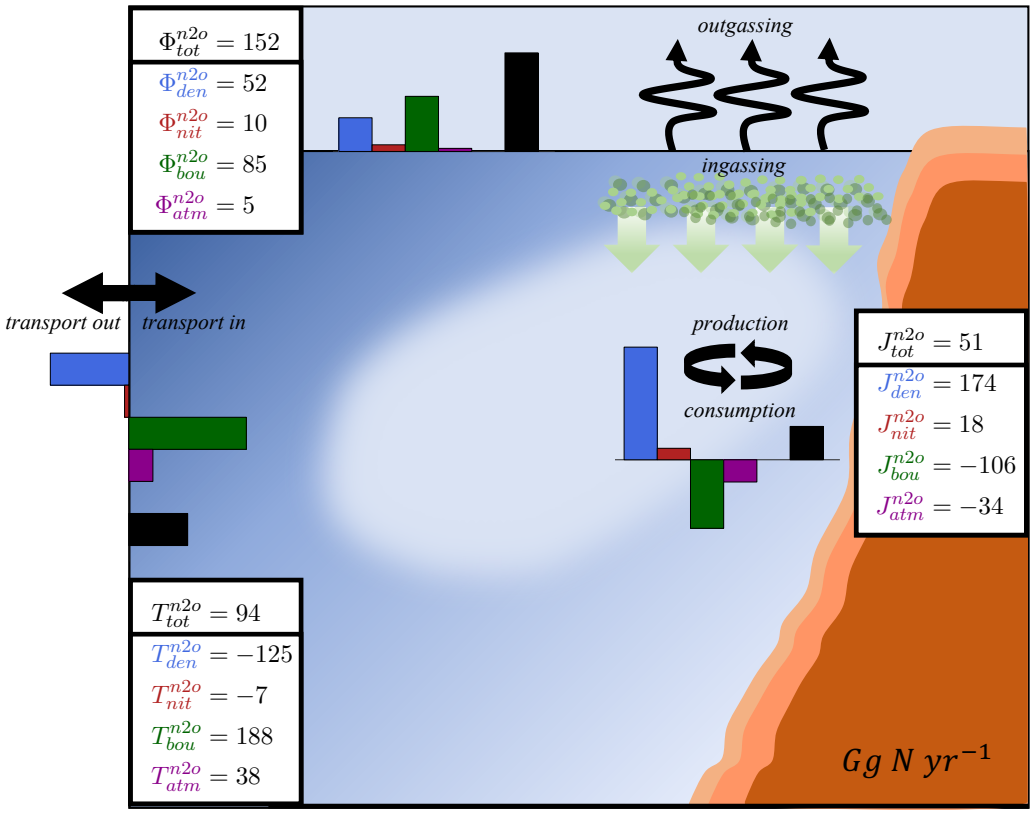

Figure 9. Schematic of the ETSP OMZ N_2O budget, with calculated averages ($Gg\,N\,y^{-1}$) of net air-sea flux (Φ), advection (T), and sources-minus-sinks (J) from model years 46 - 50. Bar plots indicate both the direction of, and relative magnitude of, budget averages.

4 Discussion and Conclusions

We developed a climatological, eddy-resolving simulation of the ETSP OMZ that reproduces the main patterns in the spatial distribution of observed nitrogen tracers and transformation rates. Despite enhanced yields at low O_2, we find almost negligible local contributions from nitrification; rather, maximum N_2O production rates from NH_4^+ oxidation (R^{n2o}_{ao}) follow vertical maxima in POC flux which occur well above the oxycline throughout much of the domain east of -90°W (Figure 6). Closer to shore, as the OMZ core shoals to $\sim$100 m, production from nitrification (J^{n2o}_{nit} in Figure 7) suggests that N_2O_{nit} is subsequently mixed into anoxic waters and consumed via N_2O reduction. The major contribution of nitrification to N_2O production takes place immediately adjacent to the coast, where low O_2 waters at shallow depths lead to enhanced production and an efficient outgassing route. As a result, the air-sea flux pattern in Figure 8 shows negligible contributions from nitrification (Φ^{n2o}_{nit}) throughout the domain, with the exception of coastal outgassing driven by upwelling. While the contribution from nitrification to N_2O production in NitrOMZ is sensitive to the choice of the parameters in equation (1), the values used in this study are constrained by observations (Section 2.3.1) and fall within range of previous estimates (Ji et al., 2018; Santoro et al., 2021) which similarly suggest weak nitrification production. Therefore, similar to the results of Ji et al. (2015) and Babbin et al. (2015), our simulation suggests that local production from nitrification is not a dominant pathway for N_2O outgassing flux in this region.

Instead, N_2O production is dominated by incomplete denitrification which takes place along the suboxic fringes of the anoxic OMZ core (Figure 6a, Figure 6e, and Figure 7), in agreement with recent studies (Babbin et al., 2015; Ji et al., 2018). In general, the three step-wise denitrification rates shows a strong seasonal dependence and are primarily controlled by the timing of organic matter supply from the euphotic zone (Figure S13) rather than variability in low O_2 volumes throughout the year (Figure S14). Within the anoxic core of the OMZ, rapid N_2O consumption rates (Figure 6a) indicate short residence times for N_2O produced via NO_2^- reduction (N_2O_{den}) due to the strong coupling between denitrification steps at low O_2. Significant net N_2O production by denitrification (J_{den}^{n2o}) occurs where high rates of vertical POC flux overlap with an anoxic to suboxic O_2 gradient; there, the difference in O_2 tolerance thresholds leads to a relatively small residual between the large NO_2^- and N_2O reduction rates within the domain (Babbin et al., 2015). As oxic organic matter remineralization stops within the anoxic OMZ core, this leads to the characteristic double peak structure in N_2O profiles (Figure 6c) bounding the OMZ throughout most of the domain.

Spatially, the vertical depth range occupied by anoxic to suboxic gradients plays a key role in determining regions of net production or consumption via the denitrification pathway. For instance, the integrated J_{den}^{n2o} in Figure 7 reveals consumption along the northern extent of the Peruvian coast at roughly 8^oS; considering this pattern, Figure 6a shows relatively sharp O_2 gradients above and below the OMZ around -85°W, indicating that N_2O consumption is particularly strong near the coast, where relatively thin but shallow suboxic layers are found. In contrast, suboxic layers become thicker further offshore, resulting in conditions more favorable to N_2O production. Therefore, the high rates of coastal outgassing observed in Figure 8 are at least partially driven by net transport from more productive surrounding waters (Figure S11).

Our results demonstrate the role of advection in redistributing supersaturated N_2O within the ETSP. Notably, the EUC and SSCC are revealed as zonal conduits controlling the import of supersaturated N_2O (N_2O_{bou}) from the boundaries (and thus, outgassing-favorable N_2O) into the OMZ domain. This is demonstrated by the large fractional contributions to N_2O at 150 m throughout the eastern extent of the transect in Figure 6g, which match subsurface patterns in Figure S12c. These results are consistent with those from Yang et al. (2020), who highlighted the tropics in the Eastern Pacific as an important outgassing region with seasonality driven predominantly by the timing of upwelling (May to September). While a significant fraction of the imported N_2O is ultimately advected into the anoxic OMZ to be consumed (Figures 6g and 7), the remainder is responsible for the bulk ($\sim$56%) of the outgassing flux over the OMZ domain. As the N_2O budget and boundary export schematic in Figures 9 and S12 show, circulation also plays a key role in exporting the majority (roughly 72%) of local denitrification-derived N_2O production (J_{den}^{n2o}) out of the OMZ budget domain. Much of this export takes place along the western boundary (Figure S12), but at more southerly latitudes and at deeper depths compared to the import of supersaturated N_2O from the boundaries (T_{bou}^{n2o}). Unfortunately, our regional simulations do not allow us to explore the fate of this N_2O. Global or basin-wide simulations would enable tracking the interplay of N_2O sources and sinks within and outside OMZs. A portion of the denitrification-derived N_2O export may recirculate back into the eastward equatorial currents, or could instead add to N_2O concentrations in offshore waters, such a those observed by Santoro et al. (2021).

The residual between rapid N_2O production and consumption by denitrification is heavily coupled to O_2 dynamics and thus a major portion of N_2O outgassing in this region is likely sensitive to future changes in OMZ magnitude and geometry. Observations suggest that deoxygenation over the past 50 years has led to expansion of OMZ volumes and shoaling of the upper oxycline (Stramma et al., 2008; Schmidtko et al., 2017). Yet, whether this has caused a positive or negative impact on N_2O production likely depends on the relative changes of anoxic versus suboxic volumes. If future climate change

results in an increase in the volume of suboxic waters, as suggested by Earth system model projections (Cabré et al., 2015; Kwiatkowski et al., 2020; Busecke et al., 2019), it would increase production from both incomplete denitrification and nitrification, leading to a positive climate feedback. Conversely, an increase in the volume of anoxic waters may drive enhanced N_2O consumption and constitute a negative climate feedback.

Future changes in the oxycline depth via projected stratification or wind changes (Kwiatkowski et al., 2020; Busecke et al., 2019; Bakun, 1990) may alter the coupling between local production and outgassing over OMZs, while also affecting the export of supersaturated N_2O into the nearby gyres. The lack of interannual forcing in this study also leaves gaps in understanding ENSO impacts. OMZ geometry and total denitrification rates are sensitive to ENSO variability (Yang et al., 2017), thus N_2O production and outgassing are likely to exhibit similar year-to-year changes. Interannually forced, high-resolution models capable of simulating both denitrification and nitrification-derived production are needed to resolve these emerging questions.

Open Research Section

The ROMS model code used to generate the simulation (Shchepetkin & McWilliams, 2005; Shchepetkin, 2015), and the MATLAB (MATLAB, 2020) scripts and output used to generate the figures shown in the paper, can be found at https://doi.org/10.5281/zenodo.7374360 (McCoy et al., 2022). Raw model output can be obtained from the Authors upon request. Biogeochemical validation data were provided by the World Ocean Atlas 2018 (H. Garcia et al., 2019a, 2019b), MEMENTO (Kock & Bange, 2015) and GLODAPv2 (Key et al., 2015; Lauvset et al., 2016) databases, with additional shipboard observations from Kalvelage et al. (2013), Cornejo and Farías (2012), and Krahmann et al. (2021). The MEMENTO database is administered by the Kiel Data Management Team at GEOMAR Helmholtz Centre for Ocean Research and supported by the German BMBF project SOPRAN (Surface Ocean Processes in the Anthropocene, http://sopran.pangaea.de). The database is accessible through the MEMENTO webpage (https://memento.geomar.de). AVISO satellite data used in model validation were processed by SSALTO/DUACS and distributed by AVISO+ at https://www.aviso.altimetry.fr with support from CNES. MODIS L3 ocean color data were obtained from the NASA/GSFC MODAPS Service website at https://oceancolor.gsfc.nasa.gov/l3/. The ERA-Interim dataset (Dee et al., 2011), which was used to force the model, was obtained from the European Centre for Medium-Range Weather Forecasts (ECMWF) at https://www.ecmwf.int. Thanks to ICDC, CEN, University of Hamburg for data support in obtaining ERA-Interim products.

Acknowledgments

This material is based upon work supported by the U.S. National Science Foundation under grant OCE-1847687. D.B. acknowledges support from the Alfred P. Sloan Foundation, and computational support by the Extreme Science and Engineering Discovery Environment (XSEDE) through allocation TG-OCE17001.

References

Anderson, L. A., & Sarmiento, J. L. (1994, 3). Redfield ratios of remineralization determined by nutrient data analysis. *Global Biogeochemical Cycles*, *8*(1), 65–80. Retrieved from `http://doi.wiley.com/10.1029/93GB03318` doi: 10.1029/93GB03318

Arévalo-Martínez, D. L., Kock, A., Löscher, C. R., Schmitz, R. A., Stramma, L., & Bange, H. W. (2015). Influence of mesoscale eddies on the distribution of nitrous oxide in the eastern tropical South Pacific. *Biogeosciences Discussions*, *12*(12), 9243–9273. doi: 10.5194/bgd-12-9243-2015

Babbin, A. R., Bianchi, D., Jayakumar, A., & Ward, B. B. (2015). Rapid nitrous oxide cycling in the suboxic ocean. *Science*, *348*(6239), 1127–1129. doi: 10.1126/science.aaa8380

Babbin, A. R., Buchwald, C., Morel, F. M., Wankel, S. D., & Ward, B. B. (2020). Nitrite oxidation exceeds reduction and fixed nitrogen loss in anoxic Pacific waters. *Marine Chemistry*, *224*(April). doi: 10.1016/j.marchem.2020.103814

Babbin, A. R., Peters, B. D., Mordy, C. W., Widner, B., Casciotti, K. L., & Ward, B. B. (2017). Multiple metabolisms constrain the anaerobic nitrite budget in the Eastern Tropical South Pacific. *Global Biogeochemical Cycles*, *31*(2), 258–271. doi: 10.1002/2016GB005407

Bakun, A. (1990). Global climate change and intensification of coastal ocean upwelling. *Science*, *247*(4939), 198–201.

Battaglia, G., & Joos, F. (2018). Marine N2O Emissions From Nitrification and Denitrification Constrained by Modern Observations and Projected in Multimillennial Global Warming Simulations. *Global Biogeochemical Cycles*, *32*(1), 92–121. doi: 10.1002/2017GB005671

Behrenfeld, M. J., Boss, E., Siegel, D. A., & Shea, D. M. (2005, 3). Carbon-based ocean productivity and phytoplankton physiology from space. *Global Biogeochemical Cycles*, *19*(1). Retrieved from `http://doi.wiley.com/10.1029/2004GB002299` doi: 10.1029/2004GB002299

Behrenfeld, M. J., & Falkowski, P. G. (1997, 1). Photosynthetic rates derived from satellite-based chlorophyll concentration. *Limnology and Oceanography*, *42*(1), 1–20. Retrieved from `http://doi.wiley.com/10.4319/lo.1997.42.1.0001` doi: 10.4319/lo.1997.42.1.0001

Bettencourt, J. H., Lopez, C., Hernandez-Garcia, E., Montes, I., Sudre, J., Dewitte, B., ... Garçon, V. (2015, 12). Boundaries of the Peruvian oxygen minimum zone shaped by coherent mesoscale dynamics. *Nature Geoscience*, *8*(12), 937–940. doi: 10.1038/ngeo2570

Bianchi, D., Dunne, J. P., Sarmiento, J. L., & Galbraith, E. D. (2012). Data-based estimates of suboxia, denitrification, and N2O production in the ocean and their sensitivities to dissolved O2. *Global Biogeochemical Cycles*, *26*(January 2016). doi: 10.1029/2011GB004209

Bianchi, D., McCoy, D., & Yang, S. (2022). Formulation, optimization and sensitivity of nitromzv1.0, a biogeochemical model of the nitrogen cycle in oceanic oxygen minimum zones. *Geoscientific Model Development Discussions*. doi: 10.5194/gmd-2022-244

Bianchi, D., Weber, T. S., Kiko, R., & Deutsch, C. (2018, 4). Global niche of marine anaerobic metabolisms expanded by particle microenvironments. *Nature Geoscience*, *11*(4), 263–268. Retrieved from `http://www.nature.com/articles/s41561-018-0081-0` doi: 10.1038/s41561-018-0081-0

Bourbonnais, A., Letscher, R. T., Bange, H. W., Échevin, V., Larkum, J., Mohn, J., ... Altabet, M. A. (2017, 4). N2O production and consumption from stable isotopic and concentration data in the Peruvian coastal upwelling system. *Global Biogeochemical Cycles*, *31*(4), 678–698. Retrieved from `http://doi.wiley.com/10.1002/2016GB005567` doi: 10.1002/2016GB005567

Brodeau, L., Barnier, B., Treguier, A.-M., Penduff, T., & Gulev, S. (2010, 1). An ERA40-based atmospheric forcing for global ocean circulation models. *Ocean Modelling*, *31*(3-4), 88–104. doi: 10.1016/j.ocemod.2009.10.005

Busecke, J. J., Resplandy, L., & Dunne, J. P. (2019, 6). The Equatorial Undercurrent and the Oxygen Minimum Zone in the Pacific. *Geophysical Research Letters*, *46*(12), 6716–6725. doi: 10.1029/2019GL082692

Busecke, J. J., Resplandy, L., & John, J. G. (2021). Future expansion of the pacific oxygen minimum zone. *Earth and Space Science Open Archive*, 25. Retrieved from `https://doi.org/10.1002/essoar.10507050.1` doi: 10.1002/essoar.10507050.1

Cabré, A., Marinov, I., Bernardello, R., & Bianchi, D. (2015, 9). Oxygen minimum zones in the tropical Pacific across CMIP5 models: Mean state differences and climate change trends. *Biogeosciences*, *12*(18), 5429–5454. doi: 10.5194/bg-12-5429-2015

Canadell, J. G., Scheel Monteiro, P., Costa, M. H., Cotrim da Cunha, L., Cox, P. M., Eliseev, A. V., ... Zickfeld, K. (2021). *Chapter 5: Global Carbon and other Biogeochemical Cycles and Feedbacks. In Climate Change 2021: The Physical Science Basis. Contribution of Working Group I to the Sixth Assessment Report of the Intergovernmental Panel on Climate Change* . Cambridge University Press.

Chavez, F. P., & Messié, M. (2009). A comparison of Eastern Boundary Upwelling Ecosystems. *Progress in Oceanography*, *83*(1-4), 80–96. Retrieved from `http://dx.doi.org/10.1016/j.pocean.2009.07.032` doi: 10.1016/j.pocean.2009.07.032

Codispoti, L. A. (2010). Interesting times for marine N2O. *Science*, *327*(5971), 1339–1340. doi: 10.1126/science.1184945

Cohen, Y., & Gordon, L. I. (1978, 6). Nitrous oxide in the oxygen minimum of the eastern tropical North Pacific: evidence for its consumption during denitrification and possible mechanisms for its production. *Deep Sea Research*, *25*(6), 509–524. doi: 10.1016/0146-6291(78)90640-9

Cornejo, M., & Farías, L. (2012). Following the N2O consumption in the oxygen minimum zone of the eastern South Pacific. *Biogeosciences*, *9*(8), 3205–3212. doi: 10.5194/bg-9-3205-2012

Dalsgaard, T., Stewart, F. J., Thamdrup, B., De Brabandere, L., Revsbech, N. P., Ulloa, O., ... Delong, E. F. (2014). Oxygen at nanomolar levels reversibly suppresses process rates and gene expression in anammox and denitrification in the oxygen minimum zone off Northern Chile. *mBio*, *5*(6), 1–14. doi: 10.1128/mBio.01966-14

Dee, D. P., Uppala, S. M., Simmons, A. J., Berrisford, P., Poli, P., Kobayashi, S., ... Vitart, F. (2011). The ERA-Interim reanalysis: Configuration and performance of the data assimilation system. *Quarterly Journal of the Royal Meteorological Society*, *137*(656), 553–597. doi: 10.1002/qj.828

Deutsch, C., Frenzel, H., McWilliams, J. C., Renault, L., Kessouri, F., Howard, E., ... Yang, S. (2021). Biogeochemical variability in the california current system. *Progress in Oceanography*, *196*, 102565. Retrieved from `https://www.sciencedirect.com/science/article/pii/S0079661121000525` doi: https://doi.org/10.1016/j.pocean.2021.102565

Deutsch, C., Sarmiento, J. L., Sigman, D. M., Gruber, N., & Dunne, J. P. (2007, 1). Spatial coupling of nitrogen inputs and losses in the ocean. *Nature*, *445*(7124), 163–167. doi: 10.1038/nature05392

DeVries, T., Deutsch, C., Rafter, P. A., & Primeau, F. (2013, 4). Marine denitrification rates determined from a global 3-D inverse model. *Biogeosciences*, *10*(4), 2481–2496. doi: 10.5194/bg-10-2481-2013

Dunn, J. (2012, 2). *CSIRO Atlas of Regional Seas (CARS) - 2009.* Tasmanian Partnership for Advanced Computing. Retrieved from `http://dl.tpac.org.au/tpacportal/#dataset=144,https://researchdata.edu.au/csiro-atlas-regional-cars-2009`

Dussin, R., Barnier, B., & Brodeau, L. (2014). The Making of the DRAKKAR FORCING SET DFS5. doi: 10.5281/zenodo.1209243

Duteil, O., Frenger, I., & Getzlaff, J. (2021, 10). The riddle of eastern tropical Pacific Ocean oxygen levels: the role of the supply by intermediate-depth waters. *Ocean Science*, *17*(5), 1489–1507. Retrieved from `https://os.copernicus.org/articles/17/1489/2021/` doi: 10.5194/os-17-1489-2021

Duteil, O., Schwarzkopf, F. U., Böning, C. W., & Oschlies, A. (2014, 3). Major role of the equatorial current system in setting oxygen levels in the eastern tropical Atlantic Ocean: A high-resolution model study. *Geophysical Research Letters*, *41*(6), 2033–2040. Retrieved from `http://doi.wiley.com/10.1002/2013GL058888` doi: 10.1002/2013GL058888

Freing, A., Wallace, D. W., & Bange, H. W. (2012). Global oceanic production of nitrous oxide. *Philosophical Transactions of the Royal Society B: Biological Sciences*, *367*(1593), 1245–1255. doi: 10.1098/rstb.2011.0360

Frischknecht, M., Münnich, M., & Gruber, N. (2017, 1). Local atmospheric forcing driving an unexpected California Current System response during the 2015–2016 El Niño. *Geophysical Research Letters*, *44*(1), 304–311. doi: 10.1002/2016GL071316

Ganesh, S., Parris, D. J., Delong, E. F., & Stewart, F. J. (2014). Metagenomic analysis of size-fractionated picoplankton in a marine oxygen minimum zone. *The ISME Journal*, *8*, 187–211. Retrieved from `www.nature.com/ismej` doi: 10.1038/ismej.2013.144

Garcia, H., Weathers, K., Paver, C., Smolyar, I., Boyer, T., Locarnini, M., ... Reagan, J. (2019a). World Ocean Atlas 2018, Volume 3: Dissolved Oxygen, Apparent Oxygen Utilization, and Dissolved Oxygen Saturation. *NOAA Atlas NESDIS*, *83*.

Garcia, H., Weathers, K., Paver, C., Smolyar, I., Boyer, T., Locarnini, M., ... Reagan, J. (2019b). World ocean atlas 2018, volume 4: Dissolved inorganic nutrients (phosphate, nitrate and nitrate+nitrite, silicate). *NOAA Atlas NESDIS*, *83*.

Garcia, H. E., Boyer, T. P., Locarnini, R. A., Antonov, J. I., Mishonov, A. V., Baranova, O. K., ... Johnson, D. R. (2013). World Ocean Atlas 2013. Volume 3: dissolved oxygen, apparent oxygen utilization, and oxygen saturation. *NOAA Atlas NESDIS 75*, *3*(September), 27.

Garcia, H. E., Locarnini, R., Boyer, T. P., Antonov, J. I., Baranova, O. K., Zweng, M. M., ... Johnson, D. R. (2013). World Ocean Atlas 2013 Volume 4 : Nutrients (phosphate , nitrate , silicate). *NOAA Atlas NESDIS 76*, *4*(September), 396.

Gnanadesikan, A., Bianchi, D., & Pradal, M. A. (2013, 10). Critical role for mesoscale eddy diffusion in supplying oxygen to hypoxic ocean waters. *Geophysical Research Letters*, *40*(19), 5194–5198. doi: 10.1002/GRL.50998

Goreau, T. J., Kaplan, W. A., Wofsy, S. C., McElroy, M. B., Valois, F. W., & Watson, S. W. (1980, 9). Production of NO(2) and N(2)O by Nitrifying Bacteria at Reduced Concentrations of Oxygen. *Applied and environmental microbiology*, *40*(3), 526–32. Retrieved from `http://www.ncbi.nlm.nih.gov/pubmed/16345632http://www.pubmedcentral.nih.gov/articlerender.fcgi?artid=PMC291617` doi: 10.1128/aem.40.3.526-532.1980

IPCC. (2013). *Climate Change 2013: The Physical Science Basis. Contribution of Working Group I to the Fifth Assessment Report of the Intergovernmental Panel on Climate Change*. Cambridge, United Kingdom and New York, NY, USA: Cambridge University Press. Retrieved from `www.climatechange2013.org` doi: 10.1017/CBO9781107415324

Ji, Q., Babbin, A. R., Peng, X., Bowen, J. L., & Ward, B. B. (2015). Nitrogen substrate–dependent nitrous oxide cycling in salt marsh sediments. *Journal of Marine Research*, *73*(3-4), 71–92. doi: 10.1357/002224015815848820

Ji, Q., Buitenhuis, E., Suntharalingam, P., Sarmiento, J. L., & Ward, B. B. (2018). Global Nitrous Oxide Production Determined by Oxygen Sensitivity of Nitrification and Denitrification. *Global Biogeochemical Cycles*, *32*(12), 1790–1802. doi: 10.1029/2018GB005887

Jin, X., & Gruber, N. (2003). Offsetting the radiative benefit of ocean iron fertilization by enhancing N2O emissions. *Geophysical Research Letters*, *30*(24), 1–

4. doi: 10.1029/2003GL018458

Johnson, G. C., Sloyan, B. M., Kessler, W. S., & McTaggart, K. E. (2002). Direct measurements of upper ocean currents and water properties across the tropical Pacific during the 1990s. *Progress in Oceanography*, *52*(1), 31–61. doi: 10.1016/S0079-6611(02)00021-6

Kalvelage, T., Jensen, M. M., Contreras, S., Revsbech, N. P., Lam, P., Günter, M., … Kuypers, M. M. (2011). Oxygen sensitivity of anammox and coupled N-cycle processes in oxygen minimum zones. *PLoS ONE*, *6*(12). doi: 10.1371/journal.pone.0029299

Kalvelage, T., Lavik, G., Lam, P., Contreras, S., Arteaga, L., Löscher, C. R., … Kuypers, M. M. (2013). Nitrogen cycling driven by organic matter export in the South Pacific oxygen minimum zone. *Nature Geoscience*, *6*(3), 228–234. doi: 10.1038/ngeo1739

Karstensen, J., Stramma, L., & Visbeck, M. (2008, 6). Oxygen minimum zones in the eastern tropical Atlantic and Pacific oceans. *Progress in Oceanography*, *77*(4), 331–350. Retrieved from `https://linkinghub.elsevier.com/retrieve/pii/S0079661108000670` doi: 10.1016/j.pocean.2007.05.009

Kessler, W. S. (2006, 5). The circulation of the eastern tropical Pacific: A review. *Progress in Oceanography*, *69*(2-4), 181–217. Retrieved from `https://linkinghub.elsevier.com/retrieve/pii/S0079661106000310` doi: 10.1016/j.pocean.2006.03.009

Key, R., Olsen, A., Van Heuven, S., Lauvset, S., Velo, A., Lin, X., … Suzuki, T. (2015). *Global ocean data analysis project, version 2 (glodapv2), ornl/cdiac-162, nd-p093.* Carbon Dioxide Information Analysis Center (CDIAC). Retrieved from `http://cdiac.ornl.gov/ftp/oceans/GLODAPv2/Data_Products/` doi: 10.3334/CDIAC/OTG.NDP093_GLODAPV2

Kock, A., Arevalo-Martinez, D. L., Loscher, C. R., & Bange, H. W. (2016). Extreme N2O accumulation in the coastal oxygen minimum zone off Peru. *Biogeosciences*, *13*(3), 827–840. doi: 10.5194/bg-13-827-2016

Kock, A., & Bange, H. (2015, 2). Counting the Ocean's Greenhouse Gas Emissions. *Eos*, *96*. doi: 10.1029/2015EO023665

Körner, H., & Zumft, W. G. (1989, 7). Expression of denitrification enzymes in response to the dissolved oxygen level and respiratory substrate in continuous culture of Pseudomonas stutzeri. *Applied and Environmental Microbiology*, *55*(7), 1670–1676. doi: 10.1128/aem.55.7.1670-1676.1989

Krahmann, G., Arévalo-martínez, D. L., Dale, A. W., Dengler, M., Engel, A., Glock, N., … Hansell, D. A. (2021). Climate-Biogeochemistry Interactions in the Tropical Ocean : Data Collection and Legacy. *Frontiers in Marine Science*, *8*(September), 1–23. doi: 10.3389/fmars.2021.723304

Kuypers, M. M., Marchant, H. K., & Kartal, B. (2018). The microbial nitrogen-cycling network. *Nature Reviews Microbiology*, *16*(5), 263–276.

Kwiatkowski, L., Torres, O., Bopp, L., Aumont, O., Chamberlain, M., Christian, J. R., … Ziehn, T. (2020, 7). Twenty-first century ocean warming, acidification, deoxygenation, and upper-ocean nutrient and primary production decline from CMIP6 model projections. *Biogeosciences*, *17*(13), 3439–3470. Retrieved from `https://bg.copernicus.org/articles/17/3439/2020/` doi: 10.5194/bg-17-3439-2020

Kwiecinski, J. V., & Babbin, A. R. (2021, 12). A High-Resolution Atlas of the Eastern Tropical Pacific Oxygen Deficient Zones. *Global Biogeochemical Cycles*, *35*(12). doi: 10.1029/2021GB007001

Lam, P., & Kuypers, M. M. (2011). Microbial Nitrogen Cycling Processes in Oxygen Minimum Zones. *Annual Review of Marine Science*, *3*(1), 317–345. doi: 10.1146/annurev-marine-120709-142814

Large, W. B. (2006). Surface Fluxes for Practitioners of Global Ocean Data Assimilation. In E. P. Chassignet & J. Verron (Eds.), *Ocean weather forecasting:*

An integrated view of oceanography (pp. 229–270). Dordrecht: Springer Netherlands. Retrieved from https://doi.org/10.1007/1-4020-4028-8_9 doi: 10.1007/1-4020-4028-8{_}9

Lauvset, S. K., Key, R. M., Olsen, A., Van Heuven, S., Velo, A., Lin, X., ... Watelet, S. (2016). A new global interior ocean mapped climatology: The 1° × 1° GLODAP version 2. *Earth System Science Data*, *8*(2), 325–340. doi: 10.5194/essd-8-325-2016

Lemarié, F., Kurian, J., Shchepetkin, A. F., Jeroen Molemaker, M., Colas, F., & McWilliams, J. C. (2012). Are there inescapable issues prohibiting the use of terrain-following coordinates in climate models? *Ocean Modelling*, *42*, 57–79. doi: 10.1016/j.ocemod.2011.11.007

Löscher, C. R., Kock, A., Könneke, M., Laroche, J., Bange, H. W., & Schmitz, R. A. (2012). Production of oceanic nitrous oxide by ammonia-oxidizing archaea. *Biogeosciences*, *9*(7), 2419–2429. doi: 10.5194/bg-9-2419-2012

Luyten, J. R., Pedlosky, J., & Stommel, H. (1983, 2). The Ventilated Thermocline. *Journal of Physical Oceanography*, *13*(2), 292–309. doi: 10.1175/1520-0485(1983)013⟨0292:TVT⟩2.0.CO;2

MATLAB. (2020). *Version 9.9.0.1495850 (r2020b) update 1.* Natick, Massachusetts: The MathWorks Inc.

McCoy, D., Damien, P., Clements, D., Yang, S., & Bianchi, D. (2022, November). *Data and source code for "Pathways of Nitrous Oxide Production in the Eastern Tropical South Pacific Oxygen Minimum Zone".* Zenodo. Retrieved from https://doi.org/10.5281/zenodo.7374360 doi: 10.5281/zenodo.7374360

Moore, J. K., Doney, S. C., & Lindsay, K. (2004, 12). Upper ocean ecosystem dynamics and iron cycling in a global three-dimensional model. *Global Biogeochemical Cycles*, *18*(4), n/a-n/a. Retrieved from http://doi.wiley.com/10.1029/2004GB002220 doi: 10.1029/2004GB002220

Nevison, C., Butler, J. H., & Elkins, J. W. (2003, 12). Global distribution of N 2 O and the ΔN 2 O-AOU yield in the subsurface ocean. *Global Biogeochemical Cycles*, *17*(4), n/a-n/a. Retrieved from http://doi.wiley.com/10.1029/2003GB002068 doi: 10.1029/2003GB002068

Olsen, A., Key, R. M., van Heuven, S., Lauvset, S. K., Velo, A., Lin, X., ... Suzuki, T. (2016, 8). The Global Ocean Data Analysis Project version 2 (GLODAPv2) – an internally consistent data product for the world ocean. *Earth System Science Data*, *8*(2), 297–323. doi: 10.5194/essd-8-297-2016

Oschlies, A., Brandt, P., Stramma, L., & Schmidtko, S. (2018). Drivers and mechanisms of ocean deoxygenation. *Nature Geoscience*, *11*(7), 467–473. Retrieved from http://dx.doi.org/10.1038/s41561-018-0152-2 doi: 10.1038/s41561-018-0152-2

Peng, X., Fuchsman, C. A., Jayakumar, A., Warner, M. J., Devol, A. H., & Ward, B. B. (2016). Journal of Geophysical Research : Oceans Revisiting nitrification in the Eastern Tropical South Pacific : A focus on controls. *Journal of Geophysical Research: Oceans*, *121*(3), 1667–1684. doi: 10.1002/2015JC011455.Received

Pennington, J. T., Mahoney, K. L., Kuwahara, V. S., Kolber, D. D., Calienes, R., & Chavez, F. P. (2006, 5). Primary production in the eastern tropical Pacific: A review. *Progress in Oceanography*, *69*(2-4), 285–317. doi: 10.1016/j.pocean.2006.03.012

Ravishankara, A. R., Daniel, J. S., & Portmann, R. W. (2009, 10). Nitrous Oxide (N ¡sub¿2¡/sub¿ O): The Dominant Ozone-Depleting Substance Emitted in the 21st Century. *Science*, *326*(5949), 123–125. doi: 10.1126/science.1176985

Risien, C. M., & Chelton, D. B. (2008). A global climatology of surface wind and wind stress fields from eight years of QuikSCAT scatterometer data. *Journal of Physical Oceanography*, *38*(11), 2379–2413. doi: 10.1175/2008JPO3881.1

Santoro, A. E., Buchwald, C., Knapp, A. N., Berelson, W. M., Capone, D. G., & Casciotti, K. L. (2021, 2). Nitrification and Nitrous Oxide Production in the Offshore Waters of the Eastern Tropical South Pacific. *Global Biogeochemical Cycles*, *35*(2), 1–35. Retrieved from https://onlinelibrary.wiley.com/doi/10.1029/2020GB006716 doi: 10.1029/2020GB006716

Schmidtko, S., Stramma, L., & Visbeck, M. (2017, 2). Decline in global oceanic oxygen content during the past five decades. *Nature*, *542*(7641), 335–339. doi: 10.1038/nature21399

Séférian, R., Berthet, S., Yool, A., Palmieri, J., Bopp, L., Tagliabue, A., ... others (2020). Tracking improvement in simulated marine biogeochemistry between cmip5 and cmip6. *Current Climate Change Reports*, *6*(3), 95–119.

Shchepetkin, A. F. (2015). An adaptive, Courant-number-dependent implicit scheme for vertical advection in oceanic modeling. *Ocean Modelling*, *91*, 38–69.

Shchepetkin, A. F., & McWilliams, J. C. (2005, 1). The regional oceanic modeling system (ROMS): a split-explicit, free-surface, topography-following-coordinate oceanic model. *Ocean Modelling*, *9*(4), 347–404. doi: 10.1016/J.OCEMOD.2004.08.002

Silsbe, G. M., Behrenfeld, M. J., Halsey, K. H., Milligan, A. J., & Westberry, T. K. (2016, 12). The CAFE model: A net production model for global ocean phytoplankton. *Global Biogeochemical Cycles*, *30*(12), 1756–1777. Retrieved from http://doi.wiley.com/10.1002/2016GB005521 doi: 10.1002/2016GB005521

Simmons, A., Uppala, S., Dee, D., & Kobayashi, S. (2006). ERA-Interim: New ECMWF reanalysis products from 1989 onwards. *ECMWF Newsletter No. 110*, 25–35.

Stramma, L., Johnson, G. C., Firing, E., & Schmidtko, S. (2010, 9). Eastern Pacific oxygen minimum zones: Supply paths and multidecadal changes. *Journal of Geophysical Research*, *115*(C9), C09011. Retrieved from http://doi.wiley.com/10.1029/2009JC005976 doi: 10.1029/2009JC005976

Stramma, L., Johnson, G. C., Sprintall, J., & Mohrholz, V. (2008, 5). Expanding Oxygen-Minimum Zones in the Tropical Oceans. *Science*, *320*(5876), 655–658. Retrieved from https://www.science.org/doi/10.1126/science.1153847 doi: 10.1126/science.1153847

Suntharalingam, P., Sarmiento, J. L., & Toggweiler, J. R. (2000). Global significance of nitrous-oxide production and transport from oceanic low-oxygen zones: A modeling study. *Global Biogeochemical Cycles*, *14*(4), 1353–1370. doi: 10.1029/1999GB900100

Thamdrup, B., Dalsgaard, T., & Revsbech, N. P. (2012, 7). Widespread functional anoxia in the oxygen minimum zone of the Eastern South Pacific. *Deep Sea Research Part I: Oceanographic Research Papers*, *65*, 36–45. doi: 10.1016/J.DSR.2012.03.001

Tian, H., Xu, R., Canadell, J. G., Thompson, R. L., Winiwarter, W., Suntharalingam, P., ... Yao, Y. (2020). A comprehensive quantification of global nitrous oxide sources and sinks. *Nature*, *586*(October). Retrieved from http://dx.doi.org/10.1038/s41586-020-2780-0 doi: 10.1038/s41586-020-2780-0

Walter, S., Bange, H. W., Breitenbach, U., & Wallace, D. W. R. (2006). *Nitrous oxide in the north atlantic ocean* (Vol. 3; Tech. Rep. No. 4). Retrieved from https://bg.copernicus.org/articles/3/607/2006/ doi: 10.5194/bg-3-607-2006

Wanninkhof, R. (1992). Relationship between wind speed and gas exchange over the ocean. *Journal of Geophysical Research*, *97*(C5), 7373–7382. doi: 10.1029/92JC00188

Yang, S., Chang, B. X., Warner, M. J., Weber, T. S., Bourbonnais, A. M., Santoro, A. E., ... Bianchi, D. (2020). Global reconstruction reduces the uncertainty of oceanic nitrous oxide emissions and reveals a vigorous seasonal cycle. *Pro-*

ceedings of the National Academy of Sciences of the United States of America, *117*(22). doi: 10.1073/pnas.1921914117

Yang, S., Gruber, N., Long, M. C., & Vogt, M. (2017, 10). ENSO-Driven Variability of Denitrification and Suboxia in the Eastern Tropical Pacific Ocean. *Global Biogeochemical Cycles*, *31*(10), 1470–1487. doi: 10.1002/2016GB005596

Yoshida, N., Morimoto, H., Hirano, M., Koike, I., Matsuo, S., Wada, E., ... Hattori, A. (1989, 12). Nitrification rates and 15N abundances of N2O and NO3 in the western North Pacific. *Nature*, *342*(6252), 895–897. doi: 10.1038/342895a0

Pathways of Nitrous Oxide Production in the Eastern Tropical South Pacific Oxygen Minimum Zone

Daniel McCoy[1], Pierre Damien[1], Daniel Clements[1], Simon Yang[1], Daniele Bianchi[1]

[1]Department of Atmospheric and Oceanic Sciences
[1]University of California – Los Angeles
[1]520 Portola Plaza, Los Angeles, CA 90095, USA

Key Points:

- In the eastern tropical South Pacific Oxygen Minimum Zone, denitrification is the dominant source of N_2O production.
- Tropical subsurface currents supply N_2O to the region, fueling N_2O emissions to the atmosphere.
- Significant amounts of locally-produced N_2O escape outgassing and are exported to the subtropical gyre.

Corresponding author: Daniel McCoy, `demccoy@atmos.ucla.edu`

Abstract

Oceanic emissions of nitrous oxide (N_2O) account for roughly one-third of all natural sources to the atmosphere. Hot-spots of N_2O outgassing occur over oxygen minimum zones (OMZs), where the presence of steep oxygen gradients surrounding anoxic waters leads to enhanced N_2O production from both nitrification and denitrification. However, the relative contributions from these pathways to N_2O production and outgassing in these regions remains poorly constrained, in part due to shared intermediary nitrogen tracers, and the tight coupling of denitrification sources and sinks. To shed light on this problem, we embed a new, mechanistic model of the OMZ nitrogen cycle within a three-dimensional eddy-resolving physical-biogeochemical model of the ETSP, tracking contributions from remote advection, atmospheric exchange, and local nitrification and denitrification. Our results indicate that net N_2O production from denitrification is approximately one order of magnitude greater than nitrification within the ETSP OMZ. However, only ∼30% of denitrification-derived N_2O production ultimately outgasses to the atmosphere in this region (contributing ∼34% of the air-sea N_2O flux on an annual basis), while the remaining is exported out of the domain. Instead, remotely-produced N_2O advected into the OMZ region accounts for roughly half (∼56%) of the total N_2O outgassing, with smaller contributions from nitrification (∼7%). Our results suggests that, together with enhanced production by denitrification, upwelling of remotely-derived N_2O (likely produced via nitrification in the oxygenated ocean) contributes the most to N_2O outgassing over the ETSP OMZ.

1 Introduction

Nitrous oxide (N_2O) is a powerful greenhouse gas that is roughly 300 times more potent than carbon dioxide (CO_2) and is projected to become the most important ozone-depleting anthropogenic emission by the end of the 21st century (Ravishankara et al., 2009; IPCC, 2013). Recent analyses of the global N_2O budget over the decade of 2007 - 2016 suggest that anthropogenic emissions are responsible for up to 40% of total N_2O sources to the atmosphere, mostly from agriculture, whereas outgassing from the ocean accounts for roughly 20% (Canadell et al., 2021). The production of N_2O in the ocean is linked to the remineralization of organic matter (OM) via both aerobic and anaerobic pathways, and, as a consequence, is tightly coupled to the oceanic oxygen (O_2) distribution (Freing et al., 2012; Arévalo-Martínez et al., 2015; Babbin et al., 2015; Ji et al., 2015; Yang et al., 2020). While in large parts of the surface ocean N_2O concentrations are close to saturation, the most intense hot-spots of N_2O air-sea flux are found in the Eastern Tropical North Pacific (ETNP), the Eastern Tropical South Pacific (ETSP), and the Arabian Sea, where high organic matter export rates and sluggish lateral circulation results in steep O_2 gradients that surround anoxic (here defined as $O_2 < 5\ mmol\ m^{-3}$) waters also known as oxygen minimum zones (OMZ)(Codispoti, 2010; Arévalo-Martínez et al., 2015; Ji et al., 2018; Yang et al., 2020). Although OMZ regions only account for roughly 1% of the total ocean volume, the dynamic marine nitrogen cycling that occurs there results in up to 50% of total oceanic N_2O emissions (Codispoti, 2010; Arévalo-Martínez et al., 2015; Babbin et al., 2015; Yang et al., 2020).

The ETSP hosts the second largest OMZ by area and comprises the Humboldt Current System, one of the four major Eastern Boundary Upwelling Systems, which extends from the southern extent of Chile ($\sim 45^oS$) to northern Peru ($\sim 4^oS$)(Chavez & Messié, 2009; Santoro et al., 2021). While southern Chile experiences more intense upwelling during boreal summer (Pennington et al., 2006), upwelling-favorable conditions exist year-round along the Peruvian and northern Chile coastlines, fueling high rates of surface primary productivity, organic matter export (Chavez & Messié, 2009), and subsurface O_2 depletion. The ETSP OMZ is located in the South Pacific tropical shadow zone of the thermocline (Luyten et al., 1983), which extends westward from the eastern boundary between the equatorward edges of the subtropical gyres. This limits the supply of oxy-

gen from the ventilated subtropical gyres to the OMZs, and leaves the relatively O_2-rich eastward tropical currents such as the Equatorial Undercurrent (EUC) and the Southern Subsurface Countercurrents (SSCC) as the major advective sources of O_2 to the equatorward side of the ETSP OMZ (Karstensen et al., 2008; Stramma et al., 2010). While these advective pathways are reinforced by lateral O_2 supply from mesoscale eddies (Gnanadesikan et al., 2013; Bettencourt et al., 2015), O_2 remains depleted within the OMZ core (Kwiecinski & Babbin, 2021), leading to functional anoxia (Thamdrup et al., 2012), fixed nitrogen loss, a pronounced subsurface nitrite (NO_2^-) maximum, and a strong nitrogen deficit (Kalvelage et al., 2013). An additional characteristic of the ETSP is the relatively sharp transition from anoxic to suboxic ($5\ mmol\ m^{-3} < O_2 < 10\ mmol\ m^{-3}$) waters along the OMZ boundary. These O_2 gradients host both aerobic (i.e., nitrification) and anaerobic (i.e., denitrification) nitrogen cycle transformations, ultimately leading to N_2O supersaturation in the layers surrounding the anoxic core (Babbin et al., 2015; Kock et al., 2016). Upwelling of these waters to the surface likely contributes to the local hot-spot of N_2O outgassing in the ETSP, as shown by observational and modeling studies (Arévalo-Martínez et al., 2015; Ji et al., 2018; Yang et al., 2020).

Nitrification is a two-step process that occurs within the oxygenated water column wherein ammonium (NH_4^+) produced from remineralization of organic matter (pathway 1 in Figure 1) is oxidized by O_2 to NO_2^- and subsequently to nitrate (NO_3^-) by NH_4^+-oxidizing bacteria and archaea and NO_2^--oxidizing bacteria, respectively (pathways 2 and 4, respectively) (Lam & Kuypers, 2011). Nitrification-derived N_2O occurs as a byproduct of NH_4^+ oxidation (pathway 3), resulting in a positive correlation between apparent oxygen utilization (AOU) and supersaturated N_2O concentrations in many areas of the ocean (Cohen & Gordon, 1978; Walter et al., 2006), a process that has been further quantified by active production of $^{15}N_2O$ in ^{15}N tracer incubation experiments (Yoshida et al., 1989). The ratio of N_2O yield to NO_2^- yield from NH_4^+ oxidation has been observed to increase at decreasing O_2 concentrations in cultures with NH_4^+-oxidizing bacteria and archaea (Goreau et al., 1980; Löscher et al., 2012), likely leading to enhanced nitrification-derived N_2O production within the steep suboxic gradients above and below the anoxic core of OMZs (Nevison et al., 2003; Ji et al., 2015, 2018; Santoro et al., 2021).

Besides N_2O production via the nitrification pathway, N_2O also forms as an intermediary product of step-wise denitrification (NO_3^- to NO_2^- to N_2O to N_2) under suboxic and anoxic conditions (pathways 5 - 7 in Figure 1). Within the anoxic core of OMZs, widespread consumption of N_2O occurs via N_2O reduction — the only known process able to remove N_2O from the water column. However, recent studies have highlighted how the different steps, each mediated by distinct enzymes and likely different microorganisms (Ganesh et al., 2014; Kuypers et al., 2018), are subject to variable O_2 sensitivities wherein NO_3^-, NO_2^-, and N_2O reduction become progressively less O_2 tolerant (Körner & Zumft, 1989; Kalvelage et al., 2011; Dalsgaard et al., 2014; Babbin et al., 2015; Ji et al., 2015). Therefore, the same suboxic gradients that lead to enhanced N_2O production from nitrification can also lead to N_2O accumulation from denitrification, as NO_2^- reduction proceeds while N_2O reduction is inhibited, in a process referred to as "incomplete" denitrification (Babbin et al., 2015).

The coupled production of N_2O at low O_2 from nitrification and denitrification, and their shared NO_2^- intermediary, complicate the interpretation of in situ observations from OMZs (Ji et al., 2015, 2018; Santoro et al., 2021). Observations of N_2O and NO_2^- in these regions typically reveal an OMZ anoxic core layer characterized by a secondary NO_2^- maximum and undersaturated N_2O concentrations, suggesting coupled step-wise denitrification. Supersaturated concentrations of N_2O in the bounding suboxic gradients (the upper and lower oxyclines) have been linked to the enhanced production by nitrification (Cohen & Gordon, 1978). Yet, studies have noted the lack of a linear relationship with AOU and high abundances of gene markers for NO_2^- reduction as evidence

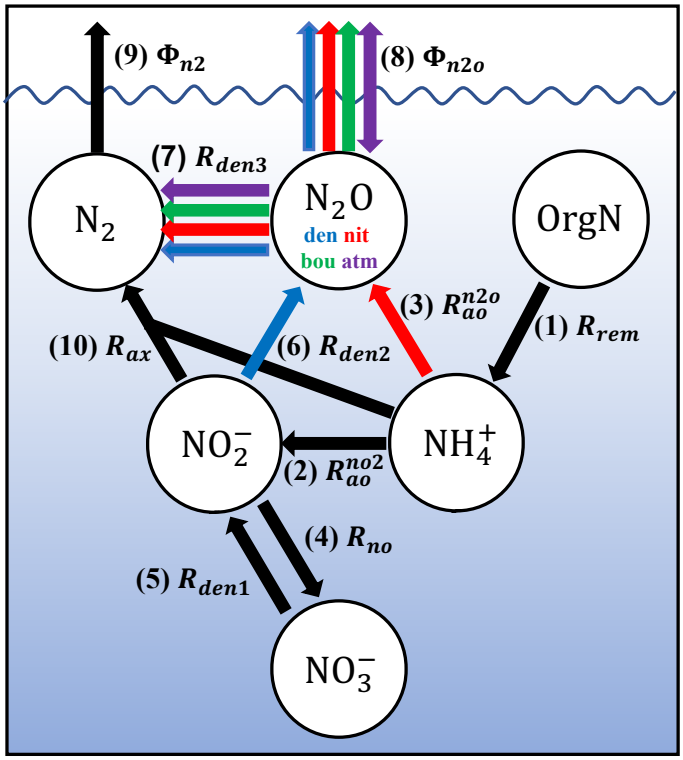

Figure 1. Schematic of the oceanic nitrogen cycle (ignoring biological uptake) as represented in ROMS. Transformation pathways include: (1, R_{rem}) oxic remineralization of nitrogen in organic matter (OrgN) to ammonium; (2, R_{ao}^{no}) ammonium oxidation to nitrite; (3, R_{ao}^{n2o}) ammonium oxidation to nitrous oxide; (4, R_{no}) nitrite oxidation; (5, R_{den1}) nitrate reduction; (6, R_{den2}) nitrite reduction; (7, R_{den3}) decomposed nitrous oxide reduction; (8, Φ_{n2o}) decomposed nitrous oxide air-sea flux; (9, Φ_{n2}) dinitrogen air-sea flux; and (10, R_{ax}) anaerobic ammonium oxidation (anammox). Colored arrows correspond to the sources and sinks of the decomposed N_2O tracers (N_2O_{den}, N_2O_{nit}, N_2O_{bou}, and N_2O_{atm}) discussed in Section 2.4.

of simultaneous production from both nitrification and incomplete denitrification (Arévalo-Martínez et al., 2015), as further supported by isotopic evidence (Bourbonnais et al., 2017).

However, while progressive O_2 tolerances for denitrification have been documented (Dalsgaard et al., 2014), biogeochemical models predominantly employ simple parameterizations representing N_2O production as a function of nitrification, whereas denitrification is typically modelled with a lack of N_2O production or as a net sink of N_2O at low O_2 (Suntharalingam et al., 2000; Jin & Gruber, 2003; Ji et al., 2018; Battaglia & Joos, 2018). Other studies have highlighted the importance of resolving O_2-dependent decoupling of N_2O production and consumption (Babbin et al., 2015), suggesting that N_2O production rates from denitrification may be up to two orders of magnitude larger than those from nitrification near the core of OMZs, albeit closely balanced by N_2O reduction to dinitrogen gas (N_2). Thus, incomplete denitrification may account for a production source that is poorly represented in most biogeochemical ocean and climate models.

While the uncertainty surrounding N_2O production in the ocean has been reduced in recent years following improved estimates of ocean (Yang et al., 2020), terrestrial, and anthropogenic N_2O sources (Canadell et al., 2021; Tian et al., 2020), barriers remain in

accurately projecting future air-sea flux because of poorly constrained contributions from the nitrification and denitrification pathways. The observed expansion of OMZs (Stramma et al., 2008; Schmidtko et al., 2017; Oschlies et al., 2018) is expected to continue over the 21st century, although the extent of future changes in low O_2 and anoxic water volumes remain uncertain (Cabré et al., 2015; Bianchi et al., 2018; Busecke et al., 2021). Therefore, accurate parameterization of N_2O cycling in global ocean models is crucial in simulating realistic future scenarios, and a better understanding of the physical and biogeochemical mechanisms and relative contributions from both production pathways is warranted. This is particularly critical given that OMZ regions continue to be poorly resolved in current global Earth system models (Cabré et al., 2015; Busecke et al., 2021; Séférian et al., 2020), which generally struggle to capture the role of fine-scale circulation such as the zonal jet systems that ventilate the tropical Ocean (Kessler, 2006; Duteil et al., 2014; Busecke et al., 2019; Duteil et al., 2021).

To address these sources of uncertainty, we implement a new model of the OMZ nitrogen cycle (NitrOMZ) (Bianchi et al., 2022) into an eddy-resolving three-dimensional (3-D) regional ocean model of the ETSP that simulates local N_2O production from nitrification and denitrification. The new model, constrained by in situ ETSP observations of nitrogen cycle tracers and rates, allows for an examination of the N_2O balance within a characteristic OMZ upwelling region. To attribute the sources of N_2O outgassing flux to different processes, we use the 3-D model to track contributions from local air-sea gas exchange, advection into the domain from the boundaries, and production by nitrification and denitrification. This analysis reveals the importance of incomplete denitrification and transport of remotely-generated N_2O for air-sea fluxes, with implications for future N_2O emissions in a changing ocean.

The rest of the paper is organized as follows: Section 2 describes the 3-D model configuration and setup, a brief summary of N_2O production pathways in NitrOMZ, and the N_2O tracer decomposition strategy; Section 3 provides a short validation of model solutions, summarizes the results of the simulations, and describes the ETSP N_2O balance; Section 4 discusses the results and implications, and concludes the paper.

2 Modelling Methods and Validation

2.1 Physical Model Configuration and Forcing

The physical component of the model consists of the Regional Ocean Modeling System (ROMS) (Shchepetkin & McWilliams, 2005; Shchepetkin, 2015), a primitive-equation, hydrostatic, topography-following general ocean circulation model. The model domain extends from -111.38^oW to -66.62^oW and from 42.52^oS to 3.41^oN and is chosen to resolve key oceanographic features of the ETSP such as the EUC (Figure 2c), the wind-driven South Pacific gyre (contour lines in Figure 2a and 2b), and the horizontal extent of the OMZ (Figure 3a). Its grid consists of 402 x 502 points with a nominal resolution of 10 kilometers and 42 topography-following vertical levels with higher resolution at the surface and bottom. The model time-step is 800 seconds, and output is saved as monthly means.

For this study, low-frequency interannual variability is ignored to instead focus on a climatological steady-state. Initial conditions and monthly climatological boundary forcing (applied at the northern, western, and southern boundaries) for temperature, salinity, surface elevation, and horizontal velocity are taken from an existing Pacific-wide ROMS simulation (Lemarié et al., 2012). Normal-year-forcing of daily freshwater and turbulent heat fluxes are estimated using bulk formulae (Large, 2006) applied to ERA-interim (ERAi) reanalysis data for the year 1979 (Simmons et al., 2006; Dee et al., 2011). Because of known biases in ERAi shortwave (overestimate) and longwave (underestimate) fluxes (Brodeau et al., 2010), we applied the DRAKKAR Forcing Set version 5.2 corrections to heat flux

terms (Dussin et al., 2014). Daily climatological wind stress is taken from the QuickSCAT-based Scatterometer Climatology of Ocean Winds (Risien & Chelton, 2008). The resulting simulation produces an overall similar climatological picture of the hydrographic properties, gyre circulation, and equatorial current structure of the ETSP (Figure 2a - c) when compared to validation products (Figure 2d - f).

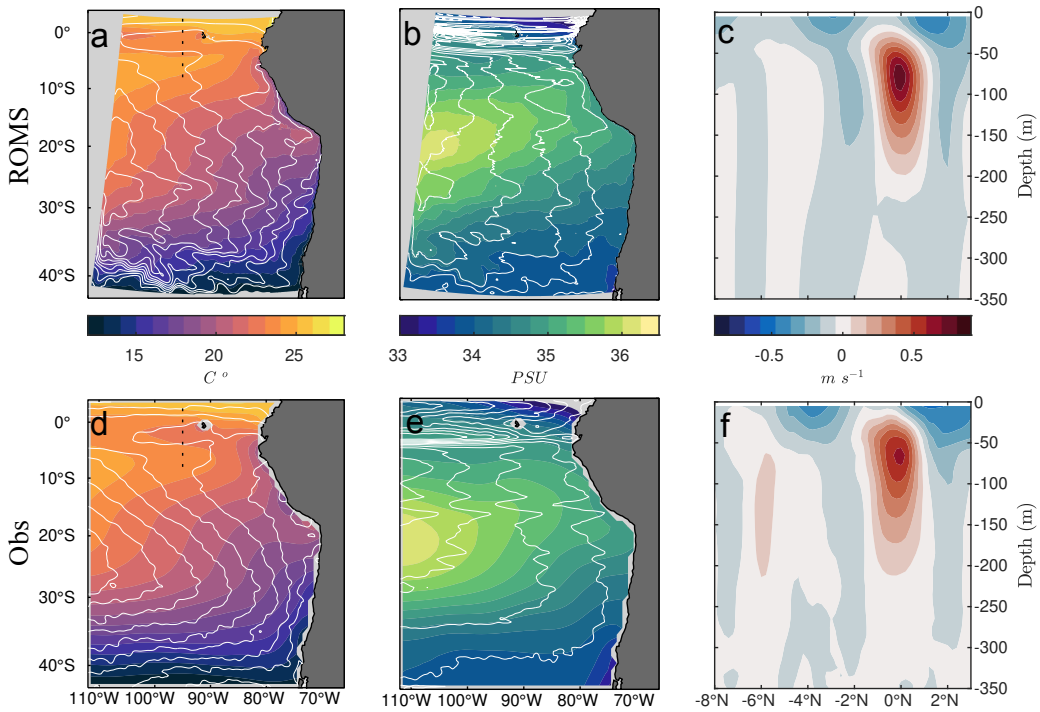

Figure 2. (a,d) Annually averaged sea-surface temperature from ROMS model years 46 - 50 (top) and World Ocean Atlas 2018 (bottom). Contours highlight sea-surface height at 5 *cm* intervals, with validation data obtained by averaging AVISO data between 2000 to 2018. Dashed lines mark the transect location in panels (c) and (f). (b,e) Same as in panels (a) and (d), but for sea-surface salinity; contours highlight calculated geostrophic velocity streamlines, with validation data derived from AVISO. (c,f) Zonal velocity sections along the equator at 95^oW from ROMS (top) and Johnson et al. (2002) (bottom).

2.2 Biogeochemical Model Configuration and Forcing

The physical model is coupled online to the Biogeochemical Elemental Cycling (BEC) model from Moore et al. (2004) using the same equations and parameter settings as in Frischknecht et al. (2017) with the exception of the nitrogen cycling component, which was expanded for the NitrOMZ model (Bianchi et al., 2022). NitrOMZ explicitly resolves the main set of nitrogen cycle transformations associated with the remineralization of sinking OM in low O_2 environments (summarized in Figure 1). These include the chemolithotrophic reactions associated with nitrification: aerobic NH_4^+ oxidation to both N_2O ($R_{ao}^{n_2o}$) and NO_2^- ($R_{ao}^{no_2}$), and aerobic NO_2^- oxidation to NO_3^- (R_{no}). Anaerobic NH_4^+ oxidation with NO_2^- to N_2 (anammox, R_{ax}) is also represented. Additionally, NitrOMZ partitions the OM remineralization cycle in ROMS-BEC to include three additional heterotrophic denitrification steps: NO_3^- reduction to NO_2^- (R_{den1}), NO_2^- reduction to N_2O (R_{den2}), and N_2O reduction to N_2 (R_{den3}). The treatment of OM in the model is outlined in support-

ing information S1, with chemolithotrophic and heterotrophic reactions summarized in S2. Notably, the model expands BEC by allowing for the production of N_2O via both nitrification and incomplete denitrification pathways (Section 2.2.1).

Initial conditions and boundary forcing of biogeochemical nutrient concentrations (NO_3^-, PO_4^{3-}, $Si(OH)_4$ and O_2) are taken from monthly climatological observations from the 2013 World Ocean Atlas (H. E. Garcia, Boyer, et al., 2013; H. E. Garcia, Locarnini, et al., 2013); NH_4^+, NO_2^-, and N_2 boundary conditions are set to 0 but adjust rapidly within the domain. Iron data were taken from the Community Earth System Model (CESM) as in Deutsch et al. (2021), and DIC/Alkalinity were extracted from GLODAP (Lauvset et al., 2016) with a reference year of 2002. Initial and monthly boundary conditions for N_2O were provided from a 3-D reconstruction based on in situ data from recent cruises to the ETSP (Kalvelage et al., 2013; Ji et al., 2015; Peng et al., 2016; Babbin et al., 2017, 2020), and the MEMENTO databases (Kock & Bange, 2015) and GLODAP (Olsen et al., 2016; Lauvset et al., 2016), which we extrapolate to the model domain using the same machine learning approach as described in Yang et al. (2020).

2.2.1 NitrOMZ N_2O Production

Production of N_2O via nitrification in NitrOMZ is modelled as a by-product of NH_4^+ oxidation ($R_{ao}^{n_2o}$, pathway 3 in Figure 1), with enhanced yields at lower O_2 concentrations. Both nitrification steps (i.e. NO_2^- oxidation) are suppressed near the surface by light inhibition (see supporting information S4) and competition for NH_4^+ and NO_2^- from phytoplankton as in Frischknecht et al. (2017). Therefore, nitrification is largely restricted to below the euphotic zone while also being suppressed at low O_2. The partitioning between N_2O and NO_2^- production from R_{ao} is calculated using the function proposed by Nevison et al. (2003), derived by fitting measured N_2O and NO_2^- yields ($f_{ao}^{n_2o}$ and $f_{ao}^{no_2}$, respectively) to oxygen concentrations (Goreau et al., 1980):

$$\frac{f_{ao}^{n_2o}}{f_{ao}^{no_2}} = 0.01 \cdot \frac{a}{[O_2]} + b. \tag{1}$$

Relative to the original parameterization by Nevison et al. (2003), we apply distinct values of the parameters a and b to reflect results from a series of in situ measurements of N_2O production from the ETSP and ETNP OMZs (Ji et al., 2015, 2018; Santoro et al., 2021) (see Section 2.3.1). N_2O production by nitrification, in units of *mmol* N m^{-3} s^{-1}, is therefore represented as:

$$R_{ao}^{n_2o} = R_{ao} \cdot f_{ao}^{n_2o}, \tag{2}$$

with a similar function for NO_2^- production.

In the denitrification pathway, N_2O is produced via NO_2^- reduction at low O_2:

$$R_{den2}^{n_2o} = f_{den2} \cdot R_{rem}^{tot} \cdot Q_{den}^{C:N}, \tag{3}$$

where f_{den2} is the local fraction of total OM remineralization (R_{rem}^{tot}) routed to NO_2^- reduction (see supporting information S2), and $Q_{den}^{C:N}$ the carbon to nitrogen ratio from denitrification (472/2/106) following Anderson and Sarmiento (1994). Similarly, N_2O is consumed via N_2O reduction to N_2 at low O_2:

$$R_{den3}^{n_2} = f_{den3} \cdot R_{rem}^{tot} \cdot Q_{den}^{C:N}. \tag{4}$$

Net production of N_2O ($R_{net}^{n_2o}$, in units of *mmol* N_2O m^{-3} s^{-1}) results by the combination of nitrification (equation (2)) and the residual between NO_2^- and N_2O reduction (equation (3) minus equation (4)):

$$R_{net}^{n_2o} = 0.5 \cdot (R_{ao}^{n_2o} + R_{den2}^{n_2o}) - R_{den3}^{n_2}. \tag{5}$$

2.3 Biogeochemical Validation

To validate the biogeochemical tracer distributions simulated by ROMS-BEC, we gathered O_2, NO_3^-, PO_4^{-3}, and N^* (defined as 16·[NO_3^-] - [PO_4^{3-}]) reconstructions from World Ocean Atlas 2018 (H. Garcia et al., 2019a) (Figures S1 - S4); additional O_2 estimates were provided by Dunn (2012) and Bianchi et al. (2012). Estimates of 3-D NO_2^- and N_2O were obtained from in situ observations (Kock & Bange, 2015; Lauvset et al., 2016), and extrapolated using a machine learning approach as outlined in Yang et al. (2020) (Figures S5 - S6). Annually averaged maps of net primary production (NPP) were obtained using three different productivity algorithms, which included the Eppley Vertically Generalized Production Model (Eppley-VGPM) (Behrenfeld & Falkowski, 1997), the updated Carbon-Based Productivity Model (CbPM2) (Behrenfeld et al., 2005) and the Carbon, Absorption, and Fluorescence Euphotic-resolving model (CAFE) (Silsbe et al., 2016) (Figure S7). Level 3 satellite chlorophyll-a concentration data were obtained from the NASA Ocean Color data center (Figure S8), with all of the satellite-based data (including NPP) obtained from the Ocean Productivity Group at Oregon State University. Additional model validation is discussed in Section 3.1.

2.3.1 Model Parameterization and Spinup

Further details on the formulation and parameterization of NitrOMZ are discussed in Bianchi et al. (2022). Briefly, we estimated uncertain model parameters by optimizing a one-dimensional version of the model against a cost functioned designed to evaluate squared errors between model estimates and local observations of tracers and N transformation rates from the ETSP (Kalvelage et al., 2013; Ji et al., 2015; Peng et al., 2016; Babbin et al., 2017, 2020). Based on the optimization, we implement a low-cost parameter set with good comparisons to observed N_2O and NO_2^- profiles (Opt_{sel} from Bianchi et al. (2022), with parameter values in Table S4) into ROMS-BEC. The model is initially run for 20 years before evaluating against the validation products discussed in Section 2.3 and in situ ETSP observations from Kalvelage et al. (2013), Cornejo and Farías (2012), and Krahmann et al. (2021).

Based on this first comparison, we applied additional tuning to (1) bring surface concentrations of NO_2^- and NH_4^+ closer to zero and (2) increase the concentration of N_2O in suboxic waters to better match the magnitude of observed subsurface N_2O maxima in the ETSP OMZ. This was accomplished by (1) slightly increasing the maximum NH_4^+ and NO_2^- oxidation rates (k_{ao} and k_{no}, respectively, see supporting information S2) and (2) slightly widening the difference between exponential O_2 inhibition thresholds for NO_2^- and N_2O reduction ($K_{den2}^{o_2}$ and $K_{den3}^{o_2}$, respectively). We implement the final parameter set into ROMS-BEC and run a 50 year-long simulation to obtain a steady-state solution (Figure S9).

The choice of parameters results in a high NH_4^+ oxidation rate (R_{ao}) just below the euphotic zone that mostly produces NO_2^- ($R_{ao}^{no_2}$) due to high O_2 concentrations. As O_2 becomes scarce, R_{ao} decreases, yet production of N_2O ($R_{ao}^{n_2o}$) relative to NO_2^- increases following equations (1) and (2). Consumption of N_2O within anoxic waters occurs as all denitrification steps proceed without O_2 inhibition (consumption >> production). Similar to Babbin et al. (2015) and Bianchi et al. (2022), we model a progressive O_2 inhibition of the three denitrification steps ($K_{den1}^{O_2} > K_{den2}^{O_2} > K_{den3}^{O_2}$). Therefore, incomplete denitrification is allowed to occur at low but non-zero O_2 as NO_3^- reduction and NO_2^- reduction (R_{den1} and R_{den2}, respectively) proceed while N_2O reduction (R_{den3}) is inhibited (consumption < production).

2.4 N_2O Balance and Tracer Decomposition

To track the evolution of N_2O from different pathways, we decompose N_2O into four tracers that keep track of N_2O sources in the model domain:

$$N_2O = N_2O_{den} + N_2O_{nit} + N_2O_{atm} + N_2O_{bou}. \tag{6}$$

Each of the tracers in equation (6) follows a separate conservation equation (see supporting information S3), and is affected by a specific production process, by air-sea gas fluxes, transport from the boundaries, and destruction by the last step of denitrification (N_2O reduction, R_{den3}). By construction, the conservation equations for the individual tracers sum up to the conservation equation for N_2O (equation (5)), so that equation (6) can be considered a linear tracer decomposition.

Specifically, N_2O_{nit} tracks local production by nitrification (R_{ao}^{n2o}, equation (2)) whereas N_2O_{den} tracks production by denitrification ($R_{den2}^{n_2o}$, equation (3)) as outlined in Section 2.2.1 (pathways 3 and 6, respectively, in Figure 1). The remaining tracers, N_2O_{atm} and N_2O_{bou}, are designed to track N_2O originating from the atmosphere and from production sources outside the regional ROMS domain, respectively. Saturated N_2O forced from the model boundaries (assuming an atmospheric N_2O concentration of 300 ppb) can be interpreted as originating from air-sea equilibrium with the atmosphere, whereas supersaturated N_2O is linked to production outside the regional model domain. We therefore split the N_2O forced into the domain into a saturation component (N_2O_{atm}) and a supersaturation component (N_2O_{bou}) transported into the domain.

To close separate biogeochemical budgets for each N_2O tracer, we similarly decomposed the N_2O reduction rate (R_{den3}, equation (4) and pathway 7 in Figure 1) and N_2O air-sea flux (Φ^{n2o}, pathway 8 in Figure 1) to track losses with respect to the decomposed N_2O concentrations from within the domain:

$$R_{den3} = R_{den3}^{den} + R_{den3}^{nit} + R_{den3}^{bou} + R_{den3}^{atm} \tag{7}$$

$$\Phi_{n2o} = \Phi_{n2o}^{den} + \Phi_{n2o}^{nit} + \Phi_{n2o}^{bou} + \Phi_{n2o}^{atm}. \tag{8}$$

Here, each consumption term by denitrification is proportional to the individual tracer concentration in a linear fashion. Air-sea fluxes follow the same formulation as N_2O (modeled according to Wanninkhof (1992) using a constant atmospheric mixing ratio of 300 ppb), but with mixing ratios set to zero for all tracers except N_2O_{atm}, for which it is set to the total value. Therefore, while initially saturated at the boundaries, the concentration of N_2O_{atm} can drop below saturation following consumption via R_{den3}^{atm}. When N_2O-undersaturated water is exposed to the surface, atmospheric in-gassing will increase N_2O_{atm} until N_2O reaches saturation. As such, N_2O_{atm} tracks both domain ingassing of N_2O and import of saturated N_2O from the model boundaries, whereas N_2O_{bou} exclusively tracks import of the supersaturation component. To initialize the decomposition, the initial 3-D N_2O was separated into N_2O_{atm} and N_2O_{bou} while N_2O_{nit} and N_2O_{den} were set to zero everywhere; thus these tracers exclusively track production within the domain after initialization (Figure S10).

Finally, to elucidate the sources of N_2O air-sea flux over the OMZ, we defined a budget domain that captures the extent of the ETSP OMZ horizontally (dashed blue box in Figure 3a) and vertically from the surface to 750 m depth. We configured ROMS output to close biogeochemical budgets within each grid cell, allowing us to scale them up to arbitrary 3-D domains within the model:

$$\frac{d[\mathrm{C}]}{dt} = J + T - \Phi. \tag{9}$$

Here, $d[\mathrm{C}]/dt$ is the climatological N_2O rate of change calculated as the difference between snapshots at the beginning and end of each month; T the transport component calculated as the divergence of advection/diffusion fluxes, J the sum of biological sources and sinks, and Φ the air-sea flux controlled by gas exchange.

3 Results

3.1 Model Validation

Figure 3 shows the extent and thickness of the modelled OMZ from model years 46 - 50 (Figure 3a) and various validation products (Figure 3b - e). The simulated OMZ is centered offshore of the Peruvian and Ecuadorian coastline at roughly 8^oS and extends from the Galapagos islands at the equator to nearly 15^oS. This represents a displacement both equatorward and offshore compared to observations, which suggest a more coastal OMZ between southern Peru and Chile. The thickness of waters with less than 10 $mmol$ O_2 m^{-3} ranges mostly between 300 - 500 m and extends to roughly 105^oW. Considering that O_2 reconstructions based on spatial interpolation of in situ profiles underestimate the volume of anoxic waters (Bianchi et al., 2012), the inset bar plot in Figure 3a suggests that the ROMS simulation is overall within range of OMZ volume predictions across several thresholds ranging from 5 $mmol$ O_2 m^{-3} (Kwiecinski & Babbin, 2021) to 20 $mmol$ O_2 m^{-3} (H. Garcia et al., 2019a; Bianchi et al., 2012; Dunn, 2012).

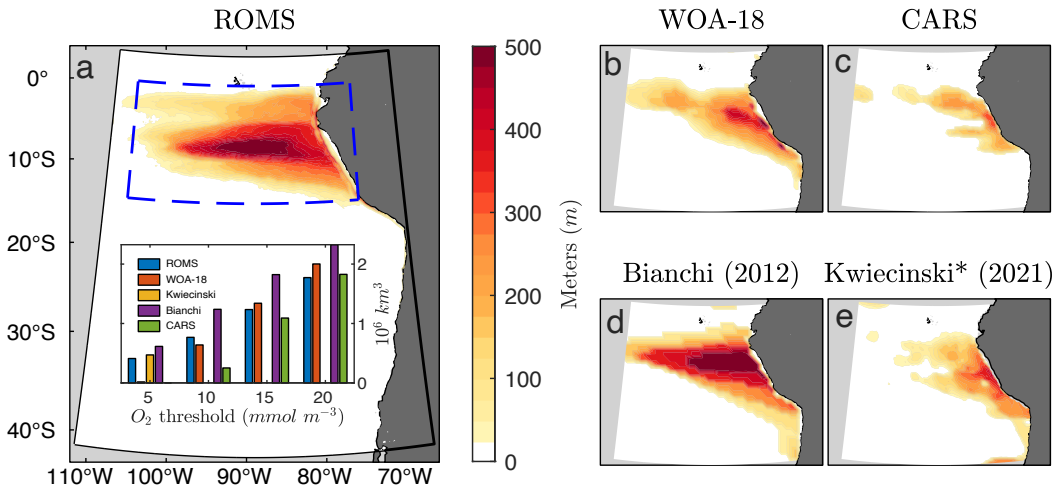

Figure 3. (a) ROMS Peru-Chile 10 km domain, with annually averaged OMZ thickness (O_2 < 10 $mmol$ m^{-3}) from model years 46 - 50. The inset bar plot shows OMZ volume from ROMS and validation products based on 5, 10, 15, and 20 $mmol$ m^{-3} thresholds. The N_2O budget region is also shown as the area encompassed by dashed blue lines, extending vertically from the surface to 750 m. (b-d) OMZ thickness (O_2 < 10 $mmol$ m^{-3}) from World Ocean Atlas 2018, CSIRO Atlas of Regional Seas (CARS), and the Objective mapping 2 product from Bianchi et al. (2012). (e) OMZ thickness (O_2 < 5 $mmol$ m^{-3}) from Kwiecinski and Babbin (2021).

Taking into account the slight equatorward geographic shift in the model OMZ, nitrogen tracer (NO_3^-, NO_2^-, and N_2O) sections at 250 m in Figure 4a - c compare well with validation products (Figure 4d - f). The simulation is able to replicate the expected draw-down of NO_3^- and N_2O and increase in NO_2^- within the core of the OMZ, characteristics of step-wise denitrification. The magnitude and spatial patterns of open ocean concentrations are similarly reproduced, such as the low NO_3^- and N_2O concentrations observed in the subtropical gyre at 25^oS. The oxic to suboxic transition zone (inshore of the 20 $mmol$ O_2 m^{-3} contour in Figure 4) also reveals an increase in N_2O concentrations that skillfully reproduces observational reconstructions discussed in Section 2.2.

The vertical subsurface structure and concentration magnitudes of nitrogen tracers in the ETSP OMZ are shown in Figure 4g - i. Model profiles centered over the OMZ

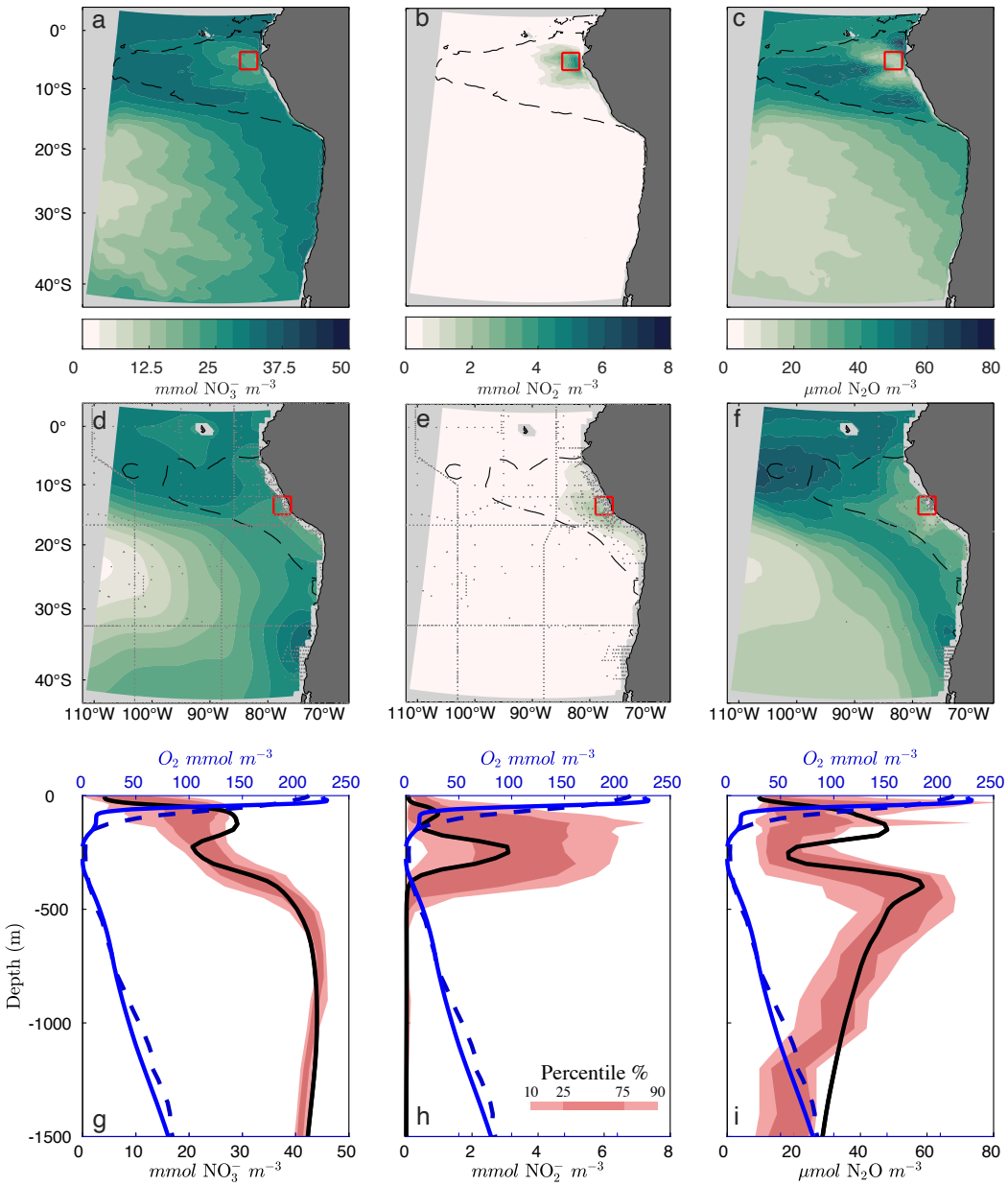

Figure 4. (a-c) ROMS annually averaged NO_3^-, NO_2^-, and N_2O at 250 m from model years 46 - 50. Dashed black lines highlight the 20 $mmol$ O_2 m^{-3} contour. (d-f) NO_3^-, NO_2^-, and N_2O at 250 m from World Ocean Atlas 2018 and machine learning estimates, respectively. Grey markers show the location of shipboard samples. (g-i) Averaged profiles of NO_3^-, NO_2^-, and N_2O from ROMS (black curves) extracted from within the OMZ (red boxes in panels a - c). Shaded regions show the 10th/90th and 25th/75th percentiles of shipboard observations from Kalvelage et al. (2013), Cornejo and Farías (2012), and Krahmann et al. (2021) conducted within the red boxes in panels d - f. Solid blue curves show ROMS O_2 whereas the dashed blue curves show averaged World Ocean Atlas 2018 O_2 over the shipboard sampling region.

show low concentrations at the surface for NO_3^-, NO_2^-, and N_2O. As depth increases, local maxima in NO_2^- and N_2O can be seen at ∼100 m that correspond to low but non-

zero O_2. Just below this depth, where O_2 drops further to anoxic levels, local minima in NO_3^- and N_2O appear along with a large peak in NO_2^- of roughly 3 $mmol\ m^{-3}$. Beneath the anoxic OMZ, a second N_2O peak appears of slightly greater magnitude ($\sim$60 μmol N_2O m^{-3}) to the shallower maxima ($\sim$50 μmol N_2O m^{-3}). Depth-dependent distributions from shipboard measurements (Kalvelage et al., 2013; Cornejo & Farías, 2012; Krahmann et al., 2021) through the OMZ (pink shading) generally show good agreement between model and observations as O_2 increases and decreases vertically. Note that the geographical location of shipboard measurements differs from the ROMS averaging box due to the equatorward and offshore OMZ shift discussed above. Despite this geographical bias, Figures 4g - i demonstrate similarity in the expression of anaerobic nitrogen cycle processes at locations with comparable O_2 profiles. Remaining inconsistencies, such as the shallower depth of the observed upper N_2O maxima, can be explained by the proximity of observations to the coast, as compared to the more offshore location used to average model profiles.

Finally, given the importance of accurately representing water column denitrification, we compared total fixed nitrogen loss in ROMS via denitrification and anammox to other ETSP estimates (Figure 5). Both processes contribute roughly 50% to OMZ N-loss throughout the year, with seasonal variability mostly driven by changes in denitrification rates (red shading). The total water-column fixed nitrogen loss in the model is 25.2 TgN yr^{-1}, within the range of observational estimates for the region (Deutsch et al., 2007; Bianchi et al., 2012; DeVries et al., 2013; Yang et al., 2017). Thus, despite a geographic shift, the model produces a realistic OMZ and associated nitrogen cycle tracers and rates.

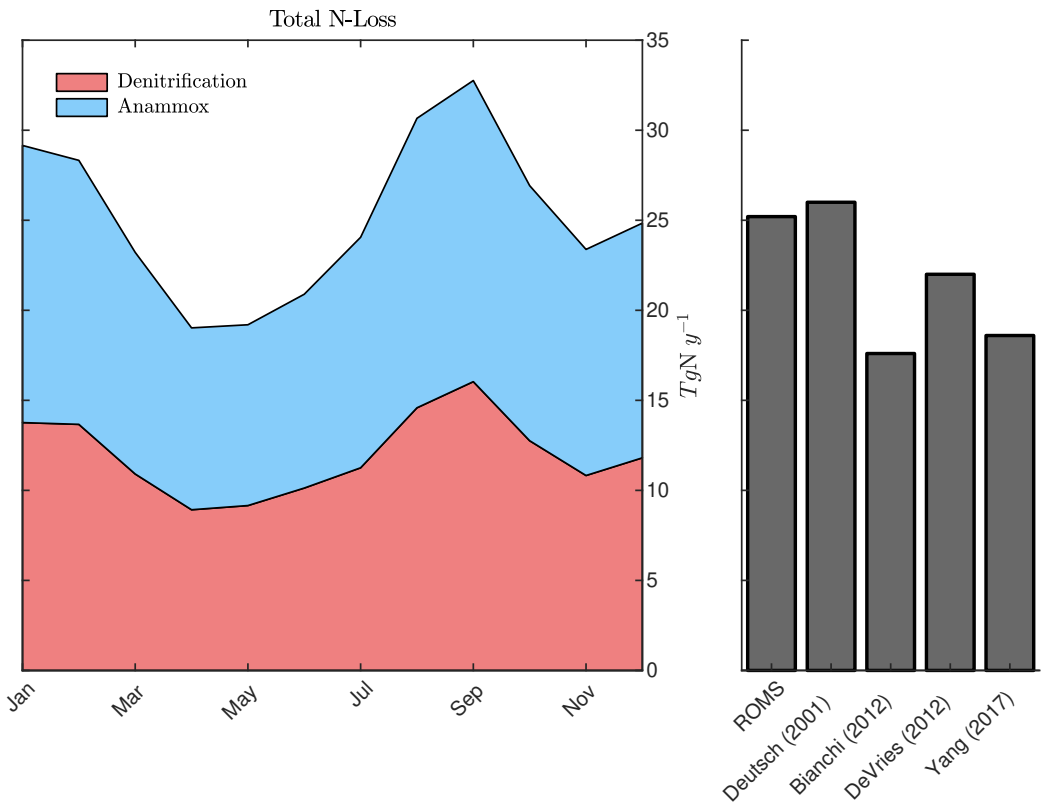

Figure 5. (left) Monthly averaged fixed nitrogen loss from ROMS via canonical denitrification and anammox from models year 46 - 50. (right) ETSP estimates of total annual averaged nitrogen loss from ROMS, Deutsch et al. (2007), Bianchi et al. (2012), DeVries et al. (2013), and Yang et al. (2017).

3.2 ETSP N_2O Production

A transect crossing the core of the model OMZ shows that N_2O production and consumption rates from denitrification are strongly influenced by O_2 concentrations (Figure 6a). Within the anoxic core, N_2O reduction to N_2 ($R^{n_2}_{den3}$) exceeds NO_2^- reduction to N_2O ($R^{n_2o}_{den2}$), causing widespread net N_2O consumption (red shading) of nearly 0.1 μmol N m^{-3} d^{-1}. The resulting N_2O and NO_2^- transects (Figure 6c and 6d) show consistent offshore subsurface N_2O minima coinciding with peak concentrations of NO_2^- at the same depth range. These patterns suggests that all three denitrification steps proceed with minimal O_2 inhibition within the OMZ core, supporting a zone of active fixed N-loss.

Along the exterior of the OMZ core, O_2 gradients preferentially inhibit N_2O reduction to N_2 ($R^{n_2}_{den3}$) and allow incomplete denitrification to proceed. Accordingly, net N_2O consumption transitions to net production (blue shading) of a similar $\sim$0.1 μmol N m^{-3} d^{-1} magnitude (Figure 6a). Beyond suboxic waters, net production from denitrification ceases. In contrast, maximum N_2O production from NH_4^+ oxidation ($R^{n_2o}_{ao}$, Figure 6b) peaks at roughly 0.01 μmol N m^{-3} d^{-1} and is largely restricted to a thin, mostly oxygenated layer at roughly 100 - 150 m that mirrors vertical maxima in POC flux (not shown), with little amplification at low O_2.

The relative contributions from the N_2O tracer decomposition (Figure 6e - h) highlight the disparity between N_2O sources. At the surface, atmospheric ingassing allows

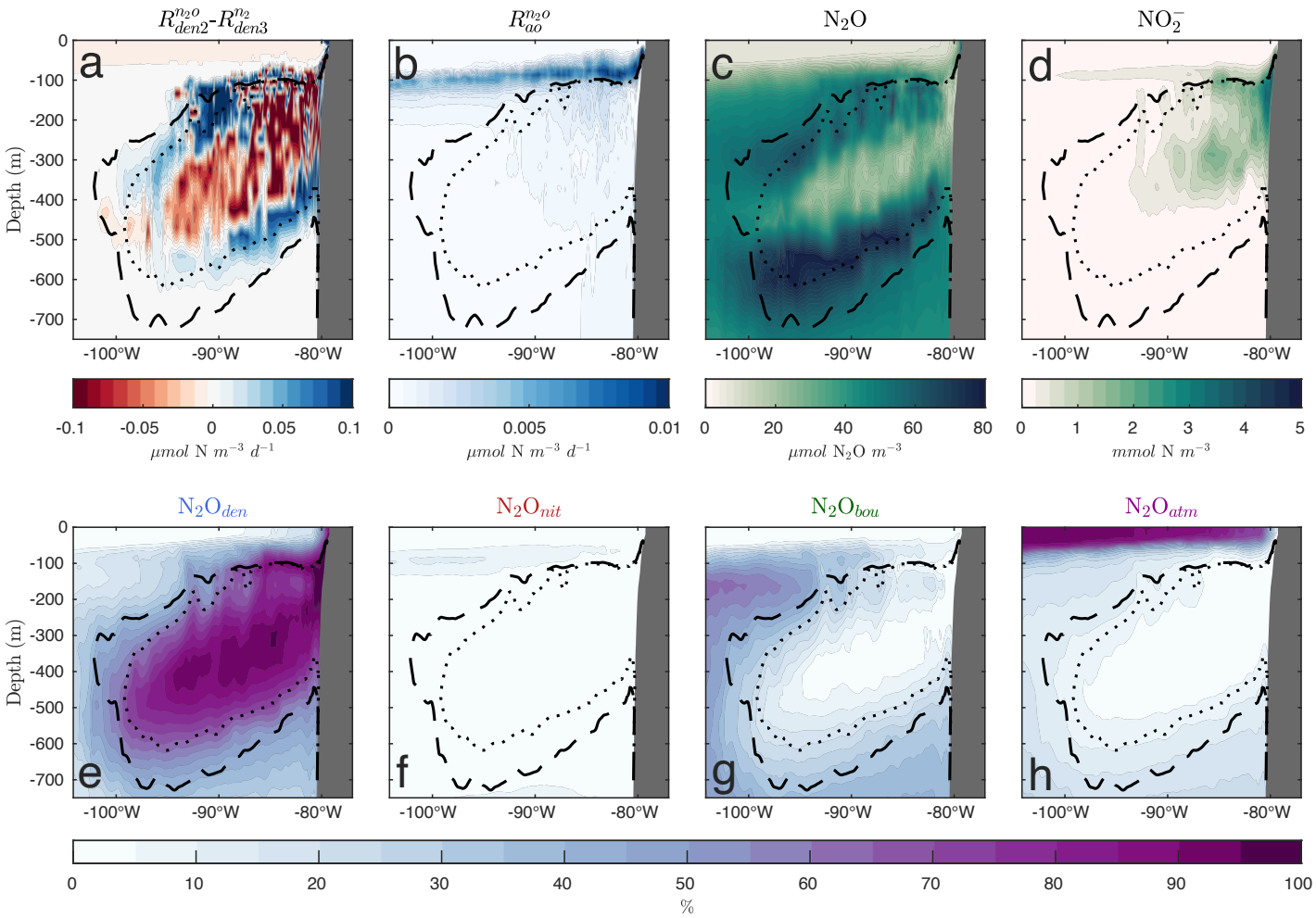

Figure 6. (a) Annually averaged net N_2O production from denitrification for model years 46 - 50 along a transect from the coast at 8^oS. The dotted and dashed black curves in highlight the 5 and 10 $mmol$ O_2 m^{-3} contours, respectively. (b-d) Same as in panel (a), but for N_2O production from nitrification (b), N_2O (c), and NO_2^- (d). Panels (e) - (h) show the relative contributions to N_2O for each decomposed N_2O tracer (N_2O_{den}, N_2O_{nit}, N_2O_{bou}, and N_2O_{atm}).

saturated N_2O (N_2O_{atm}) to dominate (Figure 6h), especially offshore. Within the anoxic OMZ core, despite vigorous net N_2O consumption (Figure 6a), residual N_2O concentrations of $\sim$20 μmol m^{-3} persist (Figure 6c), and are nearly completely attributed to N_2O denitrification (N_2O_{den}, Figure 6e). As O_2 increases beyond suboxic levels, the contribution of N_2O_{den} diminishes, while contributions from supersaturated and saturated N_2O from the boundaries (N_2O_{bou} and N_2O_{atm}, respectively) account for the remainder. In contrast, N_2O from nitrification (N_2O_{nit}, Figure 6f) does not contribute more than 10%, with a maximum at roughly 100 m depth, suggesting that incomplete denitrification is the main contributor ($\mathcal{O}(10)$ times greater production) to local N_2O production throughout the OMZ.

Notably, the contributions from supersaturated and saturated N_2O transported into the OMZ from the model domain boundaries (N_2O_{bou} and N_2O_{atm}, respectively) are rapidly reduced at low O_2, showing consumption of externally derived N_2O within the OMZ core. Additionally, while production from incomplete denitrification is generally confined to

suboxic waters (Figure 6a), significant concentrations of N_2O_{den} in oxygenated waters suggest export of N_2O_{den} out of the OMZ. Together, these results highlight an important role for circulation in redistributing N_2O within the ETSP.

3.3 Contributions of Different Processes to the N_2O Balance

Figure 7 shows vertically-integrated N_2O sources minus sinks (J terms) over the OMZ budget region, and the annual time-series of total integrated net production for N_2O and each decomposed tracer. In general, net N_2O production ($J^{n_2o}_{tot}$, black line in the time-series) is positive for each month with the exception of June, and reveals higher rates beginning in August that persist through December. Production is predominantly driven by denitrification ($J^{n_2o}_{den}$, blue line), which also drives the bulk of monthly variability seen in $J^{n_2o}_{tot}$. In contrast, production from nitrification ($J^{n_2o}_{nit}$, red line) is net positive throughout the year, but only accounts for a small proportion of the N_2O production. Tracers that lack domain production sources (N_2O_{bou} and N_2O_{atm}) show consistent consumption rates throughout the year.

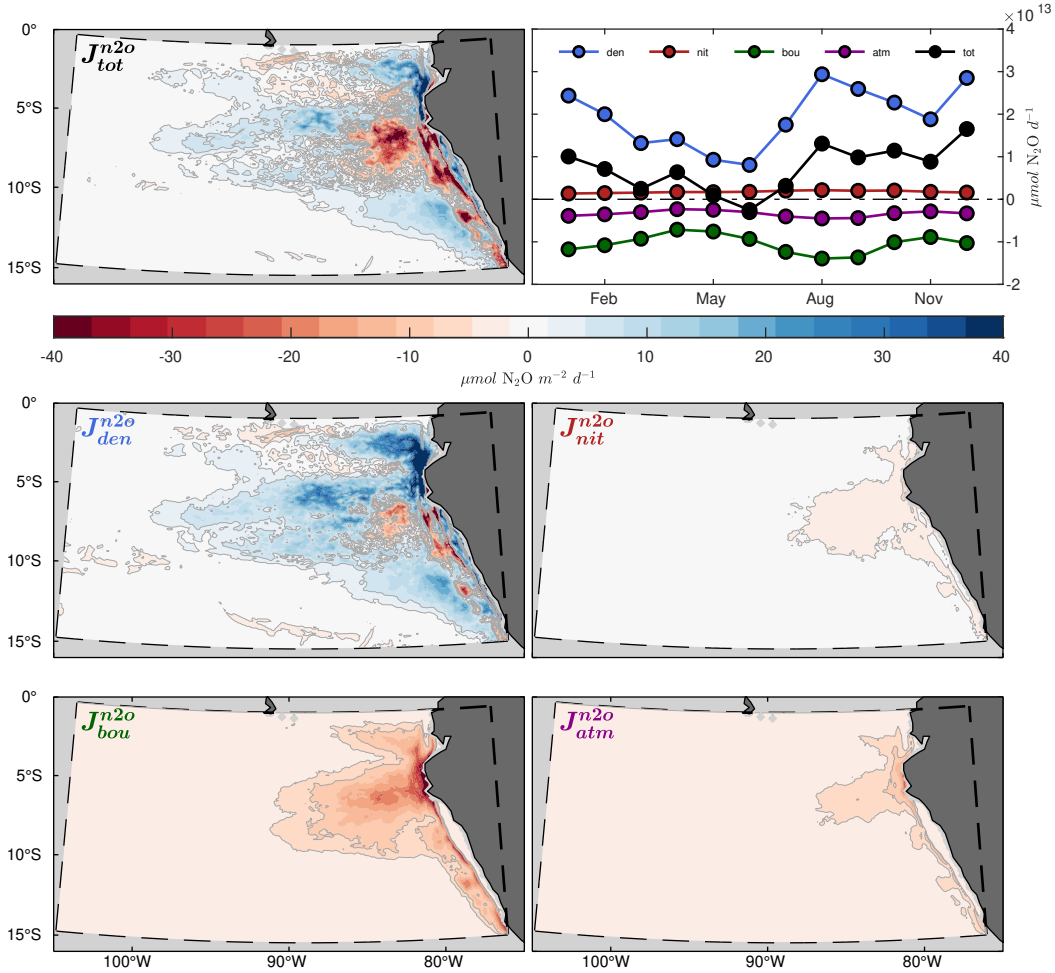

Figure 7. (top left) Vertically integrated sources-minus-sinks (J) for N_2O from the OMZ budget domain, annually averaged from model years 46 - 50. (top right) Time-series of integrated sources-minus-sinks for N_2O (black) and the decomposed N_2O tracers. (bottom panels) Same as in the top left panel, but for each of the decomposed N_2O tracers. Positive values (production) are shown in blue, and negative values (consumption or removal) in red.

Vertically-integrated total N_2O production ($J_{tot}^{n_2o}$) and denitrification-derived production ($J_{den}^{n_2o}$) shown in Figure 7 are similar and reveal a hot-spot of vigorous net consumption (red shading) centered at roughly 8^oS and 80^oW that abruptly transitions to net production (blue shading) in the surrounding ocean. The remaining tracers reveal similar hot-spots of consumption near the coast, especially supersaturated N_2O from the model boundaries ($J_{bou}^{n_2o}$). Integrated N_2O consumption from nitrification ($J_{nit}^{n_2o}$) is balanced by production immediately adjacent to the coastline and in the offshore region that ultimately leads to net production within the budget domain. The region is therefore characterized by a coastal hot-spot of net N_2O consumption that depletes both locally produced N_2O (N_2O_{den} and N_2O_{nit}, blue and red lines respectively) and remote N_2O originating from outside the model domain (N_2O_{bou} and N_2O_{atm}, green and purple lines respectively). Outside the coastal hot-spot, N_2O production from denitrification overcompensates for the consumption at the coast and makes the OMZ a net source of N_2O in all months, with the exception of June. As expected at steady-state, the divergence of advective and diffusive fluxes (T terms) for each N_2O tracer, shown in Figure S11, largely balances the sources minus sinks in Figure 7.

The total N_2O air-sea flux ($\Phi_{tot}^{n_2o}$, black lines in Figure 8) peaks in July and is positive throughout the year, indicating the surface ocean of the ETSP OMZ as a constant source of N_2O to the atmosphere with higher outgassing rates throughout upwelling season (boreal summer). The major contributing components to the flux are supersaturated N_2O from the model boundaries ($\Phi_{bou}^{n_2o}$) and locally produced N_2O from denitrification ($\Phi_{den}^{n_2o}$), which exhibit similar seasonal cycles as in the total flux ($\Phi_{tot}^{n_2o}$), albeit with different geographical distributions. The spatial pattern of $\Phi_{tot}^{n_2o}$ can be described as a combination of $\Phi_{bou}^{n_2o}$ and $\Phi_{den}^{n_2o}$ patterns; $\Phi_{den}^{n_2o}$ is concentrated near the coast with a structure closely mirroring the coastal hot-spot of consumption shown by Figure 7, whereas $\Phi_{bou}^{n_2o}$ takes place mostly along the northern boundary of the budget region (albeit with maximum outgassing near the coast). Since the N_2O_{atm} tracer can be consumed via N_2O reduction within the domain (section 2.4), $\Phi_{atm}^{n_2o}$ similarly tracks the coastal hot-spot, but reveals oceanic ingassing at the surface, peaking in July, which brings N_2O_{atm} back towards saturation. Finally, the magnitude of air-sea flux from local nitrification ($\Phi_{nit}^{n_2o}$) is small but net positive, and shows a similar July maximum peaking near the coast.

3.4 N_2O Balance

A schematic of the annual N_2O balance (Figure 9) shows that total OMZ N_2O production is dominated by incomplete denitrification (174 $Gg\,N\,y^{-1}$), whereas nitrification contributes a smaller fraction (18 $Gg\,N\,y^{-1}$). Conversely, consumption of both saturated and supersaturated N_2O from the model boundaries (N_2O_{atm} and N_2O_{bou}) drives a net N_2O loss (106 and 34 $Gg\,N\,y^{-1}$ respectively). The excess production makes the OMZ a net N_2O source to the atmosphere (51 $Gg\,N\,y^{-1}$). This production takes place predominantly on the fringe of the OMZ both vertically and horizontally, where thick suboxic layers support net N_2O accumulation from the denitrification pathway (Figures 6 and 7).

The budget also suggests that the corresponding outgassing pathways from local production sources are somewhat inefficient; the annual export of 125 and 7 $Gg\,N\,y^{-1}$ of N_2O_{den} and N_2O_{nit} (respectively) suggests that ∼72% and ∼39% of their net production ($J_{den}^{n_2o}$ and $J_{nit}^{n_2o}$, respectively) ultimately avoids outgassing within the budget domain. Yet despite the surprising magnitude of these production export rates, high net import rates of N_2O_{bou} and N_2O_{atm} from the model boundaries (188 and 38 $Gg\,N\,y^{-1}$, respectively) drive an annual net source of 94 $Gg\,N\,y^{-1}$ into the OMZ region. Separating the advective fluxes into zonal, meridional, and vertical components reveals zonal fluxes along the western boundary of the domain as the primary interface of N_2O exchange with the surrounding ocean, organized as alternating narrow bands of N_2O import (Figure S12e, red shading) and export (blue shading). The net transport is driven by supersat-

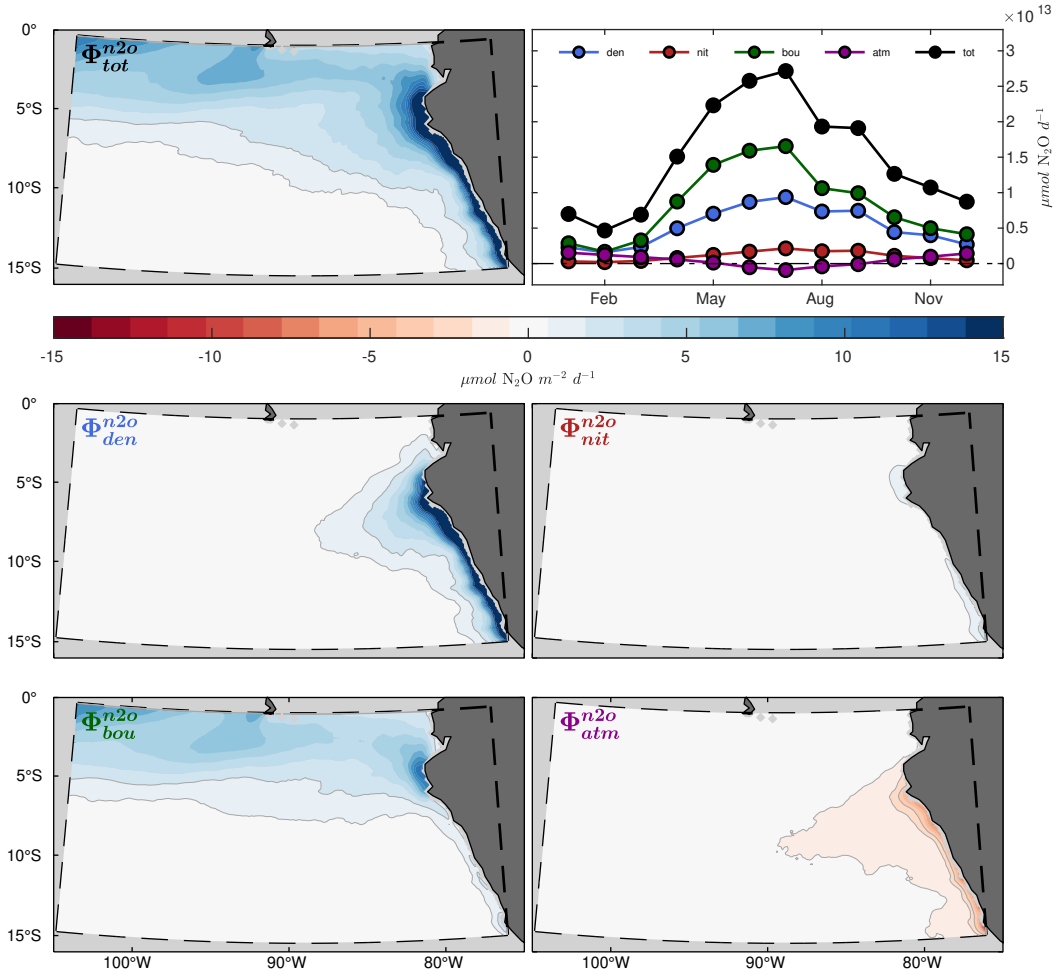

Figure 8. Same as in Figure 7, but for air-sea flux (Φ) of N_2O

urated N_2O (N_2O_{bou}) supplied through the boundaries (Figure S12c), with the most intense import along the equator at roughly 150 m depth (see also Figure 6g). In contrast, denitrification-driven export (Figure S12a) is focused further to the south (roughly 8^oS) and at deeper depths (200 - 500 m, also evident in Figure 6e).

After accounting for boundary exchanges, local subsurface production and consumption, and periodic ingassing of N_2O_{atm} (Figure 8), all tracers reveal net outgassing with $\Phi^{n_2o}_{bou}$ and $\Phi^{n_2o}_{den}$ contributing ~56% and ~34% (respectively) to the annual 152 $Gg\,N\,y^{-1}$ outgassed to the atmosphere. Thus, what emerges from the above descriptions is an ETSP OMZ that is characterized by: (1) A consistent supply of N_2O_{bou} and N_2O_{atm} from predominantly zonal subsurface currents in the tropical band (Figures S11, S12c, and S12e); (2) Advection of all N_2O tracers into a coastal hot-spot where vigorous consumption leads to significant N-loss; (3) Net N_2O production predominantly by denitrification within suboxic gradients surrounding the OMZ (Figure 7); (4) Significant export of N_2O_{den} into the exterior ocean (Figures S11 and S12); (5) Consumption of locally produced and externally derived N_2O; and (6) Year-round air-sea flux of N_2O driven predominantly by imported N_2O_{bou} and locally produced N_2O_{den} that upwell and outgas along the northern extent of the OMZ domain and along the coast, respectively (Figure 8).

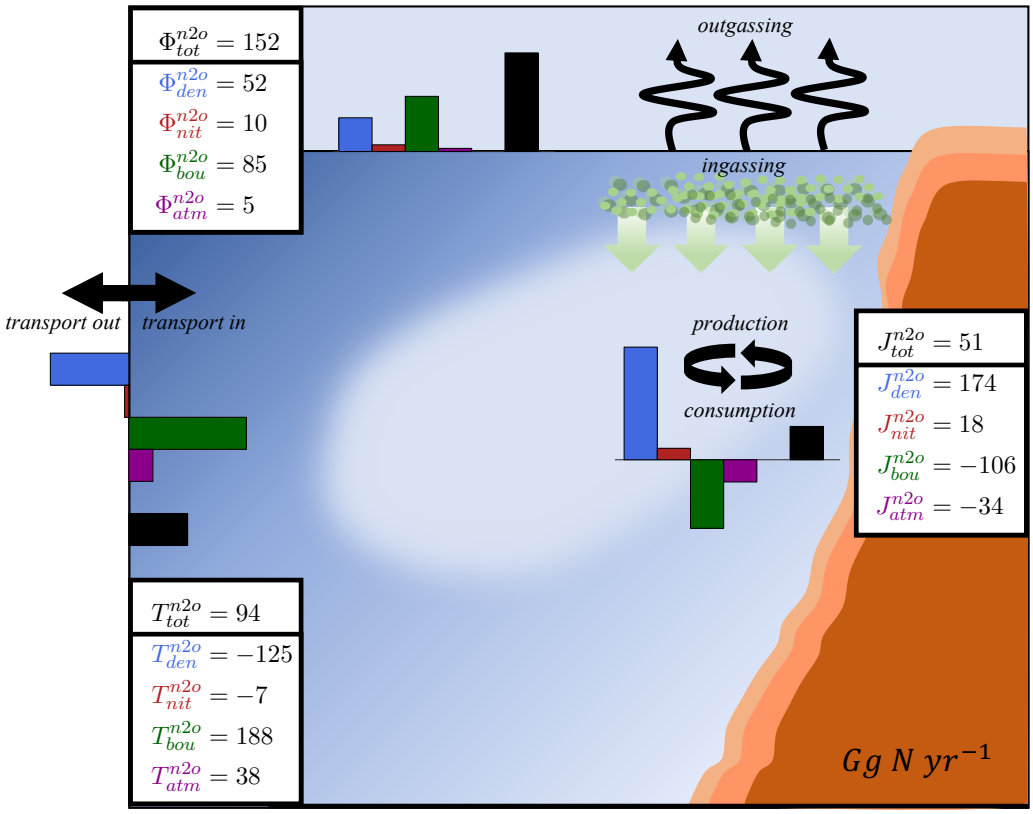

Figure 9. Schematic of the ETSP OMZ N_2O budget, with calculated averages ($Gg\,N\,y^{-1}$) of net air-sea flux (Φ), advection (T), and sources-minus-sinks (J) from model years 46 - 50. Bar plots indicate both the direction of, and relative magnitude of, budget averages.

4 Discussion and Conclusions

We developed a climatological, eddy-resolving simulation of the ETSP OMZ that reproduces the main patterns in the spatial distribution of observed nitrogen tracers and transformation rates. Despite enhanced yields at low O_2, we find almost negligible local contributions from nitrification; rather, maximum N_2O production rates from NH_4^+ oxidation (R^{n2o}_{ao}) follow vertical maxima in POC flux which occur well above the oxycline throughout much of the domain east of -90°W (Figure 6). Closer to shore, as the OMZ core shoals to $\sim$100 m, production from nitrification (J^{n2o}_{nit} in Figure 7) suggests that N_2O_{nit} is subsequently mixed into anoxic waters and consumed via N_2O reduction. The major contribution of nitrification to N_2O production takes place immediately adjacent to the coast, where low O_2 waters at shallow depths lead to enhanced production and an efficient outgassing route. As a result, the air-sea flux pattern in Figure 8 shows negligible contributions from nitrification (Φ^{n2o}_{nit}) throughout the domain, with the exception of coastal outgassing driven by upwelling. While the contribution from nitrification to N_2O production in NitrOMZ is sensitive to the choice of the parameters in equation (1), the values used in this study are constrained by observations (Section 2.3.1) and fall within range of previous estimates (Ji et al., 2018; Santoro et al., 2021) which similarly suggest weak nitrification production. Therefore, similar to the results of Ji et al. (2015) and Babbin et al. (2015), our simulation suggests that local production from nitrification is not a dominant pathway for N_2O outgassing flux in this region.

Instead, N_2O production is dominated by incomplete denitrification which takes place along the suboxic fringes of the anoxic OMZ core (Figure 6a, Figure 6e, and Figure 7), in agreement with recent studies (Babbin et al., 2015; Ji et al., 2018). In general, the three step-wise denitrification rates shows a strong seasonal dependence and are primarily controlled by the timing of organic matter supply from the euphotic zone (Figure S13) rather than variability in low O_2 volumes throughout the year (Figure S14). Within the anoxic core of the OMZ, rapid N_2O consumption rates (Figure 6a) indicate short residence times for N_2O produced via NO_2^- reduction (N_2O_{den}) due to the strong coupling between denitrification steps at low O_2. Significant net N_2O production by denitrification (J_{den}^{n2o}) occurs where high rates of vertical POC flux overlap with an anoxic to suboxic O_2 gradient; there, the difference in O_2 tolerance thresholds leads to a relatively small residual between the large NO_2^- and N_2O reduction rates within the domain (Babbin et al., 2015). As oxic organic matter remineralization stops within the anoxic OMZ core, this leads to the characteristic double peak structure in N_2O profiles (Figure 6c) bounding the OMZ throughout most of the domain.

Spatially, the vertical depth range occupied by anoxic to suboxic gradients plays a key role in determining regions of net production or consumption via the denitrification pathway. For instance, the integrated J_{den}^{n2o} in Figure 7 reveals consumption along the northern extent of the Peruvian coast at roughly 8^oS; considering this pattern, Figure 6a shows relatively sharp O_2 gradients above and below the OMZ around -85°W, indicating that N_2O consumption is particularly strong near the coast, where relatively thin but shallow suboxic layers are found. In contrast, suboxic layers become thicker further offshore, resulting in conditions more favorable to N_2O production. Therefore, the high rates of coastal outgassing observed in Figure 8 are at least partially driven by net transport from more productive surrounding waters (Figure S11).

Our results demonstrate the role of advection in redistributing supersaturated N_2O within the ETSP. Notably, the EUC and SSCC are revealed as zonal conduits controlling the import of supersaturated N_2O (N_2O_{bou}) from the boundaries (and thus, outgassing-favorable N_2O) into the OMZ domain. This is demonstrated by the large fractional contributions to N_2O at 150 m throughout the eastern extent of the transect in Figure 6g, which match subsurface patterns in Figure S12c. These results are consistent with those from Yang et al. (2020), who highlighted the tropics in the Eastern Pacific as an important outgassing region with seasonality driven predominantly by the timing of upwelling (May to September). While a significant fraction of the imported N_2O is ultimately advected into the anoxic OMZ to be consumed (Figures 6g and 7), the remainder is responsible for the bulk ($\sim$56%) of the outgassing flux over the OMZ domain. As the N_2O budget and boundary export schematic in Figures 9 and S12 show, circulation also plays a key role in exporting the majority (roughly 72%) of local denitrification-derived N_2O production (J_{den}^{n2o}) out of the OMZ budget domain. Much of this export takes place along the western boundary (Figure S12), but at more southerly latitudes and at deeper depths compared to the import of supersaturated N_2O from the boundaries (T_{bou}^{n2o}). Unfortunately, our regional simulations do not allow us to explore the fate of this N_2O. Global or basin-wide simulations would enable tracking the interplay of N_2O sources and sinks within and outside OMZs. A portion of the denitrification-derived N_2O export may recirculate back into the eastward equatorial currents, or could instead add to N_2O concentrations in offshore waters, such a those observed by Santoro et al. (2021).

The residual between rapid N_2O production and consumption by denitrification is heavily coupled to O_2 dynamics and thus a major portion of N_2O outgassing in this region is likely sensitive to future changes in OMZ magnitude and geometry. Observations suggest that deoxygenation over the past 50 years has led to expansion of OMZ volumes and shoaling of the upper oxycline (Stramma et al., 2008; Schmidtko et al., 2017). Yet, whether this has caused a positive or negative impact on N_2O production likely depends on the relative changes of anoxic versus suboxic volumes. If future climate change

results in an increase in the volume of suboxic waters, as suggested by Earth system model projections (Cabré et al., 2015; Kwiatkowski et al., 2020; Busecke et al., 2019), it would increase production from both incomplete denitrification and nitrification, leading to a positive climate feedback. Conversely, an increase in the volume of anoxic waters may drive enhanced N_2O consumption and constitute a negative climate feedback.

Future changes in the oxycline depth via projected stratification or wind changes (Kwiatkowski et al., 2020; Busecke et al., 2019; Bakun, 1990) may alter the coupling between local production and outgassing over OMZs, while also affecting the export of supersaturated N_2O into the nearby gyres. The lack of interannual forcing in this study also leaves gaps in understanding ENSO impacts. OMZ geometry and total denitrification rates are sensitive to ENSO variability (Yang et al., 2017), thus N_2O production and outgassing are likely to exhibit similar year-to-year changes. Interannually forced, high-resolution models capable of simulating both denitrification and nitrification-derived production are needed to resolve these emerging questions.

Open Research Section

The ROMS model code used to generate the simulation (Shchepetkin & McWilliams, 2005; Shchepetkin, 2015), and the MATLAB (MATLAB, 2020) scripts and output used to generate the figures shown in the paper, can be found at https://doi.org/10.5281/zenodo.7374360 (McCoy et al., 2022). Raw model output can be obtained from the Authors upon request. Biogeochemical validation data were provided by the World Ocean Atlas 2018 (H. Garcia et al., 2019a, 2019b), MEMENTO (Kock & Bange, 2015) and GLODAPv2 (Key et al., 2015; Lauvset et al., 2016) databases, with additional shipboard observations from Kalvelage et al. (2013), Cornejo and Farías (2012), and Krahmann et al. (2021). The MEMENTO database is administered by the Kiel Data Management Team at GEOMAR Helmholtz Centre for Ocean Research and supported by the German BMBF project SOPRAN (Surface Ocean Processes in the Anthropocene, http://sopran.pangaea.de). The database is accessible through the MEMENTO webpage (https://memento.geomar.de). AVISO satellite data used in model validation were processed by SSALTO/DUACS and distributed by AVISO+ at https://www.aviso.altimetry.fr with support from CNES. MODIS L3 ocean color data were obtained from the NASA/GSFC MODAPS Service website at https://oceancolor.gsfc.nasa.gov/l3/. The ERA-Interim dataset (Dee et al., 2011), which was used to force the model, was obtained from the European Centre for Medium-Range Weather Forecasts (ECMWF) at https://www.ecmwf.int. Thanks to ICDC, CEN, University of Hamburg for data support in obtaining ERA-Interim products.

Acknowledgments

This material is based upon work supported by the U.S. National Science Foundation under grant OCE-1847687. D.B. acknowledges support from the Alfred P. Sloan Foundation, and computational support by the Extreme Science and Engineering Discovery Environment (XSEDE) through allocation TG-OCE17001.

References

Anderson, L. A., & Sarmiento, J. L. (1994, 3). Redfield ratios of remineralization determined by nutrient data analysis. *Global Biogeochemical Cycles*, *8*(1), 65–80. Retrieved from `http://doi.wiley.com/10.1029/93GB03318` doi: 10.1029/93GB03318

Arévalo-Martínez, D. L., Kock, A., Löscher, C. R., Schmitz, R. A., Stramma, L., & Bange, H. W. (2015). Influence of mesoscale eddies on the distribution of nitrous oxide in the eastern tropical South Pacific. *Biogeosciences Discussions*, *12*(12), 9243–9273. doi: 10.5194/bgd-12-9243-2015

Babbin, A. R., Bianchi, D., Jayakumar, A., & Ward, B. B. (2015). Rapid nitrous oxide cycling in the suboxic ocean. *Science*, *348*(6239), 1127–1129. doi: 10.1126/science.aaa8380

Babbin, A. R., Buchwald, C., Morel, F. M., Wankel, S. D., & Ward, B. B. (2020). Nitrite oxidation exceeds reduction and fixed nitrogen loss in anoxic Pacific waters. *Marine Chemistry*, *224*(April). doi: 10.1016/j.marchem.2020.103814

Babbin, A. R., Peters, B. D., Mordy, C. W., Widner, B., Casciotti, K. L., & Ward, B. B. (2017). Multiple metabolisms constrain the anaerobic nitrite budget in the Eastern Tropical South Pacific. *Global Biogeochemical Cycles*, *31*(2), 258–271. doi: 10.1002/2016GB005407

Bakun, A. (1990). Global climate change and intensification of coastal ocean upwelling. *Science*, *247*(4939), 198–201.

Battaglia, G., & Joos, F. (2018). Marine N2O Emissions From Nitrification and Denitrification Constrained by Modern Observations and Projected in Multimillennial Global Warming Simulations. *Global Biogeochemical Cycles*, *32*(1), 92–121. doi: 10.1002/2017GB005671

Behrenfeld, M. J., Boss, E., Siegel, D. A., & Shea, D. M. (2005, 3). Carbon-based ocean productivity and phytoplankton physiology from space. *Global Biogeochemical Cycles*, *19*(1). Retrieved from `http://doi.wiley.com/10.1029/2004GB002299` doi: 10.1029/2004GB002299

Behrenfeld, M. J., & Falkowski, P. G. (1997, 1). Photosynthetic rates derived from satellite-based chlorophyll concentration. *Limnology and Oceanography*, *42*(1), 1–20. Retrieved from `http://doi.wiley.com/10.4319/lo.1997.42.1.0001` doi: 10.4319/lo.1997.42.1.0001

Bettencourt, J. H., Lopez, C., Hernandez-Garcia, E., Montes, I., Sudre, J., Dewitte, B., ... Garçon, V. (2015, 12). Boundaries of the Peruvian oxygen minimum zone shaped by coherent mesoscale dynamics. *Nature Geoscience*, *8*(12), 937–940. doi: 10.1038/ngeo2570

Bianchi, D., Dunne, J. P., Sarmiento, J. L., & Galbraith, E. D. (2012). Data-based estimates of suboxia, denitrification, and N2O production in the ocean and their sensitivities to dissolved O2. *Global Biogeochemical Cycles*, *26*(January 2016). doi: 10.1029/2011GB004209

Bianchi, D., McCoy, D., & Yang, S. (2022). Formulation, optimization and sensitivity of nitromzv1.0, a biogeochemical model of the nitrogen cycle in oceanic oxygen minimum zones. *Geoscientific Model Development Discussions*. doi: 10.5194/gmd-2022-244

Bianchi, D., Weber, T. S., Kiko, R., & Deutsch, C. (2018, 4). Global niche of marine anaerobic metabolisms expanded by particle microenvironments. *Nature Geoscience*, *11*(4), 263–268. Retrieved from `http://www.nature.com/articles/s41561-018-0081-0` doi: 10.1038/s41561-018-0081-0

Bourbonnais, A., Letscher, R. T., Bange, H. W., Échevin, V., Larkum, J., Mohn, J., ... Altabet, M. A. (2017, 4). N2O production and consumption from stable isotopic and concentration data in the Peruvian coastal upwelling system. *Global Biogeochemical Cycles*, *31*(4), 678–698. Retrieved from `http://doi.wiley.com/10.1002/2016GB005567` doi: 10.1002/2016GB005567

Brodeau, L., Barnier, B., Treguier, A.-M., Penduff, T., & Gulev, S. (2010, 1). An ERA40-based atmospheric forcing for global ocean circulation models. *Ocean Modelling*, *31*(3-4), 88–104. doi: 10.1016/j.ocemod.2009.10.005

Busecke, J. J., Resplandy, L., & Dunne, J. P. (2019, 6). The Equatorial Undercurrent and the Oxygen Minimum Zone in the Pacific. *Geophysical Research Letters*, *46*(12), 6716–6725. doi: 10.1029/2019GL082692

Busecke, J. J., Resplandy, L., & John, J. G. (2021). Future expansion of the pacific oxygen minimum zone. *Earth and Space Science Open Archive*, 25. Retrieved from `https://doi.org/10.1002/essoar.10507050.1` doi: 10.1002/essoar.10507050.1

Cabré, A., Marinov, I., Bernardello, R., & Bianchi, D. (2015, 9). Oxygen minimum zones in the tropical Pacific across CMIP5 models: Mean state differences and climate change trends. *Biogeosciences*, *12*(18), 5429–5454. doi: 10.5194/bg-12-5429-2015

Canadell, J. G., Scheel Monteiro, P., Costa, M. H., Cotrim da Cunha, L., Cox, P. M., Eliseev, A. V., ... Zickfeld, K. (2021). *Chapter 5: Global Carbon and other Biogeochemical Cycles and Feedbacks. In Climate Change 2021: The Physical Science Basis. Contribution of Working Group I to the Sixth Assessment Report of the Intergovernmental Panel on Climate Change* . Cambridge University Press.

Chavez, F. P., & Messié, M. (2009). A comparison of Eastern Boundary Upwelling Ecosystems. *Progress in Oceanography*, *83*(1-4), 80–96. Retrieved from `http://dx.doi.org/10.1016/j.pocean.2009.07.032` doi: 10.1016/j.pocean.2009.07.032

Codispoti, L. A. (2010). Interesting times for marine N2O. *Science*, *327*(5971), 1339–1340. doi: 10.1126/science.1184945

Cohen, Y., & Gordon, L. I. (1978, 6). Nitrous oxide in the oxygen minimum of the eastern tropical North Pacific: evidence for its consumption during denitrification and possible mechanisms for its production. *Deep Sea Research*, *25*(6), 509–524. doi: 10.1016/0146-6291(78)90640-9

Cornejo, M., & Farías, L. (2012). Following the N2O consumption in the oxygen minimum zone of the eastern South Pacific. *Biogeosciences*, *9*(8), 3205–3212. doi: 10.5194/bg-9-3205-2012

Dalsgaard, T., Stewart, F. J., Thamdrup, B., De Brabandere, L., Revsbech, N. P., Ulloa, O., ... Delong, E. F. (2014). Oxygen at nanomolar levels reversibly suppresses process rates and gene expression in anammox and denitrification in the oxygen minimum zone off Northern Chile. *mBio*, *5*(6), 1–14. doi: 10.1128/mBio.01966-14

Dee, D. P., Uppala, S. M., Simmons, A. J., Berrisford, P., Poli, P., Kobayashi, S., ... Vitart, F. (2011). The ERA-Interim reanalysis: Configuration and performance of the data assimilation system. *Quarterly Journal of the Royal Meteorological Society*, *137*(656), 553–597. doi: 10.1002/qj.828

Deutsch, C., Frenzel, H., McWilliams, J. C., Renault, L., Kessouri, F., Howard, E., ... Yang, S. (2021). Biogeochemical variability in the california current system. *Progress in Oceanography*, *196*, 102565. Retrieved from `https://www.sciencedirect.com/science/article/pii/S0079661121000525` doi: https://doi.org/10.1016/j.pocean.2021.102565

Deutsch, C., Sarmiento, J. L., Sigman, D. M., Gruber, N., & Dunne, J. P. (2007, 1). Spatial coupling of nitrogen inputs and losses in the ocean. *Nature*, *445*(7124), 163–167. doi: 10.1038/nature05392

DeVries, T., Deutsch, C., Rafter, P. A., & Primeau, F. (2013, 4). Marine denitrification rates determined from a global 3-D inverse model. *Biogeosciences*, *10*(4), 2481–2496. doi: 10.5194/bg-10-2481-2013

Dunn, J. (2012, 2). *CSIRO Atlas of Regional Seas (CARS) - 2009.* Tasmanian Partnership for Advanced Computing. Retrieved from `http://dl.tpac.org.au/tpacportal/#dataset=144,https://researchdata.edu.au/csiro-atlas-regional-cars-2009`

Dussin, R., Barnier, B., & Brodeau, L. (2014). The Making of the DRAKKAR FORCING SET DFS5. doi: 10.5281/zenodo.1209243

Duteil, O., Frenger, I., & Getzlaff, J. (2021, 10). The riddle of eastern tropical Pacific Ocean oxygen levels: the role of the supply by intermediate-depth waters. *Ocean Science*, *17*(5), 1489–1507. Retrieved from `https://os.copernicus.org/articles/17/1489/2021/` doi: 10.5194/os-17-1489-2021

Duteil, O., Schwarzkopf, F. U., Böning, C. W., & Oschlies, A. (2014, 3). Major role of the equatorial current system in setting oxygen levels in the eastern tropical Atlantic Ocean: A high-resolution model study. *Geophysical Research Letters*, *41*(6), 2033–2040. Retrieved from `http://doi.wiley.com/10.1002/2013GL058888` doi: 10.1002/2013GL058888

Freing, A., Wallace, D. W., & Bange, H. W. (2012). Global oceanic production of nitrous oxide. *Philosophical Transactions of the Royal Society B: Biological Sciences*, *367*(1593), 1245–1255. doi: 10.1098/rstb.2011.0360

Frischknecht, M., Münnich, M., & Gruber, N. (2017, 1). Local atmospheric forcing driving an unexpected California Current System response during the 2015–2016 El Niño. *Geophysical Research Letters*, *44*(1), 304–311. doi: 10.1002/2016GL071316

Ganesh, S., Parris, D. J., Delong, E. F., & Stewart, F. J. (2014). Metagenomic analysis of size-fractionated picoplankton in a marine oxygen minimum zone. *The ISME Journal*, *8*, 187–211. Retrieved from `www.nature.com/ismej` doi: 10.1038/ismej.2013.144

Garcia, H., Weathers, K., Paver, C., Smolyar, I., Boyer, T., Locarnini, M., ... Reagan, J. (2019a). World Ocean Atlas 2018, Volume 3: Dissolved Oxygen, Apparent Oxygen Utilization, and Dissolved Oxygen Saturation. *NOAA Atlas NESDIS*, *83*.

Garcia, H., Weathers, K., Paver, C., Smolyar, I., Boyer, T., Locarnini, M., ... Reagan, J. (2019b). World ocean atlas 2018, volume 4: Dissolved inorganic nutrients (phosphate, nitrate and nitrate+nitrite, silicate). *NOAA Atlas NESDIS*, *83*.

Garcia, H. E., Boyer, T. P., Locarnini, R. A., Antonov, J. I., Mishonov, A. V., Baranova, O. K., ... Johnson, D. R. (2013). World Ocean Atlas 2013. Volume 3: dissolved oxygen, apparent oxygen utilization, and oxygen saturation. *NOAA Atlas NESDIS 75*, *3*(September), 27.

Garcia, H. E., Locarnini, R., Boyer, T. P., Antonov, J. I., Baranova, O. K., Zweng, M. M., ... Johnson, D. R. (2013). World Ocean Atlas 2013 Volume 4 : Nutrients (phosphate , nitrate , silicate). *NOAA Atlas NESDIS 76*, *4*(September), 396.

Gnanadesikan, A., Bianchi, D., & Pradal, M. A. (2013, 10). Critical role for mesoscale eddy diffusion in supplying oxygen to hypoxic ocean waters. *Geophysical Research Letters*, *40*(19), 5194–5198. doi: 10.1002/GRL.50998

Goreau, T. J., Kaplan, W. A., Wofsy, S. C., McElroy, M. B., Valois, F. W., & Watson, S. W. (1980, 9). Production of NO(2) and N(2)O by Nitrifying Bacteria at Reduced Concentrations of Oxygen. *Applied and environmental microbiology*, *40*(3), 526–32. Retrieved from `http://www.ncbi.nlm.nih.gov/pubmed/16345632http://www.pubmedcentral.nih.gov/articlerender.fcgi?artid=PMC291617` doi: 10.1128/aem.40.3.526-532.1980

IPCC. (2013). *Climate Change 2013: The Physical Science Basis. Contribution of Working Group I to the Fifth Assessment Report of the Intergovernmental Panel on Climate Change*. Cambridge, United Kingdom and New York, NY, USA: Cambridge University Press. Retrieved from `www.climatechange2013.org` doi: 10.1017/CBO9781107415324

Ji, Q., Babbin, A. R., Peng, X., Bowen, J. L., & Ward, B. B. (2015). Nitrogen substrate–dependent nitrous oxide cycling in salt marsh sediments. *Journal of Marine Research*, *73*(3-4), 71–92. doi: 10.1357/002224015815848820

Ji, Q., Buitenhuis, E., Suntharalingam, P., Sarmiento, J. L., & Ward, B. B. (2018). Global Nitrous Oxide Production Determined by Oxygen Sensitivity of Nitrification and Denitrification. *Global Biogeochemical Cycles*, *32*(12), 1790–1802. doi: 10.1029/2018GB005887

Jin, X., & Gruber, N. (2003). Offsetting the radiative benefit of ocean iron fertilization by enhancing N2O emissions. *Geophysical Research Letters*, *30*(24), 1–

4. doi: 10.1029/2003GL018458

Johnson, G. C., Sloyan, B. M., Kessler, W. S., & McTaggart, K. E. (2002). Direct measurements of upper ocean currents and water properties across the tropical Pacific during the 1990s. *Progress in Oceanography*, *52*(1), 31–61. doi: 10.1016/S0079-6611(02)00021-6

Kalvelage, T., Jensen, M. M., Contreras, S., Revsbech, N. P., Lam, P., Günter, M., … Kuypers, M. M. (2011). Oxygen sensitivity of anammox and coupled N-cycle processes in oxygen minimum zones. *PLoS ONE*, *6*(12). doi: 10.1371/journal.pone.0029299

Kalvelage, T., Lavik, G., Lam, P., Contreras, S., Arteaga, L., Löscher, C. R., … Kuypers, M. M. (2013). Nitrogen cycling driven by organic matter export in the South Pacific oxygen minimum zone. *Nature Geoscience*, *6*(3), 228–234. doi: 10.1038/ngeo1739

Karstensen, J., Stramma, L., & Visbeck, M. (2008, 6). Oxygen minimum zones in the eastern tropical Atlantic and Pacific oceans. *Progress in Oceanography*, *77*(4), 331–350. Retrieved from `https://linkinghub.elsevier.com/retrieve/pii/S0079661108000670` doi: 10.1016/j.pocean.2007.05.009

Kessler, W. S. (2006, 5). The circulation of the eastern tropical Pacific: A review. *Progress in Oceanography*, *69*(2-4), 181–217. Retrieved from `https://linkinghub.elsevier.com/retrieve/pii/S0079661106000310` doi: 10.1016/j.pocean.2006.03.009

Key, R., Olsen, A., Van Heuven, S., Lauvset, S., Velo, A., Lin, X., … Suzuki, T. (2015). *Global ocean data analysis project, version 2 (glodapv2), ornl/cdiac-162, nd-p093.* Carbon Dioxide Information Analysis Center (CDIAC). Retrieved from `http://cdiac.ornl.gov/ftp/oceans/GLODAPv2/Data_Products/` doi: 10.3334/CDIAC/OTG.NDP093_GLODAPV2

Kock, A., Arevalo-Martinez, D. L., Loscher, C. R., & Bange, H. W. (2016). Extreme N2O accumulation in the coastal oxygen minimum zone off Peru. *Biogeosciences*, *13*(3), 827–840. doi: 10.5194/bg-13-827-2016

Kock, A., & Bange, H. (2015, 2). Counting the Ocean's Greenhouse Gas Emissions. *Eos*, *96*. doi: 10.1029/2015EO023665

Körner, H., & Zumft, W. G. (1989, 7). Expression of denitrification enzymes in response to the dissolved oxygen level and respiratory substrate in continuous culture of Pseudomonas stutzeri. *Applied and Environmental Microbiology*, *55*(7), 1670–1676. doi: 10.1128/aem.55.7.1670-1676.1989

Krahmann, G., Arévalo-martínez, D. L., Dale, A. W., Dengler, M., Engel, A., Glock, N., … Hansell, D. A. (2021). Climate-Biogeochemistry Interactions in the Tropical Ocean : Data Collection and Legacy. *Frontiers in Marine Science*, *8*(September), 1–23. doi: 10.3389/fmars.2021.723304

Kuypers, M. M., Marchant, H. K., & Kartal, B. (2018). The microbial nitrogen-cycling network. *Nature Reviews Microbiology*, *16*(5), 263–276.

Kwiatkowski, L., Torres, O., Bopp, L., Aumont, O., Chamberlain, M., Christian, J. R., … Ziehn, T. (2020, 7). Twenty-first century ocean warming, acidification, deoxygenation, and upper-ocean nutrient and primary production decline from CMIP6 model projections. *Biogeosciences*, *17*(13), 3439–3470. Retrieved from `https://bg.copernicus.org/articles/17/3439/2020/` doi: 10.5194/bg-17-3439-2020

Kwiecinski, J. V., & Babbin, A. R. (2021, 12). A High-Resolution Atlas of the Eastern Tropical Pacific Oxygen Deficient Zones. *Global Biogeochemical Cycles*, *35*(12). doi: 10.1029/2021GB007001

Lam, P., & Kuypers, M. M. (2011). Microbial Nitrogen Cycling Processes in Oxygen Minimum Zones. *Annual Review of Marine Science*, *3*(1), 317–345. doi: 10.1146/annurev-marine-120709-142814

Large, W. B. (2006). Surface Fluxes for Practitioners of Global Ocean Data Assimilation. In E. P. Chassignet & J. Verron (Eds.), *Ocean weather forecasting:*

An integrated view of oceanography (pp. 229–270). Dordrecht: Springer Netherlands. Retrieved from https://doi.org/10.1007/1-4020-4028-8_9 doi: 10.1007/1-4020-4028-8{_}9

Lauvset, S. K., Key, R. M., Olsen, A., Van Heuven, S., Velo, A., Lin, X., ... Watelet, S. (2016). A new global interior ocean mapped climatology: The 1° × 1° GLODAP version 2. *Earth System Science Data*, *8*(2), 325–340. doi: 10.5194/essd-8-325-2016

Lemarié, F., Kurian, J., Shchepetkin, A. F., Jeroen Molemaker, M., Colas, F., & McWilliams, J. C. (2012). Are there inescapable issues prohibiting the use of terrain-following coordinates in climate models? *Ocean Modelling*, *42*, 57–79. doi: 10.1016/j.ocemod.2011.11.007

Löscher, C. R., Kock, A., Könneke, M., Laroche, J., Bange, H. W., & Schmitz, R. A. (2012). Production of oceanic nitrous oxide by ammonia-oxidizing archaea. *Biogeosciences*, *9*(7), 2419–2429. doi: 10.5194/bg-9-2419-2012

Luyten, J. R., Pedlosky, J., & Stommel, H. (1983, 2). The Ventilated Thermocline. *Journal of Physical Oceanography*, *13*(2), 292–309. doi: 10.1175/1520-0485(1983)013⟨0292:TVT⟩2.0.CO;2

MATLAB. (2020). *Version 9.9.0.1495850 (r2020b) update 1.* Natick, Massachusetts: The MathWorks Inc.

McCoy, D., Damien, P., Clements, D., Yang, S., & Bianchi, D. (2022, November). *Data and source code for "Pathways of Nitrous Oxide Production in the Eastern Tropical South Pacific Oxygen Minimum Zone".* Zenodo. Retrieved from https://doi.org/10.5281/zenodo.7374360 doi: 10.5281/zenodo.7374360

Moore, J. K., Doney, S. C., & Lindsay, K. (2004, 12). Upper ocean ecosystem dynamics and iron cycling in a global three-dimensional model. *Global Biogeochemical Cycles*, *18*(4), n/a-n/a. Retrieved from http://doi.wiley.com/10.1029/2004GB002220 doi: 10.1029/2004GB002220

Nevison, C., Butler, J. H., & Elkins, J. W. (2003, 12). Global distribution of N 2 O and the ΔN 2 O-AOU yield in the subsurface ocean. *Global Biogeochemical Cycles*, *17*(4), n/a-n/a. Retrieved from http://doi.wiley.com/10.1029/2003GB002068 doi: 10.1029/2003GB002068

Olsen, A., Key, R. M., van Heuven, S., Lauvset, S. K., Velo, A., Lin, X., ... Suzuki, T. (2016, 8). The Global Ocean Data Analysis Project version 2 (GLODAPv2) – an internally consistent data product for the world ocean. *Earth System Science Data*, *8*(2), 297–323. doi: 10.5194/essd-8-297-2016

Oschlies, A., Brandt, P., Stramma, L., & Schmidtko, S. (2018). Drivers and mechanisms of ocean deoxygenation. *Nature Geoscience*, *11*(7), 467–473. Retrieved from http://dx.doi.org/10.1038/s41561-018-0152-2 doi: 10.1038/s41561-018-0152-2

Peng, X., Fuchsman, C. A., Jayakumar, A., Warner, M. J., Devol, A. H., & Ward, B. B. (2016). Journal of Geophysical Research : Oceans Revisiting nitrification in the Eastern Tropical South Pacific : A focus on controls. *Journal of Geophysical Research: Oceans*, *121*(3), 1667–1684. doi: 10.1002/2015JC011455.Received

Pennington, J. T., Mahoney, K. L., Kuwahara, V. S., Kolber, D. D., Calienes, R., & Chavez, F. P. (2006, 5). Primary production in the eastern tropical Pacific: A review. *Progress in Oceanography*, *69*(2-4), 285–317. doi: 10.1016/j.pocean.2006.03.012

Ravishankara, A. R., Daniel, J. S., & Portmann, R. W. (2009, 10). Nitrous Oxide (N ¡sub¿2¡/sub¿ O): The Dominant Ozone-Depleting Substance Emitted in the 21st Century. *Science*, *326*(5949), 123–125. doi: 10.1126/science.1176985

Risien, C. M., & Chelton, D. B. (2008). A global climatology of surface wind and wind stress fields from eight years of QuikSCAT scatterometer data. *Journal of Physical Oceanography*, *38*(11), 2379–2413. doi: 10.1175/2008JPO3881.1

Santoro, A. E., Buchwald, C., Knapp, A. N., Berelson, W. M., Capone, D. G., & Casciotti, K. L. (2021, 2). Nitrification and Nitrous Oxide Production in the Offshore Waters of the Eastern Tropical South Pacific. *Global Biogeochemical Cycles*, *35*(2), 1–35. Retrieved from https://onlinelibrary.wiley.com/doi/10.1029/2020GB006716 doi: 10.1029/2020GB006716

Schmidtko, S., Stramma, L., & Visbeck, M. (2017, 2). Decline in global oceanic oxygen content during the past five decades. *Nature*, *542*(7641), 335–339. doi: 10.1038/nature21399

Séférian, R., Berthet, S., Yool, A., Palmieri, J., Bopp, L., Tagliabue, A., ... others (2020). Tracking improvement in simulated marine biogeochemistry between cmip5 and cmip6. *Current Climate Change Reports*, *6*(3), 95–119.

Shchepetkin, A. F. (2015). An adaptive, Courant-number-dependent implicit scheme for vertical advection in oceanic modeling. *Ocean Modelling*, *91*, 38–69.

Shchepetkin, A. F., & McWilliams, J. C. (2005, 1). The regional oceanic modeling system (ROMS): a split-explicit, free-surface, topography-following-coordinate oceanic model. *Ocean Modelling*, *9*(4), 347–404. doi: 10.1016/J.OCEMOD.2004.08.002

Silsbe, G. M., Behrenfeld, M. J., Halsey, K. H., Milligan, A. J., & Westberry, T. K. (2016, 12). The CAFE model: A net production model for global ocean phytoplankton. *Global Biogeochemical Cycles*, *30*(12), 1756–1777. Retrieved from http://doi.wiley.com/10.1002/2016GB005521 doi: 10.1002/2016GB005521

Simmons, A., Uppala, S., Dee, D., & Kobayashi, S. (2006). ERA-Interim: New ECMWF reanalysis products from 1989 onwards. *ECMWF Newsletter No. 110*, 25–35.

Stramma, L., Johnson, G. C., Firing, E., & Schmidtko, S. (2010, 9). Eastern Pacific oxygen minimum zones: Supply paths and multidecadal changes. *Journal of Geophysical Research*, *115*(C9), C09011. Retrieved from http://doi.wiley.com/10.1029/2009JC005976 doi: 10.1029/2009JC005976

Stramma, L., Johnson, G. C., Sprintall, J., & Mohrholz, V. (2008, 5). Expanding Oxygen-Minimum Zones in the Tropical Oceans. *Science*, *320*(5876), 655–658. Retrieved from https://www.science.org/doi/10.1126/science.1153847 doi: 10.1126/science.1153847

Suntharalingam, P., Sarmiento, J. L., & Toggweiler, J. R. (2000). Global significance of nitrous-oxide production and transport from oceanic low-oxygen zones: A modeling study. *Global Biogeochemical Cycles*, *14*(4), 1353–1370. doi: 10.1029/1999GB900100

Thamdrup, B., Dalsgaard, T., & Revsbech, N. P. (2012, 7). Widespread functional anoxia in the oxygen minimum zone of the Eastern South Pacific. *Deep Sea Research Part I: Oceanographic Research Papers*, *65*, 36–45. doi: 10.1016/J.DSR.2012.03.001

Tian, H., Xu, R., Canadell, J. G., Thompson, R. L., Winiwarter, W., Suntharalingam, P., ... Yao, Y. (2020). A comprehensive quantification of global nitrous oxide sources and sinks. *Nature*, *586*(October). Retrieved from http://dx.doi.org/10.1038/s41586-020-2780-0 doi: 10.1038/s41586-020-2780-0

Walter, S., Bange, H. W., Breitenbach, U., & Wallace, D. W. R. (2006). *Nitrous oxide in the north atlantic ocean* (Vol. 3; Tech. Rep. No. 4). Retrieved from https://bg.copernicus.org/articles/3/607/2006/ doi: 10.5194/bg-3-607-2006

Wanninkhof, R. (1992). Relationship between wind speed and gas exchange over the ocean. *Journal of Geophysical Research*, *97*(C5), 7373–7382. doi: 10.1029/92JC00188

Yang, S., Chang, B. X., Warner, M. J., Weber, T. S., Bourbonnais, A. M., Santoro, A. E., ... Bianchi, D. (2020). Global reconstruction reduces the uncertainty of oceanic nitrous oxide emissions and reveals a vigorous seasonal cycle. *Pro-*

ceedings of the National Academy of Sciences of the United States of America, *117*(22). doi: 10.1073/pnas.1921914117

Yang, S., Gruber, N., Long, M. C., & Vogt, M. (2017, 10). ENSO-Driven Variability of Denitrification and Suboxia in the Eastern Tropical Pacific Ocean. *Global Biogeochemical Cycles*, *31*(10), 1470–1487. doi: 10.1002/2016GB005596

Yoshida, N., Morimoto, H., Hirano, M., Koike, I., Matsuo, S., Wada, E., ... Hattori, A. (1989, 12). Nitrification rates and 15N abundances of N2O and NO3 in the western North Pacific. *Nature*, *342*(6252), 895–897. doi: 10.1038/342895a0

Supporting Information for "Pathways of Nitrous Oxide Production in the Eastern Tropical South Pacific Oxygen Minimum Zone"

Daniel McCoy[1], Pierre Damien[1], Daniel Clements[1], Simon Yang[1], Daniele Bianchi[1]

[1]Department of Atmospheric and Oceanic Sciences

[1]University of California – Los Angeles

[1]520 Portola Plaza, Los Angeles, CA 90095, USA

Contents of this file

1. Text S1 to S4
   - S1: Treatment of Organic Matter
   - S2: NitrOMZ Nitrogen Cycle
   - S3: NitrOMZ Tracer Sources-and-sinks
   - S4: Light Inhibition
2. Tables S1 to S5
3. Figures S1 to S14

Corresponding author: Daniel McCoy, Department of Atmospheric and Oceanic Sciences, University of California – Los Angeles, 520 Portola Plaza, Los Angeles, CA 90095, USA. (demccoy@atmos.ucla.edu)

S1: Treatment of Organic Matter In the model, remineralization of sinking particulate OM follows the formulation of Moore, Doney, and Lindsay (2004), where sinking is implicit and based on the ballast model from Armstrong, Lee, Hedges, Honjo, and Wakeham (2001). Particulate organic carbon (POC) in BEC is produced at each time-step following:

$$R^{poc}_{prod}(z) = (R^{sp}_{graze,poc}(z) + R^{diat}_{graze,poc}(z) + R^{diaz}_{graze,poc}(z)) + (R^{sp}_{agg}(z) + R^{diat}_{agg}(z) + R^{diaz}_{agg}(z)) + (R^{sp}_{loss,poc}(z) + R^{diat}_{loss,poc}(z) + R^{diaz}_{loss,poc}(z)) + f^{d}_{zoo}R^{l}_{zoo}(z).$$

See Table S1 for descriptions of each rate; further details can be found in Deutsch et al. (2021). POC production is then partitioned into a free and mineral component:

$$R^{poc}_{prod}(z) = R^{free,poc}_{prod}(z) + R^{min,poc}_{prod}(z). \tag{1}$$

Following equation (1), both free and mineral POC is instantaneously distributed in the water column following one-dimensional steady-state production-remineralization equations. The vertical profile of free POC flux (Φ_{poc}) is calculated as:

$$\Phi_{free,poc}(z) = \Phi_{free,poc}(z_o)e^{-\frac{1}{\lambda_{poc}}(z-z_o)} + \int_{z_o}^{z} R^{prod}_{free,poc}(z)e^{-\frac{1}{\lambda_{poc}}(z-z_o)}dz. \tag{2}$$

Here, λ_{poc} is a discretized exponential scale length computed from an initial scale length (γ_{poc}) that is modified by both the local O_2 concentration of layer z:

$$\gamma_{poc} = \begin{cases} \gamma_{poc} * 3.3 & \text{where } O_2 < 5 \text{ mmol/m}^3 \\ \gamma_{poc} * (1 + (3.3-1)(40-o_2)/35) & \text{where } 5 \text{ mmol/m}^3 < O_2 < 40 \text{ mmol/m}^3 \\ \gamma_{poc} & \text{elsewhere} \end{cases} \tag{3}$$

and its thickness dz:

$$\lambda_{poc} = \begin{cases} \gamma_{poc} * (1.0), & \text{where dz <100m} \\ \gamma_{poc} * (1.0 * (2.9 - 1.0) * (-dz - 1.0)/(2.9 - 1.0), & \text{where 100m<dz<250m} \\ \gamma_{poc} * (2.9 * (5.6 - 2.9) * (-dz - 2.9)/(5.6 - 2.9), & \text{where 250m<dz<500m} \\ \gamma_{poc} * (5.6 * (5.7 - 5.6) * (-dz - 5.6)/(5.7 - 5.6), & \text{where 500m<dz<700m} \\ \gamma_{poc} * (5.7). & \text{elsewhere} \end{cases} \quad (4)$$

See Table S2 for parameter values.

The vertical profile of POC flux for each mineral is calculated as the sum of a soft and hard component (where the hard component is a fraction of the total based on f_{pcaco3}, f_{psio_2}, and f_{dust}, respectively, see Table S2). The soft component for $CaCO_3$, SiO_2, and dust follow similar remineralization processes as in equation (2), whereas the hard components remineralize according to λ_{hard} and $\lambda_{hard,dust}$ (for dust). The fluxes of each mineral are then summed in C units:

$$\Phi_{min,poc}(z) = \rho_{pcaco3}(\Phi^{soft}_{pcaco3}(z) + \Phi^{hard}_{pcaco3}(z)) + \rho_{psio_2}(\Phi^{soft}_{psio_2}(z) + \Phi^{hard}_{psio_2}(z)) + \rho_{dust}(\Phi^{soft}_{dust}(z) + \Phi^{hard}_{dust}(z))$$

Remineralization at each vertical level is then calculated as the divergence of the POC flux:

$$R^{poc}_{rem}(z) = R^{poc}_{prod}(z) + \frac{d}{dz}(\Phi_{free,poc}(z) + \Phi_{min,poc}(z)) \quad (5)$$

In contrast, dissolved organic carbon (DOC) is an explicit ROMS-BEC tracer and is remineralized (R^{doc}_{rem}) based on a timescale of 15 years with a sharp decrease (6.85%) applied below the euphotic zone as in Frischknecht, Münnich, and Gruber (2017). Local OM remineralization in the water column (R^{tot}_{rem}) is calculated as the sum of POC and DOC remineralization:

$$R^{tot}_{rem}(z) = R^{poc}_{rem}(z) + R^{doc}_{rem}(z). \quad (6)$$

S2: NitrOMZ Nitrogen Cycle The NitrOMZ model expands BEC by including, along with aerobic remineralization (R_{rem}), additional heterotrophic denitrification steps under low-O_2 conditions (Bianchi et al., 2022): NO_3^- reduction (R_{den1}), NO_2^- reduction (R_{den2}), and N_2O reduction (R_{den3}). In order to preserve BEC OM cycle, R_{rem}^{tot} (equation (6)) is partitioned into four possible components at each vertical level and time-step:

$$R_{rem}^{tot}(z) = R_{rem}(z) + R_{den1}(z) + R_{den2}(z) + R_{den3}(z) = \sum_{n=1}^{4} R_i(z), \tag{7}$$

where i represents one of the four respiration pathways. In practice, we calculate the contribution to total remineralization by each pathway i as:

$$R_i(z) = f_i(z) \cdot R_{rem}^{tot}(z), \tag{8}$$

where f_i is the relative fraction of remineralization carried out by the process i. The individual depth-dependent fractions are calculated as:

$$f_i(z) = \frac{r_i(z)}{\sum_{i=1}^{4} r_i(z)}, \tag{9}$$

where r_i is the specific heterotrophic respiration rate of the reaction, calculated based on a maximum remineralization rate modulated by a Michaelis-Menten function of the oxidant utilized (O_2, NO_3^-, NO_2^-, and N_2O for R_{rem}, R_{den1}, R_{den2}, and R_{den3}, respectively) and an exponential inhibition by oxygen (ignored for aerobic respiration):

$$r_i(z) = k_i \cdot \frac{[\mathrm{X}](z)}{K_i^X + [\mathrm{X}](z)} \cdot e^{-\frac{\mathrm{O_2}(z)}{K_i^{o2}}}. \tag{10}$$

Here, k_i represents the maximum respiration rate for each reaction, K_i^X is the half saturation constant for oxidant $[X]$ uptake, and K_i^{o2} is the scale for inhibition by oxygen.

The chemolithotrophic rates of NH_4^+ oxidation (R_{ao}), NO_2^- oxidation (R_{no}), and anaerobic NH_4^+ oxidation (anammox, R_{ax}) are represented in NitrOMZ using Michaelis-Menten

functions for both the oxidants (O_2, O_2, and NO_2^- for K_{ao}, K_{no}, and K_{ax}, respectively) and reductants (NH_4^+, NO_2^-, and NH_4^+, respectively). The general form for R_{ao} and R_{no} is:

$$R_i(z) = k_i \cdot \frac{[\mathrm{X}](z)}{K_i^X + [\mathrm{X}](z)} \cdot \frac{[\mathrm{Y}](z)}{K_i^Y + [\mathrm{Y}](z)}. \tag{11}$$

Here, k_i represents the maximum respiration rate for each reaction, and K_i^X and K_i^Y are the half saturation constants for oxidant $[X]$ and reductant $[Y]$ uptake, respectively. Both R_{ao} and R_{no} are also inhibited by light, outlined in 1. The rate of anammox follows a similar calculation, but with an additional rate-specific exponential O_2 inhibition (K_{ax}^{o2}) term applied, similar to the heterotrophic denitrification steps in equation (10). See Table S4 for parameter values used in this study.

S3: NitrOMZ Tracer Sources-and-sinks NitrOMZ represents six major components of the marine nitrogen cycle: N_2, NO_3^-, NO_2^-, N_2O, NH_4^+, and organic nitrogen, which is linked to POC and DOC via fixed stoichiometry. The biogeochemical sources and sinks for each of the remaining tracers (in units of $mmol\ m^{-3}$) are:

$$\frac{d}{dt}(\mathrm{N_2}) = (Q_{den}^{C:N} \cdot R_{den3}) + R_{ax} + (0.5 \cdot R_{den}^{sed}) \tag{12}$$

$$\frac{d}{dt}(\mathrm{NO_3^-}) = R_{no} - (Q_{den}^{C:N} \cdot R_{den1}) - R_{den}^{sed} - R_{up,no_3}^{sp} - R_{up,no_3}^{diat} - R_{up,no_3}^{diaz} \tag{13}$$

$$\frac{d}{dt}(\mathrm{NO_2^-}) = R_{ao}^{no_2} - R_{no} + Q_{den}^{C:N}(R_{den1} - R_{den2}) - R_{ax} - R_{up,no_2}^{sp} - R_{up,no_2}^{diat} - R_{up,no_2}^{diaz} \tag{14}$$

$$\frac{d}{dt}(\mathrm{N_2O}) = 0.5(R_{ao}^{n_2o} + (Q_{den}^{C:N} \cdot R_{den2})) - (Q_{den}^{C:N} \cdot R_{den3}) \tag{15}$$

$$\begin{aligned}\frac{d}{dt}(\mathrm{NH_4^+}) = {} & DON(\tau^{DON}) + DONr(\tau^{DONr}) - R_{ao} - R_{ax} \\ & + Q_{rem}^{C:N}(R_{loss,dic}^{sp} + R_{loss,dic}^{diat} + R_{loss,dic}^{diaz}) \\ & + Q_{rem}^{C:N}(R_{graze,dic}^{sp} + R_{graze,dic}^{diat} + R_{graze,dic}^{diaz} + R_{loss,dic}^{zoo}) \\ & + Q_{rem}^{C:N}(R_{poc}^{rem}(1 - Q^{DONr})) - (R_{up,nh_4}^{sp} + R_{up,nh_4}^{diat} + R_{up,nh_4}^{diaz})\end{aligned} \tag{16, 17}$$

Here the symbol d/dt denotes the sum of the local time derivative and the physical transport, and $Q_{rem}^{C:N}$ and $Q_{den}^{C:N}$ represent the approximate carbon to nitrogen ratio from remineralization (16/117) and denitrification (472/2/106), respectively, following Anderson and Sarmiento (1994). The sedimentary denitrification rate (R_{den}^{sed}) follows the same formulation as in Deutsch et al. (2021).

Following the N_2O tracer and N_2O reduction rate decomposition described in Section 2.4, the equations for each of the N_2O tracers (in units of $mmol$ N_2O m^{-3}) are represented

as:

$$\frac{d}{dt}(\mathrm{N_2O}_{den}) = Q_{den}^{C:N}(0.5 \cdot R_{den2} - R_{den3}^{den}), \tag{18a}$$

$$\frac{d}{dt}(\mathrm{N_2O}_{nit}) = (0.5 \cdot R_{ao}^{n_2o}) - (Q_{den}^{C:N} \cdot R_{den3}^{nit}), \tag{18b}$$

$$\frac{d}{dt}(\mathrm{N_2O}_{bou}) = -Q_{den}^{C:N} \cdot R_{den3}^{bou},, \tag{18c}$$

$$\frac{d}{dt}(\mathrm{N_2O}_{atm}) = -Q_{den}^{C:N} \cdot R_{den3}^{atm}. \tag{18d}$$

$$\tag{18e}$$

Descriptions of each nitrogen cycle tracer are presented in Table S5.

S4: Light Inhibition In NitrOMZ, rates of both NH_4^+ and NO_2^- oxidation (R_{ao} and R_{no}, respectively) are photo-inhibited by photosynthetically available radiation (PAR) near the surface, modelled in ROMS-BEC using the same formulation as in Frischknecht et al. (2017). Surface PAR (PAR_{in}) is attenuated with depth via a discretized exponential scale length parameter (λ_{par}) computed from an initial surface value (λ_{par_i}):

$$\lambda_{par_i} = max(0.02, Chl_{tot}), \tag{19}$$

where Chl_{tot} is the sum of community chlorophyll from diatoms (Chl_{diat}), diazotrophs (Chl_{diaz}), and small phytoplankton (Chl_{sp}). The attenuation coefficient is then further modified depending on the initial value of λ_{par_i}:

$$\lambda_{par}(z) = \begin{cases} 0.0919 \cdot (\lambda_{par_i})^{0.3536} \cdot dz & \text{where } \lambda_{par_i} < 0.13224, \\ 0.1131 \cdot (\lambda_{par_i})^{0.4562} \cdot dz & \text{where } \lambda_{par_i} \geq 0.13224. \end{cases} \tag{20}$$

In the initial surface grid cell, attenuation of PAR_{in} from the top of the cell over the cell thickness (m) is calculated as:

$$\mathrm{PAR}_{out}(z) = \mathrm{PAR}_{in}(z) \cdot e^{-\lambda_{par}(z)}. \tag{21}$$

For each cell, if both $\mathrm{PAR}_{in}(z)$ and $\mathrm{PAR}_{out}(z)$ are less than the PAR limitation for either rate (PAR_{lim}^{ao} and PAR_{lim}^{no}, here both set to 1 W m^{-2}), then photo-inhibition is avoided and the rates are calculated via equation (11). If only $\mathrm{PAR}_{in}(z)$ exceeds PAR limitation, each rate is attenuated via:

$$R_{ao}(z) = R_{ao}(z) \cdot log(\frac{\mathrm{PAR}_{out}(z)/\mathrm{PAR}_{lim}^{ao}}{-\lambda_{par}(z)}) \tag{22}$$

$$R_{no}(z) = R_{no}(z) \cdot log(\frac{\mathrm{PAR}_{out}(z)/\mathrm{PAR}_{lim}^{no}}{-\lambda_{par}(z)}). \tag{23}$$

Following the calculation, $\mathrm{PAR}_{out}(z)$ is set to $\mathrm{PAR}_{in}(z)$ for the cell below and iterated over the number of depths.

Table S1. Organic matter cycle rates.

Rates	Description	Units
$R^{sp}_{graze,poc}$	Grazing loss for small phytoplankton routed to POC	mmol C/m^3/s
$R^{diat}_{graze,poc}$	Grazing loss for diatoms routed to POC	mmol C/m^3/s
$R^{diaz}_{graze,poc}$	Grazing loss for diazotrophs routed to POC	mmol C/m^3/s
R^{sp}_{agg}	Aggregation loss of small phytoplankton	mmol C/m^3/s
R^{diat}_{agg}	Aggregation loss of diatoms	mmol C/m^3/s
R^{diaz}_{agg}	Aggregation loss of diazotrophs	mmol C/m^3/s
$R^{sp}_{loss,poc}$	Non-grazing mortality of small phytoplankton routed to POC	mmol C/m^3/s
$R^{diat}_{loss,poc}$	Non-grazing mortality of diatoms routed to POC	mmol C/m^3/s
$R^{diaz}_{loss,poc}$	Non-grazing mortality of diazotrophs routed to POC	mmol C/m^3/s
R^{prod}_{poc}	Amount of particulate organic C produced	mmol C/m^3/s
$R^{prod}_{free,poc}$	Amount of non-mineral particulate organic C produced	mmol C/m^3/s
$R^{prod}_{min,poc}$	Amount of mineral particulate organic C produced	mmol C/m^3/s
R^{rem}_{poc}	Amount of particulate organic C remineralized	mmol C/m^3/s
Φ_{poc}	Incoming particulate C-flux	mmol C/m^3/s
$\Phi_{free,poc}$	Incoming non-mineral particulate C-flux	mmol C/m^3/s
$\Phi_{min,poc}$	Incoming mineral particulate C-flux	mmol C/m^3/s
Φ^{soft}_{pcaco3}	Incoming soft $CaCO_3$ particulate flux	mmol $CaCO_3$/m^3/s
$\Phi^{soft}_{psio_2}$	Incoming soft SiO_2 particulate flux	mmol SiO_2/m^3/s
Φ^{soft}_{dust}	Incoming soft dust flux	mmol C/m^3/s
Φ^{hard}_{pcaco3}	Incoming hard $CaCO_3$ particulate flux	mmol $CaCO_3$/m^3/s
$\Phi^{hard}_{psio_2}$	Incoming hard SiO_2 particulate flux	mmol SiO_2/m^3/s
Φ^{hard}_{dust}	Incoming hard dust flux	mmol C/m^3/s

Table S2. Organic matter cycle parameters

Parameters	Description	Value	Units
ρ_{pcaco3}	Associated molar ratio of $CaCO_3$ to POC	0.417	mol $CaCO_3$ / mol POC
ρ_{psio_2}	Associated molar ratio of SiO_2 to POC	0.250	mol SiO_2 / mol POC
ρ_{dust}	Associated molar ratio of dust to POC	4163.197	mol dust / mol POC
γ_{poc}	Initial length scale for remineralization of POC	88	m
γ_{pcaco3}	Length scale for remineralization of $CaCO_3$	150	m
γ_{psio_2}	Length scale for remineralization of SiO_2	250	m
γ_{dust}	Length scale for remineralization of dust	200	m
λ_{hard}	Length scale for remineralization of hard subclass	40	km
$\lambda_{hard,dust}$	Length scale for remineralization of hard dust subclass	125	km
f_{poc}	Fraction of POC routed to hard subclass	0	N/A
f_{pcaco3}	Fraction of $CaCO_3$ routed to hard subclass	0.3	N/A
f_{psio_2}	Fraction of SiO_2 routed to hard subclass	0.03	N/A
f_{dust}	Fraction of dust routed to hard subclass	0.97	N/A

Table S3. Nitrogen cycle rates

Name	Description	Units
R_{rem}	Remineralized particulate organic C	mmol C/m^3/s
$R_{ao}^{no_2}$	Rate of NH_4^+ oxidation to NO_2^-	mmol N/m^3/s
$R_{ao}^{n_2o}$	Rate of NH_4^+ oxidation to N_2O	mmol N/m^3/s
R_{no}	Rate of NO_2^- oxidation to NO_3^-	mmol N/m^3/s
R_{den1}	Rate of NO_3^- reduction to NO_2^-	mmol C/m^3/s
R_{den2}	Rate of NO_2^- reduction to N_2O	mmol C/m^3/s
R_{den3}	Rate of N_2O reduction to N_2	mmol C/m^3/s
R_{ax}	Rate of NH_4^+ and NO_2^- loss to N_2 via anammox	mmol N/m^3/s
R_{den}^{sed}	Rate of sedimentary denitrification	mmol N/m^3/s
$R_{loss,dic}^{sp}$	Non-grazing mortality of small phytoplankton routed to DIC	mmol C/m^3/s
$R_{loss,dic}^{diat}$	Non-grazing mortality of diatoms routed to DIC	mmol C/m^3/s
$R_{loss,dic}^{diaz}$	Non-grazing mortality of diazotrophs routed to DIC	mmol C/m^3/s
$R_{loss,dic}^{zoo}$	Zooplankton mortality routed to DIC	mmol C/m^3/s
$R_{graze,dic}^{sp}$	Grazed mortality of small phytoplankton routed to DIC	mmol C/m^3/s
$R_{graze,dic}^{diat}$	Grazed mortality of diatoms routed to DIC	mmol C/m^3/s
$R_{graze,dic}^{diaz}$	Grazed mortality of diazotrophs routed to DIC	mmol C/m^3/s
R_{up,nh_4}^{sp}	Uptake of NH_4^+ by small phytoplankton	mmol N/m^3/s
R_{up,nh_4}^{diat}	Uptake of NH_4^+ by diatoms	mmol N/m^3/s
R_{up,nh_4}^{diaz}	Uptake of NH_4^+ by diazotrophs	mmol N/m^3/s
R_{up,no_3}^{sp}	Uptake of NO_3^- by small phytoplankton	mmol N/m^3/s
R_{up,no_3}^{diat}	Uptake of NO_3^- by diatoms	mmol N/m^3/s
R_{up,no_3}^{diaz}	Uptake of NO_3^- by diazotrophs	mmol N/m^3/s
R_{up,no_2}^{sp}	Uptake of NO_2^- by small phytoplankton	mmol N/m^3/s
R_{up,no_2}^{diat}	Uptake of NO_2^- by diatoms	mmol N/m^3/s
R_{up,no_2}^{diaz}	Uptake of NO_2^- by diazotrophs	mmol N/m^3/s

Table S4. Nitrogen cycle parameters

Parameters	Description	Value	Units
k_{rem}	Maximum respiration rate	9.259E-7	mmol C/m^3/s
k_{ao}	Maximum NH_4^+ oxidation rate	5.787E-7	mmol N/m^3/s
k_{no}	Maximum NO_2^- oxidation rate	5.787E-7	mmol N/m^3/s
k_{den1}	Maximum NO_3^- reduction rate	1.852E-7	mmol C/m^3/s
k_{den2}	Maximum NO_2^- reduction rate	9.259E-8	mmol C/m^3/s
k_{den3}	Maximum N_2O reduction rate	5.741E-7	mmol C/m^3/s
k_{ax}	Maximum anaerobic NH_4^+ oxidation rate	5.105E-6	mmol N/m^3/s
$K_{rem}^{o_2}$	Respiration half-saturation constant for O_2 uptake	1.000	mmol O_2/m^3
$K_{ao}^{o_2}$	NH_4^+ oxidation half-saturation constant for O_2 uptake	0.333	mmol N/m^3
$K_{ao}^{nh_4}$	NH_4^+ oxidation half-saturation constant for NH_4^+ uptake	0.305	mmol N/m^3
$K_{no}^{o_2}$	NO_2^- oxidation half-saturation constant for O_2 uptake	0.778	mmol N/m^3
$K_{no}^{no_2}$	NO_2^- oxidation half-saturation constant for NO_2^- uptake	0.509	mmol N/m^3
$K_{den1}^{no_3}$	NO_3^- reduction half-saturation constant for NO_3^- uptake	1.000	mmol N/m^3
$K_{den2}^{no_2}$	NO_2^- reduction half-saturation constant for NO_2^- uptake	0.010	mmol N/m^3
$K_{den3}^{n_2o}$	N_2O reduction half-saturation constant for N_2O uptake	0.159	mmol N/m^3
$K_{ax}^{nh_4}$	NH_4^+ oxidation half-saturation constant for NH_4^+ uptake	0.230	mmol N/m^3
$K_{ax}^{no_2}$	NH_4^+ oxidation half-saturation constant for NO_2^- uptake	0.100	mmol N/m^3
a	O_2-dependent coefficient (Nevison et al., 2003)	0.300	N/A
b	Background coefficient (Nevison et al., 2003)	0.100	N/A
$K_{den1}^{o_2}$	O_2 poisoning constant for NO_3^- reduction	6.000	mmol O_2/m^3
$K_{den2}^{o_2}$	O_2 poisoning constant for NO_2^- reduction	2.300	mmol O_2/m^3
$K_{den3}^{o_2}$	O_2 poisoning constant for N_2O reduction	0.506	mmol O_2/m^3
$K_{ax}^{o_2}$	O_2 poisoning constant for anammox	6.000	mmol O_2/m^3
τ^{DON}	Semi-labile DON remineralization inverse timescale	1.826E-4	1/s
τ^{DONr}	Refractory DON remineralization inverse timescale	2.884E-7	1/s
Q^{DONr}	Fraction of DON to refractory pool	0.0115	N/A
PAR_{lim}^{ao}	PAR limitation for NH_4^+ oxidation	1.000	W/m^2
PAR_{lim}^{no}	PAR limitation for NO_2^- oxidation	1.000	W/m^2

Table S5. Nitrogen cycle tracers

Name	**Description**	**Units**
DON	Dissolved organic nitrogen	mmol N/m^3
DONr	Refractory dissolved organic nitrogen	mmol N/m^3
NH_4^+	Ammonium	mmol N/m^3
NO_2^-	Nitrite	mmol N/m^3
NO_3^-	Nitrate	mmol N/m^3
N_2O	Nitrous oxide	mmol N/m^3
N_2O_{den}	Nitrous oxide sourced from denitrification	mmol N/m^3
N_2O_{nit}	Nitrous oxide sourced from nitrification	mmol N/m^3
N_2O_{atm}	Saturated nitrous oxide sourced from boundaries and ingassing	mmol N/m^3
N_2O_{bou}	Supersaturated nitrous oxide sourced from boundaries	mmol N/m^3
N_2	Dinitrogen	mmol N/m^3

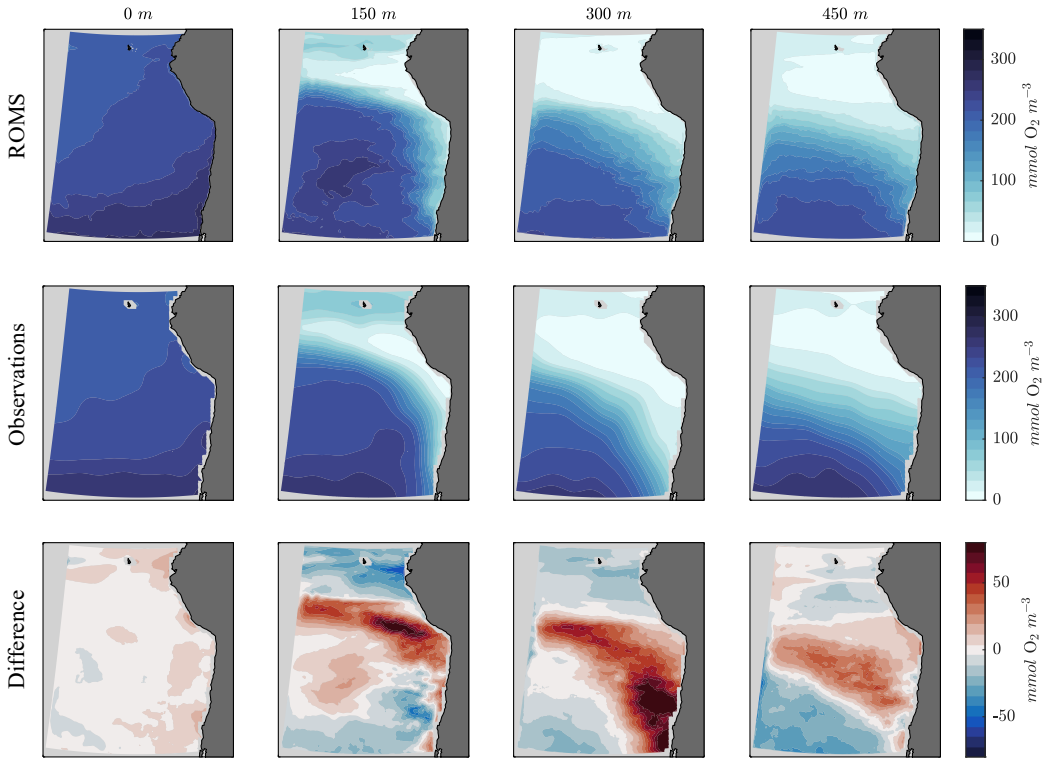

Figure S1. 0, 150, 300, and 450 m annually averaged O_2 from (top) ROMS model years 46 - 50, (middle) World Ocean Atlas 2018 O_2 (Garcia et al., 2019), and (bottom) their differences (ROMS - WOA18).

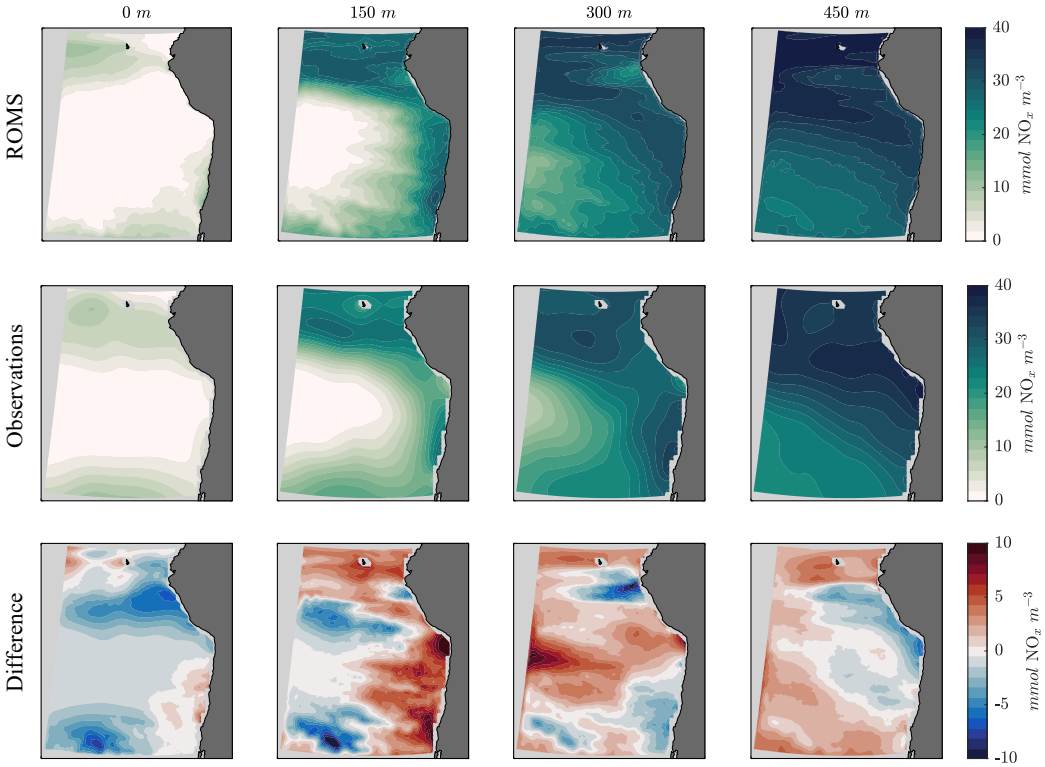

Figure S2. Same as in Figure S1, but for nitrate + nitrite (NO_x).

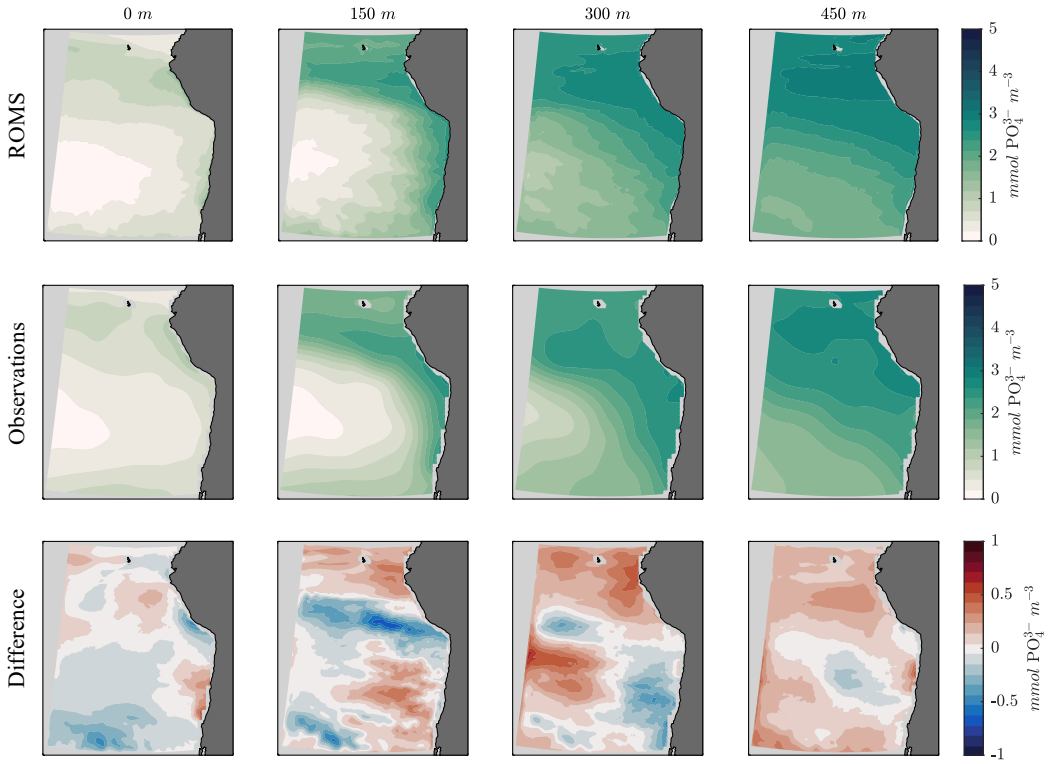

Figure S3. Same as in Figure S1, but for phosphate (PO_4^{3-}).

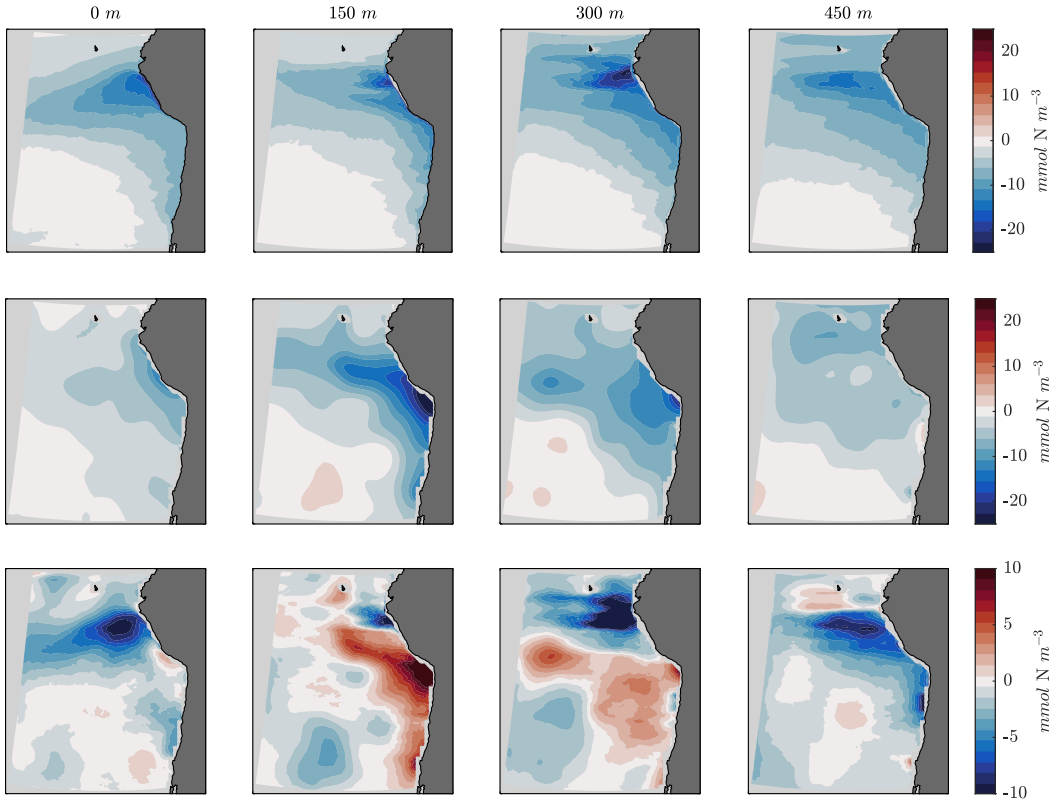

Figure S4. Same as in Figure S1, but for N* (here defined as 16·[NO_3^-] - [PO_4^{3-}]).

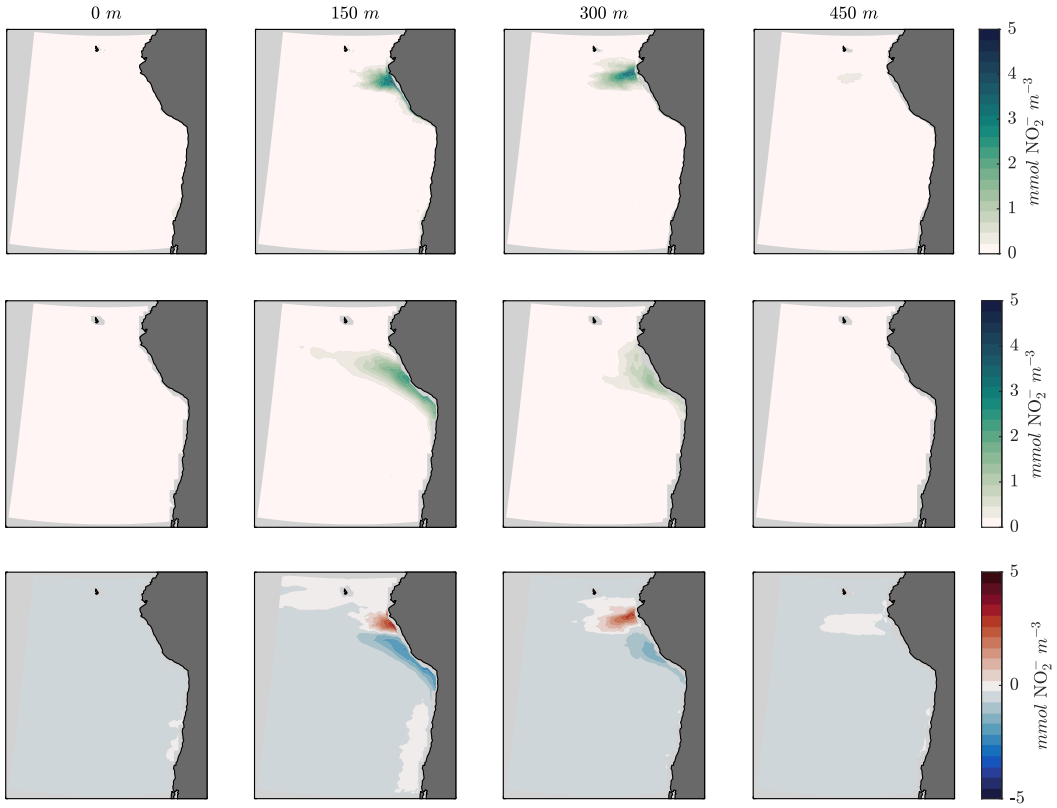

Figure S5. Same as in Figure S1, but for NO_2^- comparisons against machine learning estimates.

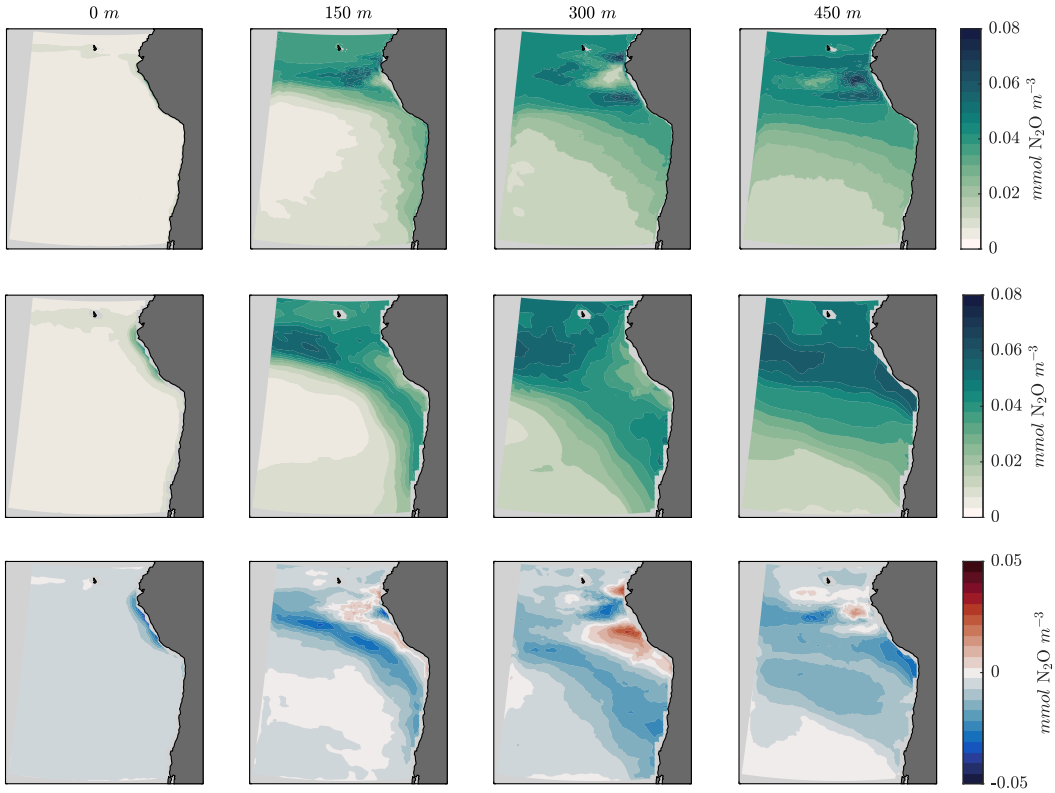

Figure S6. Same as in Figure S1, but for N_2O comparisons against machine learning estimates.

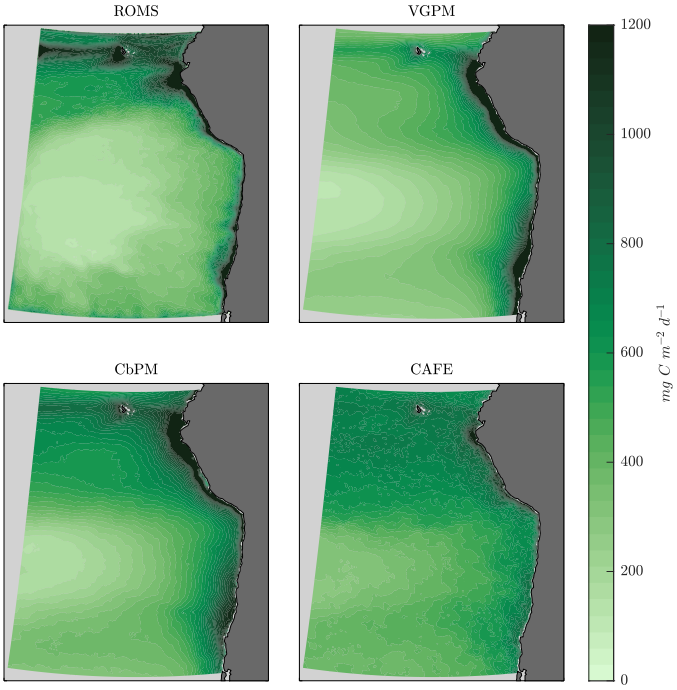

Figure S7. Annually averaged net Primary Production (NPP) from (top left) ROMS model years 46 - 50, (top right) the Eppley Vertically Generalized Production Model (Eppley-VGPM, Behrenfeld and Falkowski (1997))), (bottom left) the updated Carbon-Based Productivity Model (CbPM, Behrenfeld et al. (2005)), and (bottom right) the Fluorescence Euphotic-resolving model (CAFE, Silsbe et al. (2016)).

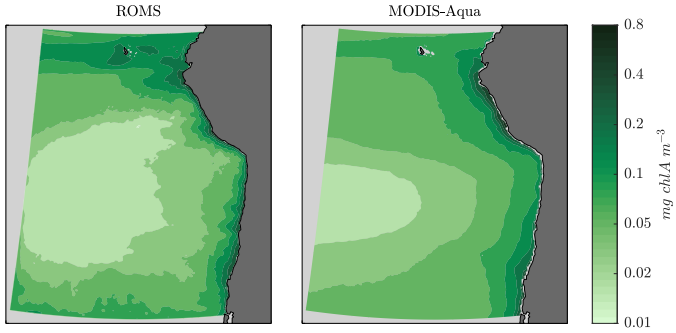

Figure S8. Annually averaged surface chlorophyll-A (chlA) from (left) ROMS model years 46 - 50 and (right) MODIS-Aqua.

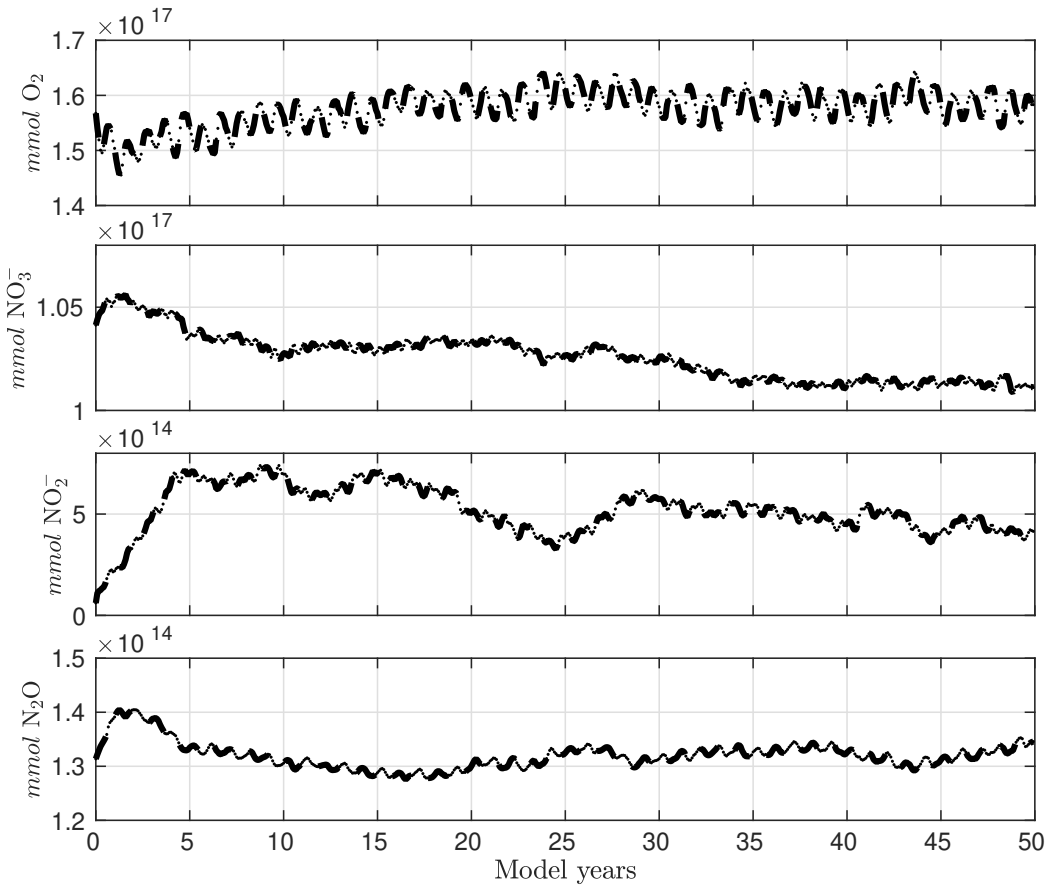

Figure S9. Integrated O_2, NO_3^-, NO_2^-, and N_2O tracers within the OMZ budget domain for model years 0 - 50.

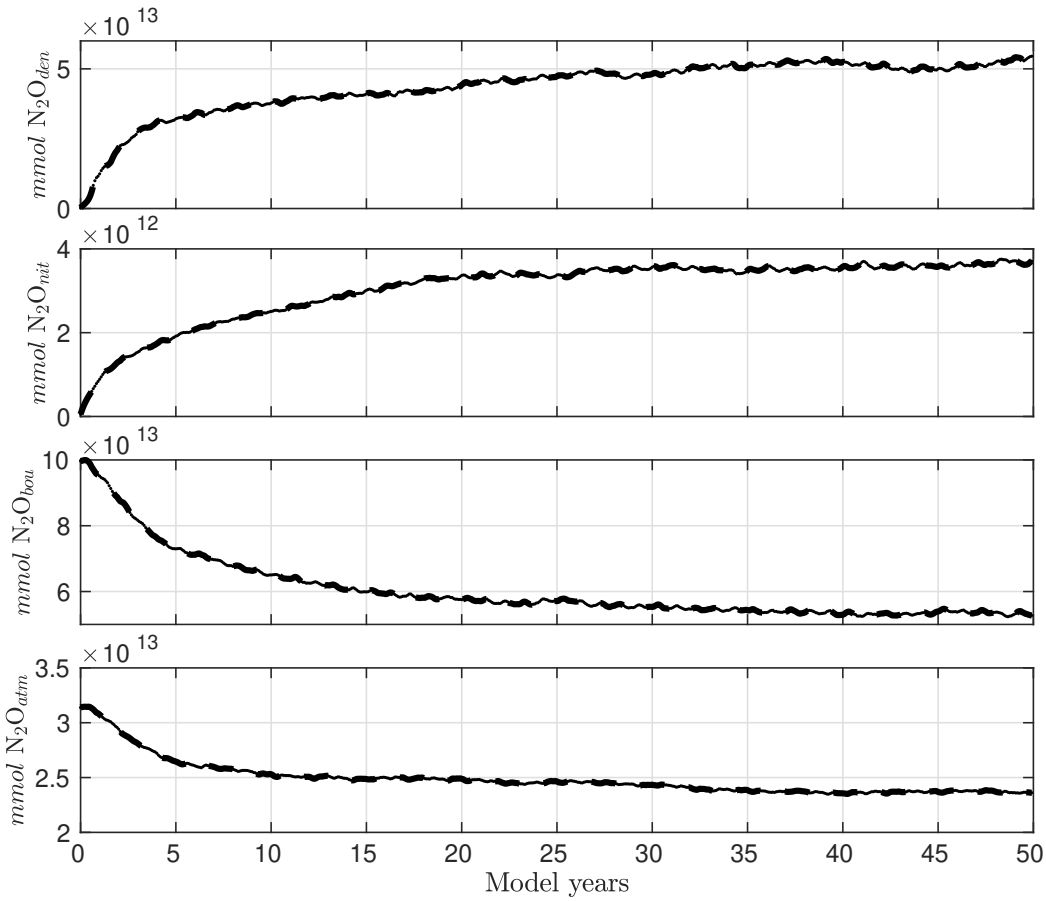

Figure S10. Integrated N_2O_{nit}, N_2O_{den}, N_2O_{bou}, and N_2O_{atm} tracers within the OMZ budget domain for model years 0 - 50.

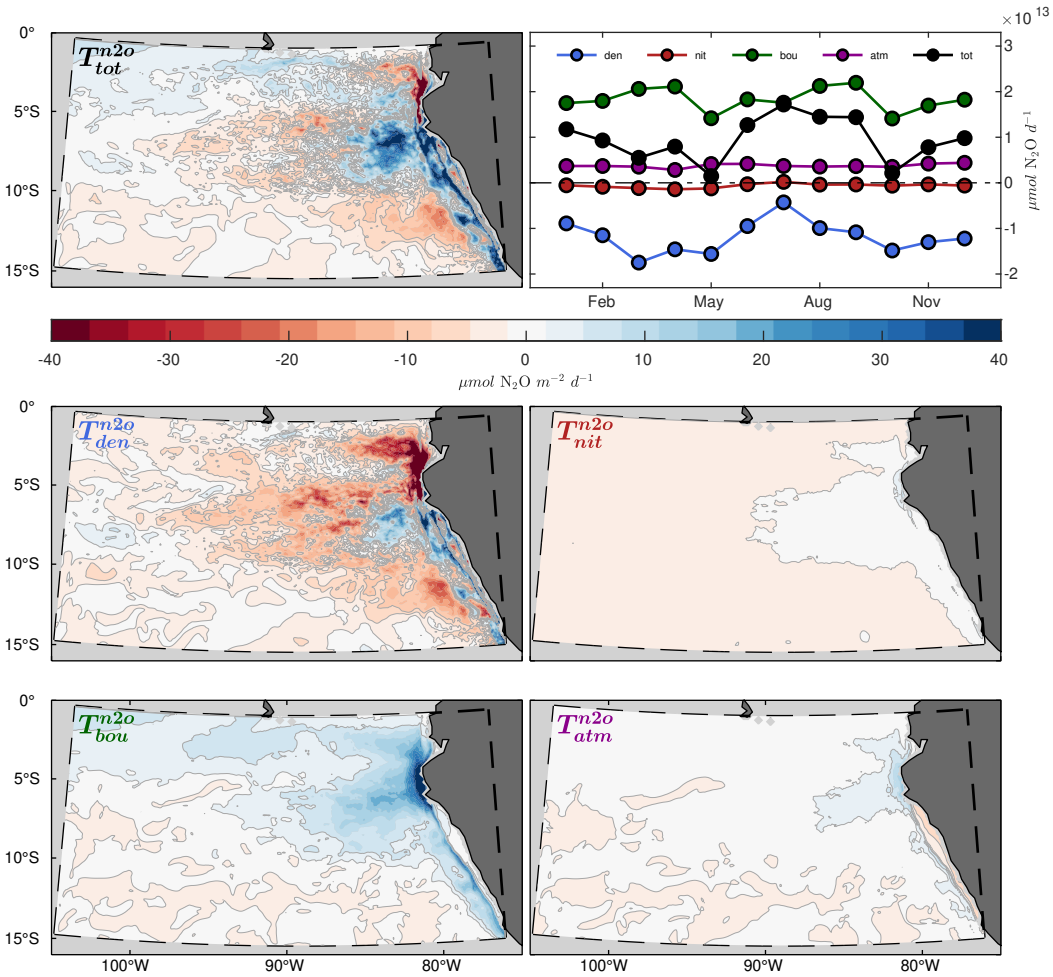

Figure S11. (top left) Vertically integrated divergence of advective and diffusive fluxes (T) for N_2O from the OMZ budget domain, annually averaged from model years 46 - 50. (top right) Time-series of integrated divergence of advective and diffusive fluxes for N_2O (black) and the decomposed N_2O tracers. (bottom panels) Same as in the top left panel, but for each of the decomposed N_2O tracers. Positive values are shown in blue, and negative values in red.

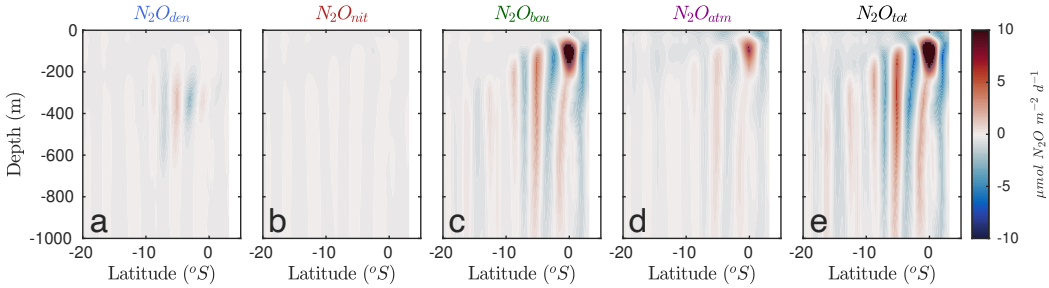

Figure S12. Annually averaged zonal N_2O transport from the western boundary of the OMZ budget domain (roughly 105^oW) from model years 46 - 50 for (a) N_2O_{den}, (b) N_2O_{nit}, (c) N_2O_{bou}, (d) N_2O_{atm}, and (e) N_2O.

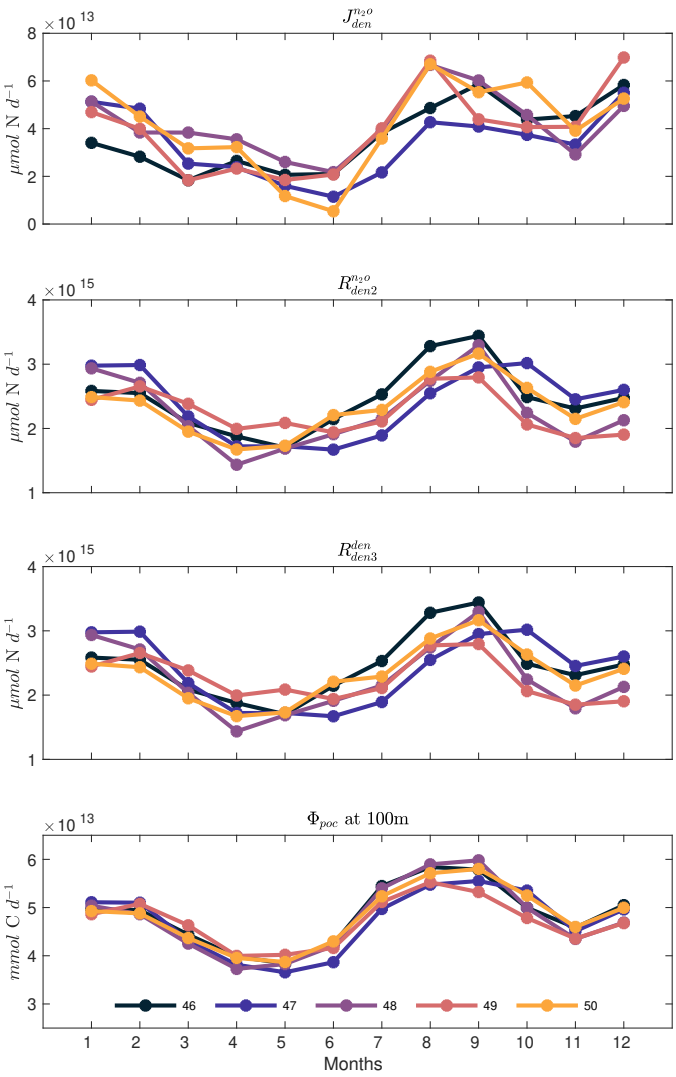

Figure S13. Integrated net N_2O production rate from denitrification ($J^{n_2o}_{den}$), integrated NO_2^- reduction rate ($R^{n_2o}_{den2}$), integrated N_2O reduction rate of denitrification-sourced N_2O (R^{den3}_{den}), and vertical POC flux (Φ_{poc}) at 100m from the OMZ budget domain for ROMS model years 46 - 50.

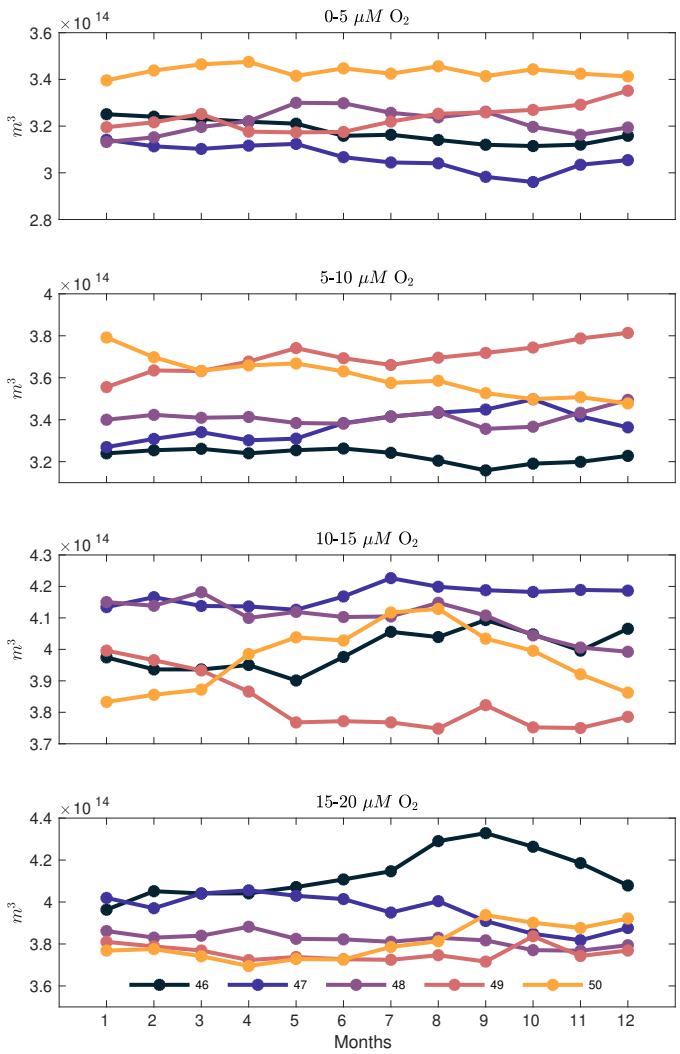

Figure S14. Volume of the OMZ budget domain occupied by various O_2 thresholds (0 - 5, 5 - 10, 10 - 15, and 15 - 20 $mmol$ O_2 m^{-3}) for ROMS model years 46 - 50.

References

Anderson, L. A., & Sarmiento, J. L. (1994, 3). Redfield ratios of remineralization determined by nutrient data analysis. *Global Biogeochemical Cycles*, *8*(1), 65–80. Retrieved from `http://doi.wiley.com/10.1029/93GB03318` doi: 10.1029/93GB03318

Armstrong, R. A., Lee, C., Hedges, J. I., Honjo, S., & Wakeham, S. G. (2001, 1). A new, mechanistic model for organic carbon fluxes in the ocean based on the quantitative association of POC with ballast minerals. *Deep Sea Research Part II: Topical Studies in Oceanography*, *49*(1-3), 219–236. Retrieved from `https://linkinghub.elsevier.com/retrieve/pii/S0967064501001011` doi: 10.1016/S0967-0645(01)00101-1

Behrenfeld, M. J., Boss, E., Siegel, D. A., & Shea, D. M. (2005, 3). Carbon-based ocean productivity and phytoplankton physiology from space. *Global Biogeochemical Cycles*, *19*(1). Retrieved from `http://doi.wiley.com/10.1029/2004GB002299` doi: 10.1029/2004GB002299

Behrenfeld, M. J., & Falkowski, P. G. (1997, 1). Photosynthetic rates derived from satellite-based chlorophyll concentration. *Limnology and Oceanography*, *42*(1), 1–20. Retrieved from `http://doi.wiley.com/10.4319/lo.1997.42.1.0001` doi: 10.4319/lo.1997.42.1.0001

Bianchi, D., McCoy, D., & Yang, S. (2022). Formulation, optimization and sensitivity of nitromzv1.0, a biogeochemical model of the nitrogen cycle in oceanic oxygen minimum zones. *Geoscientific Model Development Discussions*. doi: 10.5194/gmd-2022-244

Deutsch, C., Frenzel, H., McWilliams, J. C., Renault, L., Kessouri, F., Howard, E., ... Yang, S. (2021). Biogeochemical variability in the california current system. *Progress in Oceanography*, *196*, 102565. Retrieved from `https://www.sciencedirect.com/science/article/pii/S0079661121000525` doi: https://doi.org/10.1016/j.pocean.2021.102565

Frischknecht, M., Münnich, M., & Gruber, N. (2017, 1). Local atmospheric forcing driving an unexpected California Current System response during the 2015–2016 El Niño. *Geophysical Research Letters*, *44*(1), 304–311. doi: 10.1002/2016GL071316

Garcia, H., Weathers, K., Paver, C., Smolyar, I., Boyer, T., Locarnini, M., ... Reagan, J. (2019). World Ocean Atlas 2018, Volume 3: Dissolved Oxygen, Apparent Oxygen Utilization, and Dissolved Oxygen Saturation. *NOAA Atlas NESDIS*, *83*.

Moore, J. K., Doney, S. C., & Lindsay, K. (2004, 12). Upper ocean ecosystem dynamics and iron cycling in a global three-dimensional model. *Global Biogeochemical Cycles*, *18*(4), n/a-n/a. Retrieved from `http://doi.wiley.com/10.1029/2004GB002220` doi: 10.1029/2004GB002220

Silsbe, G. M., Behrenfeld, M. J., Halsey, K. H., Milligan, A. J., & Westberry, T. K. (2016, 12). The CAFE model: A net production model for global ocean phytoplankton. *Global Biogeochemical Cycles*, *30*(12), 1756–1777. Retrieved from `http://doi.wiley.com/10.1002/2016GB005521` doi: 10.1002/2016GB005521